INSTITUTE OF LOW TEMPERATURE AND STRUCTURE RESEARCH

POLISH ACADEMY OF SCIENCES

Division of Biomedical Physico-Chemistry

mgr inż. Zuzanna Korczak

Evaluation of luminescent properties of photon avalanching nano-, micro- and bulk crystals: novel materials, characterization methods and applications

Doctoral dissertation written under the guidance of
a supervisor **prof. dr hab. inż. Artur Bednarkiewicz**
and an auxiliary supervisor **dr inż. Marcin Szalkowski**

Wrocław, December 2023

Acknowledgements:

I would like to thank my supervisor, prof. dr hab. inż. Artur Bednarkiewicz, for his help, inspiration, scientific ideas for new experiments, knowledge and valuable guidance.

I extend my appreciation to the auxiliary supervisor dr inż. Marcin Szalkowski for his cooperation, constant support, interesting discussions.

My sincere thanks also go to the entire research group LuNASI with whom I had the honor of working, for the pleasant atmosphere of work and non-academic activities too.

May my thanks also go to my beloved parents, sister and family, who have always supported me, for love and sacrifices.

Finally, I would like to sincerely thank my friends who have been by my side throughout this journey. Your friendship made even the most difficult moments easier.

Table of contents

1. List of abbreviations

AuNR – gold nanorods

BS - beam splitter

CR - cross relaxation

DM - dichroic mirror

EMPA - energy migration photon avalanche

ES - excited state

ESA - excited state absorption

ETU- energy transfer upconversion

FM - flip mirror

FWHM - full width at half maximum

GS - grand state

GSA - grand state absorption

IR - infrared

IRQC - infrared quantum counter

LCD - liquid crystal display

LEDs - light-emitting diodes

MIRQC - medium infrared quantum counter detectors

MPA - migrating photon avalanche

MPR - multiphonon relaxation

MRI - magnetic resonance imaging

NC - nanocrystal

NDFs - neutral density filters

NIR – near-infrared

NPs- nanoparticles

OLED - organic light-emitting diodes

PA - photon avalanche

PALM - photoactivated localization microscopy

PASSI - photon-avalanche single-beam superresolution imaging

PLED - polymer light-emitting diodes

PM - power meter

PPF - paired-pulse facilitation

PSF - point spread function

RE - rare earth

REE - rare earth elements

SBR - single-band radiometric

SHG – second harmonic generation

SIM - structured illumination microscopy

SPA - sensitized photon avalanche

STED - stimulated emission depletion

STORM - stochastic optical reconstruction microscopy

TEM - transmission electron microscopy

THG - third harmonic generation

TPA - two photon absorption

UC - upconversion

UV - ultraviolet

VIS - visible

XRD - X-ray powder diffraction

ZBLAN - ZrF_4-BaF_2-LaF_3-AlF_3-NaF

2. Abstract

Photon avalanche (PA) is a fascinating phenomenon in the realm of photophysics. PA process was first observed in 1979 by Jay S. Chivian in a bulk $LaCl_3:Pr^{3+}$ crystal, while looking for materials suitable for medium infrared (IR) photon counting [1] until recently, this phenomenon was observed mostly at low temperatures in bulk crystals or optical fibers. However, in 2021 all the characteristic features of PA emission were demonstrated for the first time in nano-sized 8% Tm^{3+} doped β-$NaYF_4$ crystals. PA phenomenon is one type of upconversion (UC). PA is a cascade process that occurs in lanthanide ion doped crystals when photons of lower energy trigger a series of subsequent energy transfer processes (such as excited state absorption and cross-relaxation) and ultimately lead to photon emissions of higher energy characterized by highly non-linear multicolor luminescence intensity growth upon small increase of photoexcitation intensity which occurs above a certain pump power threshold. This power law relationship can reach non-linearities much above 10. The second characteristic feature of PA is the significant prolongation of the pump power dependent luminescence rise time (even up to hundreds of ms) for the excitation powers close to the threshold. Therefore, the major motivation behind current dissertation was to design and optimize tools to study PA phenomenon, as well as to evaluate new nano and micromaterials against the possibility to observe PA emission. Because no commercial instrumentation to study PA properties exist on the market, as part of the doctoral thesis I was involved in designing, building and optimizing an unique measuring system that was capable to count photons flux in wide 1 to 10^9 counts per second range over a large range of photoexcitation power density (10^2-10^7 Wcm^{-2}). The system is based on an optical microscope and detection is done in various alternative ways: spectrophotometer enables recording pump power dependent emission spectra, while luminescence intensity and luminescence kinetics can be recorded utilizing set of three PMT's connected to a dedicated photon counter.

Using this custom made microscopic system, I investigated spectroscopic and avalanche properties of nano- and microcrystals doped with various concentrations and combinations of lanthanide ions such as Tm^{3+}, Nd^{3+}, Pr^{3+}, Yb^{3+}, Ho^{3+}. Among the others, I measured the dependence of the luminescence intensity on the pump power density, as well as the PA rise and decay times for the Tm^{3+} avalanching ions. This dissertation delves into the fundamental principles behind PA in nano and microcrystals, exploring the role of size, composition, matrices and crystal structure in governing this process. I was

discussing the mechanisms by which PA can be initiated and controlled within these crystals. Additionally, I investigated the impact of crystal size, dopant concentration in microcrystals, evaluated the impact of various matrices and shell thickness in nanocrystals on PA emissions in Tm^{3+} ions. Moreover, I confirmed the occurrence of PA in Tm^{3+} doped $LiYF_4$ nanocrystals for the first time. Additionally, I explored how the presence of gold nanorods on the surface of crystals affected PA emission. Additionally, I also studied the behavior of PA in Yb^{3+} sensitized Pr^{3+}-doped nanocrystals under 852 nm and the influence of temperature on the visible PA emission. Furthermore, temperature measurements were conducted in crystals doped with Nd^{3+} ions under 1059 nm, but although anti-Stokes emission was observed and temperature dependent, no PA features were discovered.

PA is of particular interest in nanocrystals and microcrystals due to their unique size-dependent properties. These tiny crystalline structures, ranging from several nanometers to a dozen micrometers in diameter/length, exhibit remarkable optical properties that make them ideal candidates for harnessing the PA effect in the view of many potential applications in nano-bio-technology. PA can be used, among the other for (bio)sensing, (bio)imaging, optoelectronics, optical signal processing or optical computing. Materials demonstrating PA can also improve optical resolution in fluorescent microscopes and serve as luminescent nanothermometers with high relative temperature sensitivity. Some of these applications were also within the scope of my interest in the dissertation.

In summary, the scope of my interests in the dissertation covered wide range of activities in optical system design, versatile photophysical characterizations of various novel nano and micromaterials potentially capable to demonstrate photon avalanching phenomenon as well as evaluating their potential for luminescence thermometry and imaging applications.

3. Streszczenie w języku polskim

Po raz pierwszy lawinową emisję fotonów (PA) zaobserwowano w 1979 roku przez Jaya S. Chiviana w krysztale $LaCl_3:Pr^{3+}$, podczas poszukiwania materiałów odpowiednich do zliczania fotonów z zakresu średniej podczerwieni [1]. Do niedawna zjawisko to obserwowano głównie w niskich temperaturach w kryształach objętościowych lub światłowodach. Dopiero w 2021 roku wszystkie charakterystyczne cechy emisji PA zostały po raz pierwszy zademonstrowane w nanorozmiarowych kryształach $NaYF_4$ domieszkowanych 8% Tm^{3+}. PA zachodzi w kryształach domieszkowanych jonami lantanowców i prowadzi do anty-Stokesowskiej emisji tzn. pozwala uzyskać fotony o energii większej niż energia fotonów wzbudzających. Ponadto, emisja PA charakteryzuje się wysoce nieliniowym wzrostem intensywności wielokolorowej luminescencji przy niewielkim wzroście intensywności fotowzbudzenia, który występuje powyżej pewnego progu gęstości mocy lasera wzbudzającego. Zależność ta może osiągać nieliniowości znacznie powyżej 10. Kolejną charakterystyczną cechą PA jest wydłużenie (nawet do setek ms) czasu narastania luminescencji w zależności od intensywności pobudzenia dla mocy wzbudzenia bliskich wartości progowej.

Dlatego główną motywacją stojącą za badaniami zrealizowanymi w ramach obecnej rozprawy doktorskiej było zaprojektowanie i optymalizacja narzędzi do badania zjawiska PA, a także ocena nowych nano- i mikromateriałów pod kątem możliwości obserwacji emisji PA. Ponieważ na rynku nie istnieje komercyjne oprzyrządowanie do badania właściwości PA, w ramach pracy doktorskiej byłam zaangażowana w projektowanie, budowę i optymalizację unikalnego systemu pomiarowego, który był w stanie zliczać strumień fotonów w szerokim zakresie od 1 do 10^9 zliczeń na sekundę i w szerokim zakresie gęstości mocy fotowzbudzenia (10^2-10^7 Wcm^{-2}). Układ pomiarowy oparty jest na mikroskopie optycznym, a detekcja odbywa się na różne alternatywne sposoby: spektrofotometr umożliwia rejestrację widm emisji zależnych od mocy pompy, podczas gdy intensywność luminescencji i kinetyka luminescencji mogą być rejestrowane przy użyciu zestawu trzech PMT podłączonych do wielokanałowego licznika fotonów.

Korzystając z tego niestandardowego systemu mikroskopowego, badałam właściwości spektroskopowe i lawinowe nano- i mikrokryształów domieszkowanych różnymi stężeniami i kombinacjami jonów lantanowców, takich jak Tm^{3+}, Nd^{3+}, Pr^{3+}, Yb^{3+}, Ho^{3+}. Między innymi zmierzyłam zależność intensywności luminescencji od gęstości mocy pompy, a także czasy narostu i zaniku PA dla jonów Tm^{3+}. Niniejsza rozprawa doktorska

zagłębia się również w fundamentalne zasady stojące za PA w nano- i mikrokryształach, badając rolę rozmiaru, składu, matryc i struktury kryształów w optymalizacji tego procesu. Ponadto, omawiałam mechanizmy, dzięki którym PA może być inicjowana i kontrolowana w tych kryształach. Dodatkowo zbadałam wpływ wielkości kryształu, stężenia domieszki w mikrokryształach, oceniłam wpływ różnych matryc i grubości powłoki w nanokryształach na emisję PA w jonach Tm^{3+}. Ponadto, po raz pierwszy potwierdziłam występowanie PA w nanokryształach $LiYF_4$ domieszkowanych jonami Tm^{3+}. Co więcej, zbadałam jak obecność nanoprętów złota na powierzchni kryształów wpływa na emisję PA. Oprócz tego, sprawdzałam również zachowanie PA w nanokryształach $NaYF_4:Pr^{3+}$ współdomieszkowanych Yb^{3+} przy długości fali 852 nm oraz wpływ temperatury na widzialną emisję PA. Ponadto zweryfikowałam wpływ temperatury na anty-Stokesowską emisję w kryształach domieszkowanych jonami Nd^{3+} przy wzbudzeniu długością fali 1059 nm.

Możliwość obserwacji PA jest szczególnie interesujące w nanokryształach i mikrokryształach ze względu na ich unikalne właściwości zależne od rozmiaru. Te małe struktury krystaliczne, o średnicy od kilkunastu nanometrów do kilkunastu mikrometrów średnicy/długości, wykazują niezwykłe właściwości optyczne, które czynią je idealnymi kandydatami do wykorzystania zjawiska PA w nano-bio-technologii. PA może być zastosowana m.in. w (bio)detekcji, (bio)obrazowaniu, optoelektronice, optycznym przetwarzaniu sygnałów lub optycznych obliczeń. Materiały wykazujące PA mogą również poprawić rozdzielczość optyczną w mikroskopach fluorescencyjnych i służyć jako luminescencyjne nanotermometry o wysokiej względnej czułości temperaturowej. Niektóre z wymienionych zastosowań również wchodziły w zakres moich badań w rozprawie doktorskiej.

Podsumowując, w ramach moich obowiązków związanych z przygotowywaniem rozprawy doktorskiej, zajmowałam się projektowaniem układu optycznego. Dodatkowo, prowadziłam badania spektroskopowe, skupiając się na charakterystyce PA w nano- i mikrokryształach. Ponadto, analizowałam ich zdolność do zastosowań w dziedzinie termometrii luminescencyjnej czy obliczeniach komputerowych.

4. Theoretical introduction

4.1. Chemical, physical and optical properties of lanthanides

Lanthanides, the word is derived from the Greek word lanthaneien, meaning “lying in hiding” [2]. Lanthanides are metals, which belong to the sixth period and the 3rd group of the periodic table. Lanthanides are 16 elements (Lanthanum [La], Cerium [Ce], Praseodymium [Pr], Neodymium [Nd], Promethium [Pm], Samarium [Sm], Europium [Eu], Gadolinium [Gd], Terbium [Tb], Dysprosium [Dy], Holmium [Ho], Erbium [Er], Ytterbium [Yb], Lutetium [Lu]) with atomic numbers from 57 to 71 [3]. They have, to varying degrees, a filled 4f electron shell (without Lanthanum). With increasing charge of the nucleus (57-71) the number of electron shells is preserved, and only the number of valance electrons is increasing correspondingly [4]. This results in a greater electrostatic attraction of electrons by the nucleus, and consequently the radii of the atomic and ionic - decrease (lanthanide contraction) [5][6]. Electron configuration of lanthanides [Xe] 6s2 4fn (and 5d1 sometimes) is associated with the characteristic for these elements gradual filling of the 4f subshell, which is shielded by the filled 5s and 5p subshells of lower energy. Together with the scandium group (yttrium and scandium) they are called rare earth elements (REE) [7]. Lanthanides have very similar chemical properties to each other, which resulted in difficulties in their discovery and separation. Lanthanides are divided into a subgroup of cerium so-called light lanthanides (Ce, Pr, Nd, Pm, Sm, Eu, Gd) and a subgroup of terbium so-called heavy lanthanides (Tb, Dy, Ho, Er, Tm, Yb, Lu). All lanthanides occur at the III degree of oxidation. The most stable electron structures on the third oxidation state show: La^{3+}, due to the lack of electrons on the 4f subshell, Gd^{3+}, which has a half (7) filled 4f subshell, and Lu^{3+}, z 14 electrons on the 4f subshell Sm, Eu Tm and Yb can also occur on the II degree, and Ce, Pr, Nd, Tb, Dy on the IV degree of oxidation [8].

The energy of radiation quanta (absorption or emission) in the optical range in lanthanide ions occur on the 4f subshell, which is maximally filled (14 electrons) for Lutetium. The 4f electrons are the electrons of the f orbital in the fourth quantum level. There are a total of 7 f orbitals, with a maximum of two electrons associated with each, giving a total of 14 electrons [4].

The electron configurations of the elements and triple-positive lanthanide ions with ground state are shown in the Table 1.

Table 1. The electron configuration.

lanthanide symbol	Configuration electron of atoms	Ln^{3+} configuration	Ground State
La	[Xe] $5d^1\ 6s^2$	$4f^0$	$^1S_0$
Ce	[Xe] $4f^1\ 5d^1\ 6s^2$	$4f^1$	$^2F_{5/2}$
Pr	[Xe] $4f^3\ 6s^2$	$4f^2$	$^3H_4$
Nd	[Xe] $4f^4\ 6s^2$	$4f^3$	$^4I_{9/2}$
Pm	[Xe] $4f^5\ 6s^2$	$4f^4$	$^5I_4$
Sm	[Xe] $4f^6\ 6s^2$	$4f^5$	$^6H_{5/2}$
Eu	[Xe] $4f^7\ 6s^2$	$4f^6$	$^7F_0$
Gd	[Xe] $4f^7\ 5d^1\ 6s^2$	$4f^7$	$^8S_{7/2}$
Tb	[Xe] $4f^9\ 6s^2$	$4f^8$	$^7F_6$
Dy	[Xe] $4f^{10}\ 6s^2$	$4f^9$	$^6H_{15/2}$
Ho	[Xe] $4f^{11}\ 6s^2$	$4f^{10}$	$^5I_8$
Er	[Xe] $4f^{12}\ 6s^2$	$4f^{11}$	$^4I_{15/2}$
Tm	[Xe] $4f^{13}\ 6s^2$	$4f^{12}$	$^3H_6$
Yb	[Xe] $4f^{14}\ 6s^2$	$4f^{13}$	$^2F_{7/2}$
Lu	[Xe] $4f^{14}\ 5d^1\ 6s^2$	$4f^{14}$	$^1S_0$

As can be seen from Table 1, behind the 4f subshell there are still, occupied by electrons, subshells 5s and 6s, which effectively shield from the environment the $4f^1$, $4f^2$, $4f^3$, $4f^4$, $4f^5$, $4f^6$, $4f^7$, $4f^8$, $4f^9$, $4f^{10}$, $4f^{11}$, $4f^{12}$, $4f^{13}$, $4f^{14}$ electrons responsible for the optical transitions of 4f. When talking about the rare earth elements, we often exclude lanthanum and lutetium because, as the most commonly encountered trivalent ions, they do not possess an optically active 4f subshell. Lanthanum, in fact, has no electrons in the 4f subshell at all, and in the case of Lutetium this shell is completely filled. Consequently, electronic transitions within the 4f subshell are physically impossible in these two cases. Despite the partially occupied 4f subshell, lanthanides have their 5s and 5p subshells occupied, which are farther from the nucleus than the 4f subshell. This effect is known as the lanthanide contraction [9]. It turns out that with an increase in atomic number, the strongest electrostatic attraction between the nucleus and electrons occurs precisely for the electrons in the 4f subshell. This means that they are located much closer to the nucleus than the 5s and 5p subshells (see *Figure 1*. The probability of finding *electrons*

4f, 5s, 5p and 5d as a function of distance from the nucleus [10]. Consequently, the 5s and 5p electrons create an effective shield, isolating the 4f electrons from the influence of the external matrix field .

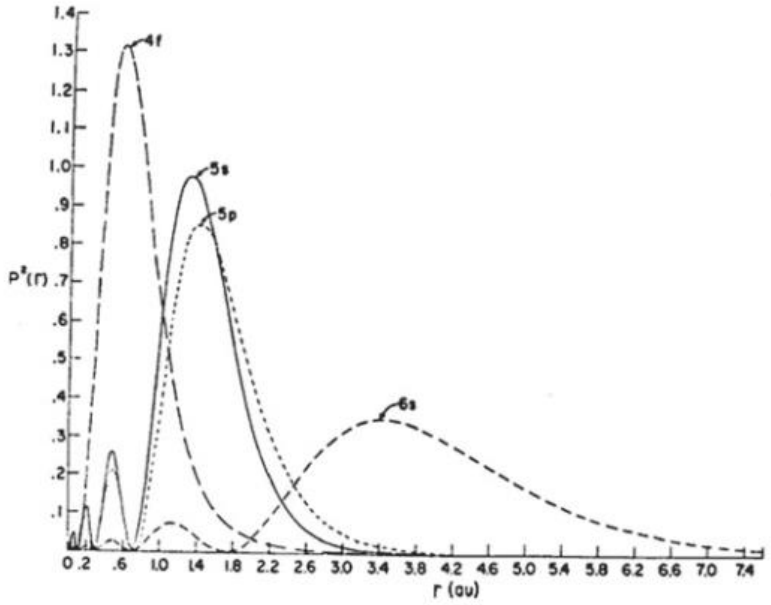

Figure 1. The probability of finding electrons 4f, 5s, 5p and 5d as a function of distance from the nucleus [10].

This strong screening from the matrix field is highly significant. Lanthanides can be successfully introduced to various materials, such as crystals, ceramics, and glasses, as the environment has minimal impact on the activator. As a result, there is no radical change in its spectroscopic properties when transitioning from one system to another.

Electron transitions in lanthanide ions can be divided into three types:

1. Charge-transfer (ligand-orbital f) transitions, consisting of the absorption of photons by the ligand, which is the donor, and transferring them to the subshell 4f Ln^{3+} ion, which emits radiation. These transitions are characterized by high intensity and spectral width, and appear on absorption spectra in the ultraviolet range. In addition, they are transitions allowed by Laporte's rule (there is a change in the parity of transitions of the electric dipole between energy levels) [11] .

2. Intra-configuration transitions, nf → (n +1) d, mostly 4f - 5d observed for Ce^{3+} ions and Pr^{3+}, these transitions are allowed transitions, characterized by high intensity in the UV range.

3. Intra-configurational transitions of lanthanide ions are transitions between individual levels within the split 4f subshell. The splitting (removal of degeneracy) of the 4f levels results from three interactions: (I) Coulombic interactions, (II) Russell-Saunders coupling, and (III) the influence of the crystal field (*Figure 2*). These transitions, as transitions between levels of the same parity, are forbidden by Laporte's rule and should not be observed. However, the mixing of 4f orbitals with energetically close 5d orbitals and coupling with lattice phonons partially lift the selection rules. By their forbidden nature, the lifetimes of excitation levels are long, allowing ESA and contributing to the possibility of obtaining PA**.** Intra-configurational transitions correspond to narrow (FWHM of around 10 cm^{-1}) and low-intensity absorption/emission bands [12].

The specific energy structure of rare earth ions is due to a series of interactions that are the cause of successive splitting of energy levels. The strongest interaction is the Coulomb interaction or electrostatic interaction, which is the sum of the interactions of the positively charged of the positively charged nucleus and the electrons carrying the electric charge on the internal, closed subshells (the electron configuration of xenon). Due to the presence of a partially filled 4f orbital, these ions have a high charge density, leading to significant electron-electron and electron-nucleus interactions. These interactions cause the energy levels of lanthanide ions to split, resulting in the loss of degeneracy. The degree of splitting depends on the specific lanthanide ion and its charge state. Coulomb field causes fission with energy on the order of 10000 cm^{-1}.

In order to characterize factors causing the splitting of the energy levels it is necessary to use the vector model of the atom. In the model this model, the angular momenta of the electrons are assumed to add to each other in a vector, giving resultant orbital angular momentum vector $\vec{L}$:

$$\vec{L} = \sum \vec{l}\, i$$

The spin vectors add up to give the resultant spin vector:

$$\vec{S} = \sum_{i} \vec{S}$$

The sum of the two vectors gives the total angular momentum of all electrons in the atom.

$$\vec{J} = \vec{L} + \vec{S}$$

All three of these summed momenta are quantized:

$$|\vec{S}| = \sqrt{S(S+1\hbar)}$$

$$|\vec{L}| = \sqrt{L(L+1\hbar)}$$

$$|\vec{J}| = \sqrt{J(J+1\hbar)}$$

This gives us the quantum numbers describing all the electrons in the atom. L is an orbital quantum number taking the values 0, 1, 2, 3, 4, 5, 6. In spectroscopy instead of numbers, to describe the orbital quantum number, letter designations: S, P, D, F, G, H, I [13].

The value of the orbital quantum number extended by additional subshells introducing the electronic unit and corresponding to the shape of the orbital.

S is a spin quantum number that can take the values 0, 1/2, 1, 3/2, ... S number is associated with the concept of multiplicity, which is defined as 2S+1.

J is the quantum number of total angular momentum and can take the following

values: J=(L+S), (L+S-1), (L+S-2),..., |L-S|...

Spin-orbit coupling, called Russel-Saunders coupling, arises from the interaction between the intrinsic spin angular momentum of electrons and their orbital angular momentum. In lanthanide ions, the 4f electrons experience substantial spin-orbit coupling due to their relatively high atomic number. This coupling further lifts the degeneracy of energy levels within the 4f electron shell. Spin-orbit coupling has significant effects on the electronic structure, energy levels, and spectral properties of atoms and ions.

Crystal field effects arise from the interaction between the electrons in the lanthanide ion and the surrounding ligands or crystal lattice. When lanthanide ions are incorporated into a crystal structure, the symmetry of their environment affects the energy levels of their electron orbitals. This results in the splitting of energy levels are known as the crystal field splitting, which further modifies the electronic structure of lanthanide ions. The nature of this splitting depends on the coordination geometry around the lanthanide ion.

Of the types mentioned, 4f - 4f transitions are the focus of our research. Due to their forbidden nature, the main factor affecting the electrons of the lanthanides are electrostatic and, to a lesser extent, magnetic interactions [14]. As already mentioned, as a result of the shielding of 4fn electrons through the 5s and 5p, the surrounding of Ln^{3+}

ions has little effect on the splitting of energy levels. However, it causes the splitting of individual multiplets into so-called Stark levels. The degeneracy of these levels depends on the symmetry of the surrounding, such as the matrix; the lower the symmetry of the crystal lattice, the lower the splitting of the multiplets. Precisely, because of the nature of 4f - 4f electron transitions in Ln^{3+} ions, the spectra of luminescence are characterized by narrow bands, with low spectral width [15][16]. The narrowness of these bands is a result of the well-defined energy levels due to the Stark effect and weak spin-orbit interactions. Each ion is characterized by a specific distribution of bands on the emission spectra, with a specific wavelength, so that ions can be distinguished by spectrometric measurements. In addition, transitions from excited to ground states are very slow, they can last even a few milliseconds, which is of particular importance for the practical application of compounds with lanthanide ions. Thanks to the relatively long-lived transitions in lanthanide ions, processes such as excited state absorption (ESA) and CR can take place. These are crucial processes for the occurrence of efficient PA. F-f-electrons are not involved in bond formation, besides allowing for very high photostability. there are usually several hundred/some thousands of activator ions in a single NC, and they do not show blinking.

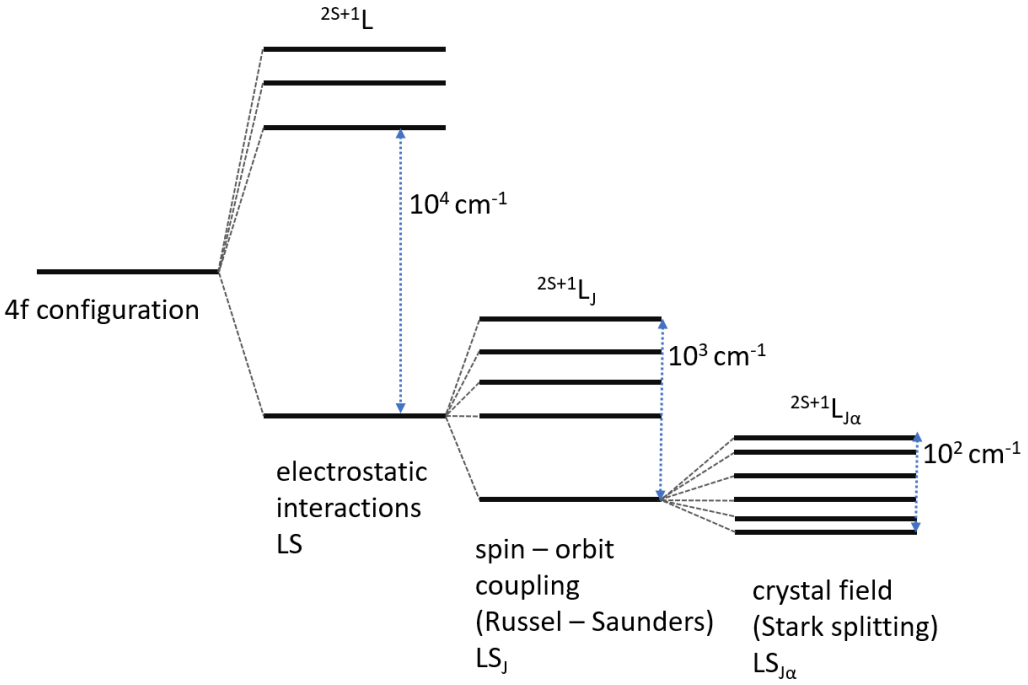

Figure 2. Electron structure of lanthanide ions. From left- electrostatic interactions, spin-orbit coupling, crystal field as factors affecting the degeneracy of levels along with cleavage values [17].

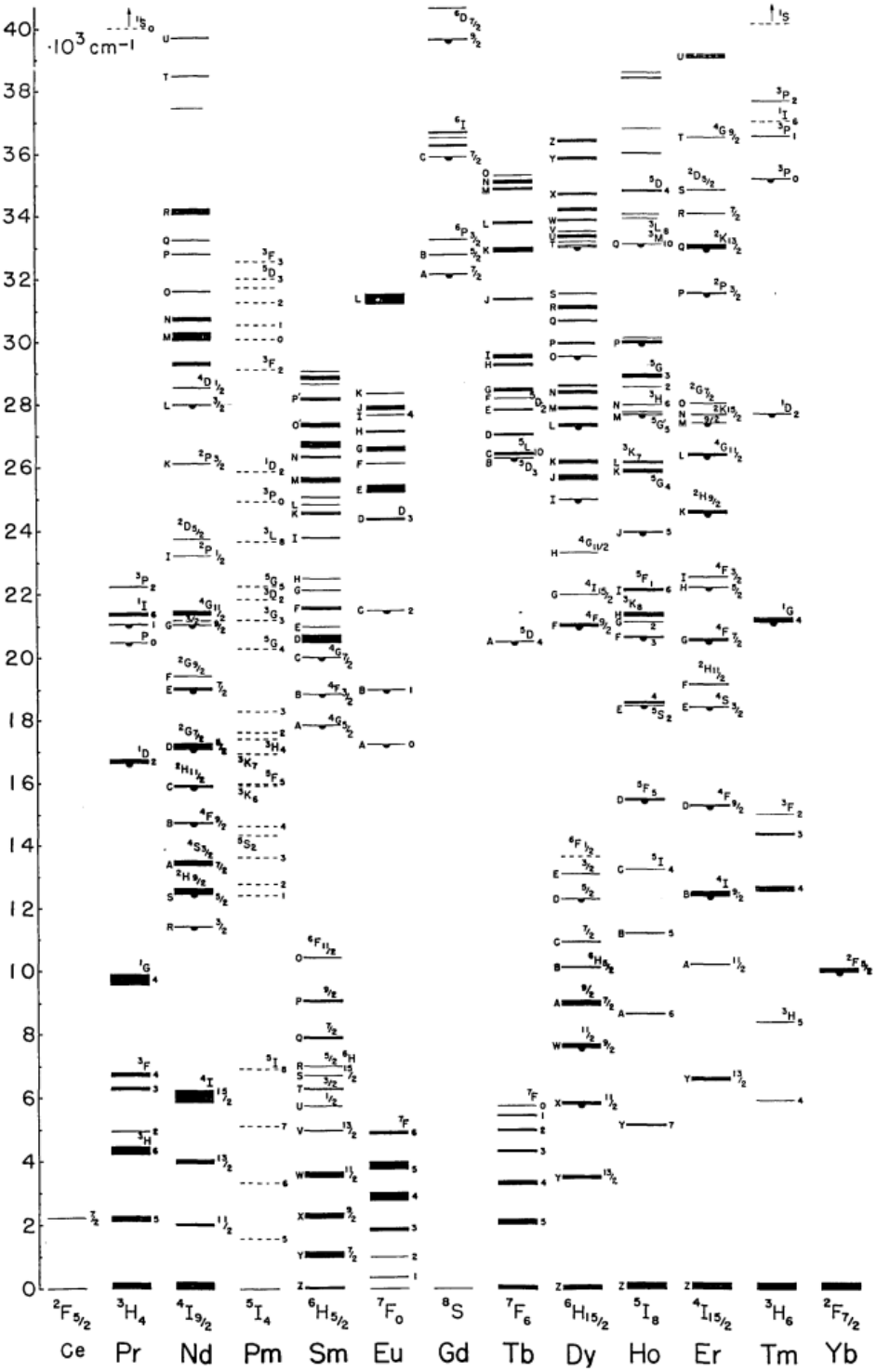

Figure 3. Dieke's diagram of relative (to the ground state) energy levels in trivalent lanthanides in $LaCl_3$ crystal [18].

Dieke's diagram (*Figure 3.*) is a graphical representation of the energy levels and transitions of lanthanide ions (rare earth elements). It is a useful tool for understanding

the spectral properties and behavior of lanthanides, particularly in the context of luminescence and spectroscopy. The diagram was first proposed by Gerhard Dieke.

Hund's rules

Hund's rule allows to determine the quantum numbers and thus the base term. The term with the lowest energy has the highest multiplicity [19]. The fundamental term corresponds to the largest in a given electron configuration, the value of S and the largest, corresponding to the assumed S, the value of L. Among the terms with equal multiplicity, the term with the largest value of the quantum number L has the lowest energy. For multiplets with the same values of S and L, the rules to determine the lowest energy configuration are following: in the case of electron configurations less than half occupied, the multiplet with the smallest value of the number J, where J = |L - S|. In the case of electron configurations occupied more than half, the multiplet with the largest value of J number where J = L+S [20].

For lanthanides that have valence electrons on the 4f subshell of the S, L and J value of a given term, is calculated as follows [21].

$$S = \frac{n}{2}; \quad L = \frac{n(7-n)}{2}; \qquad J = |\, L - S \,| \;\; for\; n \leq 7$$

$$S = \frac{14-n}{2}; \quad L = \frac{(14-n)(n-7)}{2}; \quad J = \; L + S \;\; for\; n > 7$$

Where n is the number of electrons on subshell 4f.

According to Laporte's rule, electric dipole transitions are allowed only between terms with different parity. All terms within the 4f subshell have the same evenness. By virtue of the above rule, transitions inside the 4f configuration are forbidden. As a result of the interaction environment of the ion, which does not exhibit inversion symmetry, the electron structure of the ion is disrupted and doped states of opposite evenness appear. Due to this interaction, transitions between terms of the 4f subshell are observed.

4.2. Application of lanthanide compounds

Lanthanides have a wide range of applications and have become increasingly important in modern technologies, making them a vital part of our daily lives. Their unique properties make them useful in a variety of applications, ranging from electronics to medicine [22].

One of the most significant applications of lanthanides is in the field of electronics. These elements are used in the production of electronic devices, including smartphones, computers, and televisions. Europium are used in the manufacture of touchscreens and cerium is used to polish smartphones during production. Besides cerium oxide is used for decolorizing and precision polishing of glass. Lanthanides are used in the production of computer hard drives, as well as in the production of LCD screens (cerium and neodymium). They are also used in the production of high-performance magnets used in electric motors and generators.

Lanthanide ions, such as Nd^{3+} and Ho^{3+}, are commonly used as dopants in solid-state laser materials. Nd:YAG (neodymium-doped yttrium aluminum garnet) and Ho:YAG (holmium-doped yttrium aluminum garnet) lasers are examples of widely employed lanthanide-based solid-state lasers. Er^{3+} and Yb^{3+} are commonly used lanthanides in fiber lasers. Erbium-doped fibers are employed for applications in the telecommunications industry, particularly in amplifiers for optical communication systems. Ytterbium-doped fibers are known for their high-power and efficient operation.

Lanthanides are also used as catalysts in a variety of chemical reactions. They are particularly useful in the chemical industry, where they are used in the production of petrochemicals, plastics, and other materials. For example, lanthanides are used as catalysts in the production of polyethylene, a material used in the production of plastic bags.

Cerium and samarium are used as burnable neutron absorbers in nuclear reactors to control the rate of nuclear reactions.

Lanthanides also have important medicinal applications. Lanthanides are used as contrast agents in magnetic resonance imaging (MRI) scans (gadolinium) [23]. They are also used in the treatment of some cancers. Additionally, lanthanides find applications in the

treatment of certain cancers, indicating a growing significance in cancer diagnosis and therapy. Lanthanide complexes are increasingly important in cancer treatment and diagnostics. They have applications as cytotoxic agents, in photodynamic therapy, and in biosensing and bioimaging [24].

Lanthanides are also used in lighting applications. They are used in the production of energy-efficient lighting, including solid-state lighting: semiconductor light-emitting diodes (LEDs), polymer light-emitting diodes (PLED) and organic light-emitting diodes (OLED)[25] . Solid-state lighting uses electroluminescence, unlike incandescent lamps, which use thermal radiation [26][25].

Neodymium is used to make very strong magnets, cerium is a component of pyrophoric alloys. Holmium has the highest magnetic strength among all elements, and therefore, it is used to create the strongest artificially generated magnetic fields. In addition, admixtures of lanthanides significantly increase the strength of aluminum. Lanthanides are also used in the lighting industry for the manufacture of incandescent shirts, as well as in the ceramics and glass industries. In nuclear technology europium and gadolinium are used for absorbing neutrons. Rare earth ions placed in suitable matrices, due to their optical properties, are used as luminophores, amplification centers and active centers of solid state lasers.

Electronic transitions in optical spectroscopy

Electronic transitions in optical spectroscopy encompass the investigation of the interplay between matter and electromagnetic radiation across the IR, visible (VIS), and ultraviolet (UV) regions. Photons within this range possess energies that align with the energy levels of atoms, ions, or molecules. The absorption or emission spectrum of a material, when scrutinized, offers valuable information about its electronic structure. This entails the understanding of how electrons transition between different energy states, shedding light on the material's composition and behavior. In addition to this, information about the crystalline nature, crystallographic symmetry and the strength of the crystal field can be obtained.

4.3. Interaction of light with matter

A photon can be absorbed by a material medium if its energy is equal to the energy difference between the energy levels of the medium (*Figure 4 a)*). This is described by Planck's equation: $\boldsymbol{h\nu = \Delta E}$, where h is Planck constants, ν is photon's frequency. The reverse process is also possible [13]. When a medium goes from an excited state to a state of lower energy it emits a photon (*Figure 4 b)*).

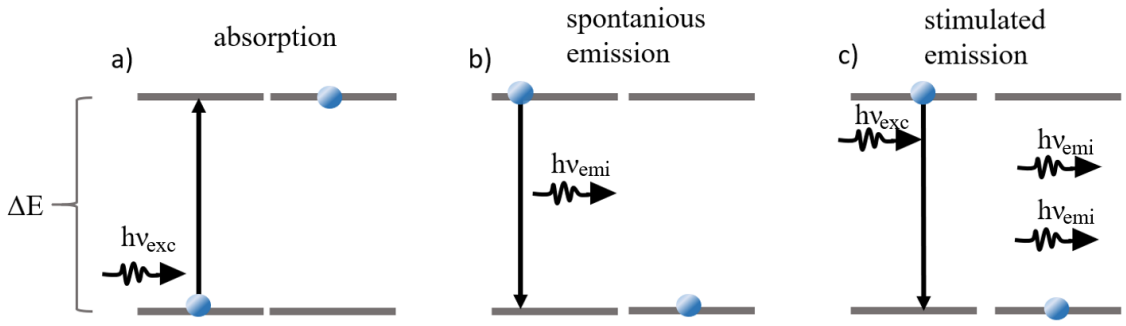

Figure 4. Interactions of light with matter. Scheme of absorption a), spontaneous emission b) and stimulated emission c).

In most known emitters, such as quantum dots or organic dyes, a basic Stokes emission - fluorescence is observed. This process involves the absorption of excitation energy ($h\nu_{exc}$) followed by the emission of a lower-energy photon ($h\nu_{emi}$). It occurs relatively quickly, typically within a timescale of 10^{-10} - 10^{-8} s. However, in certain structures like organic collagens or inorganic crystals, nonlinear anti-Stokes phenomena can also be observed, which describes the behavior of light in nonlinear media, that is, in which the dielectric polarization responds nonlinearly to the electric field. Such phenomena, like second harmonic generation (SHG) and third harmonic generation (THG), manifest in the generation of light waves with higher frequencies ($h\nu_{exc} < h\nu_{emi}$), resulting from higher-order susceptibilities of the medium ($\chi^{(2)}$ and $\chi^{(3)}$, respectively). The observation of these phenomena became possible with the invention of very high intensity, polarized, and coherent light sources, specifically lasers. In lasers, an electric field with amplitude E(ω) traveling through a medium with nonlinear susceptibility tensor χ^2 can be described in terms of polarization at double frequency, $\boldsymbol{P(2\omega) = \epsilon_o \chi^{(2)} E^2(\omega)}$ [27]. The occurrence of these processes is relatively rare (probability ~10^{-11}) and requires noncentrosymmetric crystals and precise phase matching. Another type of anti-Stokes processes involves the

energy of the resulting photons being higher than the energy of the incident photons ($h\nu_{exc} < h\nu_{emi}$), but not higher than their sum. These are 2- and 3-photon absorption processes, where the excited state of the emitter is pumped by the simultaneous absorption of 2 or 3 photons. Although 2- or 3-photon microscopy is feasible and used to enhance imaging depths and spatial confinement, these mechanisms also require high power density or peak energy excitation using ultrafast pulses. On the other hand, rare earth (RE) ions exhibit unique properties that enable several other anti-Stokes mechanisms. The rich energy level structure of the multiplets in lanthanides, along with energy transfers, phonon assistance in mismatched energy transfers, and forbidden transitions leading to long-living metastable levels, allows neighboring lanthanide ions to interact and exchange energy. This enables other multiphoton anti-Stokes mechanisms. These mechanisms are described in a subsequent chapter.

4.4. Anti-Stokes emission

Anti-Stokes emission refers to a process in which a photon is emitted from an atom or molecule with higher energy than the photon that was initially absorbed by the system. This phenomenon is associated with energy upconversion, and it typically occurs in situations where the system gains additional energy from external sources or experiences certain environmental conditions that elevate the emitted photon's energy level. This phenomenon is the opposite of Stokes emission, where the emitted light has a lower energy than the excitation light, because there are energy losses in the form of heat. The system heats up, vibrations of the crystal lattice occur and phonon emission occurs. Anti-Stokes emission is rare and usually requires low-energy photon excitation sources such as infrared lasers.

Up-conversion is the process by which an atom/molecule transitions to a state with an energy higher than that of the excitation quantum. The effect of this phenomena may be precisely anti-Stokes emission [28][29]. *Figure 5* shows the energy diagram of the ESA mechanism. The first stage of this mechanism is the resonant absorption of a photon of energy $h\nu_1$ with a probability R_1 and the transition of the ion from energy state 1 to state 2. The ion located in excited state 2 can absorb another photon of energy $h\nu_2$ with probability R_2. Under conditions where the energy differences between levels 1 and 2 and

2 and 3 are equal, excitation conversion can be obtained by absorption from the excited state when excited by a single beam of radiation. ESA can be described by the equations of occupancy of energy levels. For the above energy scheme, the equations are as follows:

$$\frac{dn_1}{dt} = -I_1 R_1 n_1 + W_2 n_2 + aW_3 n_3$$

$$\frac{dn_2}{dt} = -I_2 R_2 n_2 + I_1 R_1 n_1 - W_2 n_2 + bW_3 n_3$$

$$\frac{dn_3}{dt} = +I_2 R_2 n_2 - W_3 n_3$$

where W_2 and W_3 representant the emission probabilities from level 2 and 3 respectively, while a and b denote the fluorescence branching ratios. Additionally, n_1, n_2, and n_3 describe the number of ions in a specific energy state.

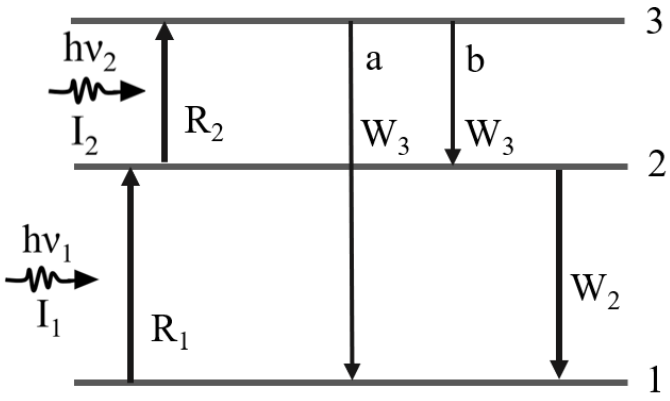

Figure 5. Energy upconversion scheme.

There are several groups of materials that exhibit efficient upconversion effects. One of these groups consists of lanthanide ions used as dopants in crystalline matrices. They are good candidates for enabling the upconversion process because most of them have appropriately matched metastable energy levels. Electronic transitions mainly occur in the 4f subshell. Due to its effective shielding by neighboring subshells, it is less influenced by the crystal field of the matrix. Therefore, disruptive interactions such as electron-photon interactions or multiphonon relaxation will be limited, which is crucial for the efficiency of the upconversion process. There are various upconversion mechanisms, and they will be briefly discussed and compared.

Excited state absorption

Absorption from the excited state involves the absorption of energy by an ion already in the excited state. Such a level can be occupied by electrons, for example, as a result of vibrations of the crystal lattice (phonons). Unlike classical absorption (ground state absorption [GSA]), this process does not occur from the ground state. The ESA process can adversely affect the emission, for example, where it is broadband. With pumping, some energy will be lost to additional absorption to higher energy levels, instead of enhancing the emission.

The population of excited states in ESA is achievable through single-ion processes. One such process is ground state absorption (GSA), distinguished by its GSA cross-section. If a photon is absorbed within a time frame shorter than the decay constant, absorption from the excited state (ES) becomes feasible, ultimately leading to the population of ES2. Generally, the ESA cross-section of ES1 differs from that of the ground state (GS). In cases where GSA does not lead to its bleaching condition, ES is fulfilled.

Energy transfer upconversion

One of the most common and highly probable processes for upconversion emission is energy transfer upconversion (ETU) [30]. The basic scheme of the ETU process is depicted in *Figure 6*. In general, ETU relies on the cooperation of at least two sensitizer ions, which absorb the excitation wavelength and transfer it to another dopant – activator (ion B)[16]. This two-step process leads to the population of the excited state (ES2) of ion B. One of the most prevalent systems where ETU upconversion occurs is the Erbium-Ytterbium (Er-Yb) system [31]. In this system, the Yb ion acts as a sensitizer, enabling visible range emissions from the excited state of Erbium. Yb plays a crucial role due to two key features of this ion as a sensitizer. Firstly, the energy level scheme of Yb consists of only two states, resulting in a relatively high absorption cross-section for the 1st transition. Secondly, another advantage of this ion is its relatively long radiative lifetime, typically in the range of milliseconds [16][32].

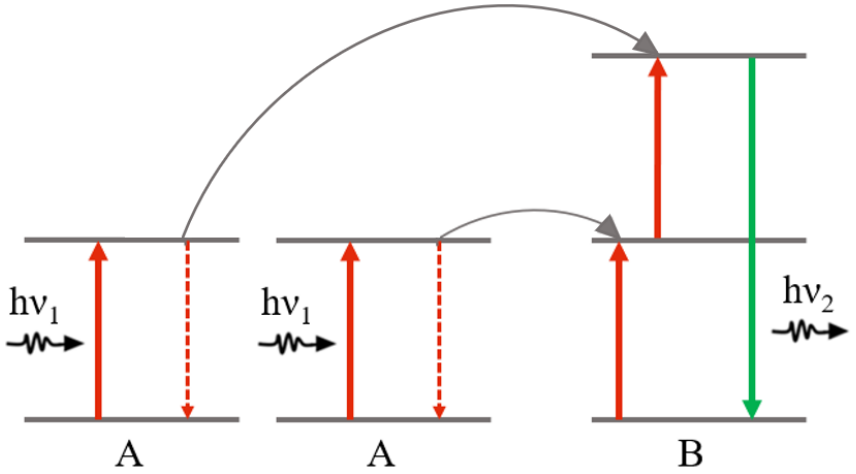

Figure 6. Energy scheme of energy transfer upconversion (ETU).

Cross relaxation

CR is a frequently observed process in Ln^{3+}-doped matrices, where energy is exchanged between neighboring lanthanide ions with the same or closely matched energy levels [16]. If in the energy system of a pair of ions there are several levels between which there is an equal or very close energy gap, then energy transfer can occur between such levels. Such a process is called CR. One of the ions is in a higher energy state and the other is in a lower or basic state. Such two ions after energy exchange have averaged energies and both are in an excited state. CR can cause a decrease in the occupancy of the higher lying energy levels, which will consequently lead to a weakening of the emission (thus it is often called also concentration quenching effect, as increased concentration of dopants makes them stay closer to each other and thus enhances the CR interaction between them). This process can also cause an increase in one emission at the expense of another. It also contributes to the occurrence of an energy looping [33], by increasing the population of the metastable level and absorption occurs more efficiently, which is necessary to PA. The concentration quenching effect, caused by shortening the Ln-Ln distance through increased doping, limits the number of acceptable activators per unit volume of the matrix. Concentration quenching also occurs in low phonon matrices like fluorides, where even a few percent of activator doping leads to significant quenching. Although in low phonon matrices, the main issue lies with multiphonon relaxation (MPR). In most cases of upconversion, Er^{3+} or Tm^{3+} ions serve as activators, while Yb^{3+} ions play the role of sensitizers. Optimal upconverting couples include 2% Er and 20% Yb or 0.2% Tm and

20% Yb, although higher doping levels have also been studied. The presence of cross-relaxation processes, which double the population of intermediate energy levels, is crucial for observing another type of anti-Stokes emission known as PA emission [30].

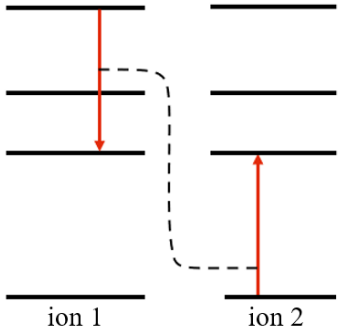

Figure 7. Scheme of cross relaxation process.

Two photon absorption

Two photon absorption (TPA) is nonlinear process. It occurs when two photons of different or identical frequencies are absorbed simultaneously, leading to the excitation of the atom/molecule from one state to a higher energy state [34]. The concept of TPA was first introduced by Maria Goppert-Mayer in 1931 [35], and its experimental observation became possible with the development of powerful lasers in the 1960s. The invention of the laser allowed the first experiment to confirm TPA, two-photon excited fluorescence was detected in a europium-doped crystal [3]. The primary distinction between TPA and ESA lies in the nature of their intermediate states. In TPA, the intermediate state is a virtual state, while in ESA, it is a metastable state. Consequently, the probability of TPA occurring is considerably lower compared to ESA.

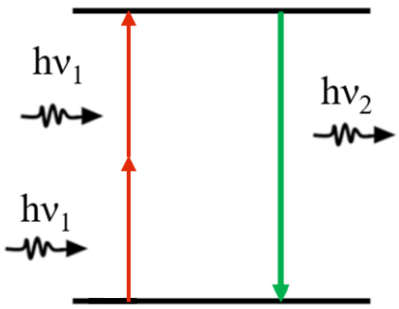

Figure 8. Schemes of a) two photon absorption (TPA).

Cooperative luminescence

Cooperative luminescence can be described as a collective de-excitation process involving a pair of ions in an excited state, resulting in the emission of a photon with an energy equal to the sum of the energies of both ions. In contrast to cooperative sensitization, cooperative emission occurs from a virtual energy state. For cooperative luminescence to occur, two ions must be positioned in close proximity to form an ion pair. Consequently, the intensity of cooperative luminescence is highly dependent on the distance between the ions. Nakazawa and Shionoya [36] first reported the highest probability of cooperative luminescence in $YbPO_4$. Since then, extensive research has been conducted on the cooperative luminescence of Yb-Yb pairs [37][38][39]. The configuration diagram of Yb ions consists of only two states: ground and excited, separated by an energy gap of approximately 10,000 cm^{-1}. The emission band of Yb ions falls within the near-infrared (NIR) spectral range, typically around 950-1050 nm. Cooperative luminescence of Yb-Yb pairs occurs at an energy level twice that of the Stokes emission from Yb and exhibit twice shorter lifetimes of ES as compared to the lifetime of single Yb^{3+} ion.

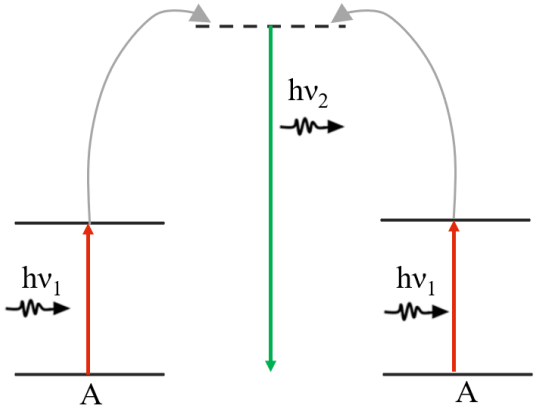

Figure 9. Energy scheme of cooperative luminescence.

Cooperative sensitization upconversion

The cooperative sensitization upconversion process shown in the *Figure 10* is quite similar to the ETU process. However, the key distinction lies in the absence of an intermediate energy state for the donor, to which energy from the acceptor can be transferred [16]. To populate the excited state ES2, cooperative energy transfer requires the contribution of energy from two acceptor ions. An example of such an energy transfer

can be seen in the Yb^{3+}, Tb^{3+} system, where Tb, as the donor, lacks an *f* energy state corresponding to ES2 [40][41]. Therefore, the sum of the energy absorbed by the acceptor ions allows them to bridge this energy gap. In some cases, this bridging is also facilitated by phonon-assisted processes [42]. Phonon-assisted processes involve the interaction between excitation photons and lattice vibrations, or phonons. In the Yb^{3+} and Tb^{3+} upconversion system, Yb^{3+} ions act as donors, and Tb^{3+} ions act as acceptors. The goal is to efficiently transfer energy from Yb^{3+} to Tb^{3+} ions for upconversion. In the absence of an intermediate energy state for Tb^{3+} ions, phonon-assisted processes become crucial. The simultaneous transfer of energy from two Yb^{3+} ions to a single Tb^{3+} ion is facilitated by the interaction with lattice vibrations, known as phonons. These phonon-assisted processes play a pivotal role in bridging the energy gap, enabling an efficient transfer of excitation energy to the Tb^{3+} ion.

It occurs when two A ions simultaneously transfer their excitation energy to the D ion, which has no intermediate level, comparable to the excitation of the A energy level [36].

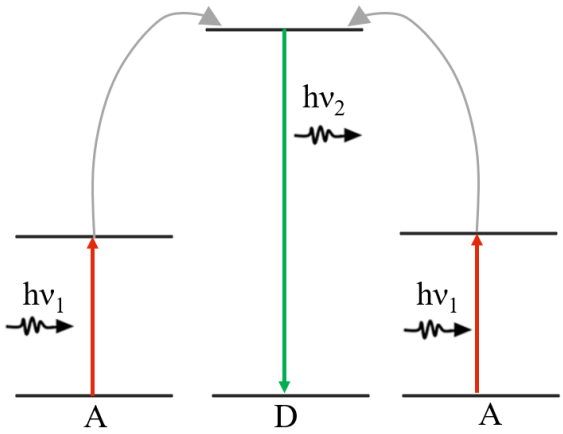

Figure 10. Energy scheme of cooperative sensitization.

Photon avalanche

PA is yet another upconversion process, which exhibit significantly (as compared to other UC processes) higher increase of luminescence intensity (I_L) by up to several orders of magnitude in response to very small increase of photoexcitation laser power (I_P). The sudden surge in luminescence intensity occurs above a certain threshold laser excitation power. One obtains a plot of luminescence intensity against the power density of an S-shaped pumped laser, which can be described by the power law: $I_L = (I_P - I_{TH})^S$ where S means a slope of the curve.

This phenomenon occurs in bulk dielectric materials that are doped with optically active lanthanide ions. PA phenomenon was first observed for the Pr^{3+} ion in $LaCl_3$ and $LaBr_3$ [1] matrices in quantum counters. This phenomenon was observed –in bulk materials (single crystals, fibers, glasses) and mostly at low temperatures [43]. However, it wasn't until 2021 that the phenomenon was observed in $NaYF_4$ nanocrystals doped with 8%Tm [44]. In order for PA to occur, the material must meet several criteria, such as: the presence of an intermediate ES, the existence of an efficient CR that sustains the occupancy of the metastable level from which efficient absorption from the ES occurs, matching the energies of the excitation photons with the absorption from the ES, meaning that the wavelength of the excitation light must be far from resonance with the absorption in the ground state and in resonance with the absorption in the ES [45]. In addition, the ratio of absorption cross section from the excited state (σESA) to cross section from the ground state (σGSA), defined as: $\beta = \frac{\sigma\mathrm{ESA}}{\sigma\mathrm{GSA}}$ must by higher than 10^4.

Exceeding a certain threshold of the power density of the excitation beam allows efficient absorption from the ES, which in turn sharply increases the intensity of luminescence. Each of the emitted photons has a higher energy than a single absorbed photon, but unlike in ETU where higher non-linearity means emission from blue-UV region, in PA the highly nonlinear emission occurs at the same (also NIR) wavelengths. In this context, avalanche photon emission is one of the most efficient, yet least understood mechanisms of upconversion. PA occurs when the system is excited by light that matches one of its ESA transitions, preferably starting from a level populated by cross-relaxation. The doubling of the population of this intermediate level through cross-relaxation leads to increased pump light absorbance by the ions, resulting in avalanche emission above a critical threshold pump power. CR can occur between ions of the same type (e.g., Tm^{3+}-Tm^{3+}) or between ESA-pumped ions and Yb^{3+} ions. In the latter case, energy is transferred from excited Yb^{3+} ions back to the intermediate level, doubling its population and resulting in Yb^{3+} - sensitized PA (SPA). Additionally, these concepts can be combined in complex systems, where a portion of the material is doped with Pr^{3+} and Yb^{3+} ions, leading to localized APA emission. The energy migrated by Yb^{3+} ions can then excite other ions (e.g., Ho^{3+} or Tm^{3+}) in another part of the material through ETU, resulting in energy migration PA (EMPA). Although PA only occurs in part of the material (e.g., the core of a nanocrystal), it powers the emission of other ions present in other part of the NP, exhibiting avalanche characteristics. The development of core-shell structures has

enabled the creation of advanced combinations of lanthanides, allowing for experiments with their properties. Otherwise, a homogeneous fusion of these elements could result in the quenching of light emission and the absence of PA phenomenon.

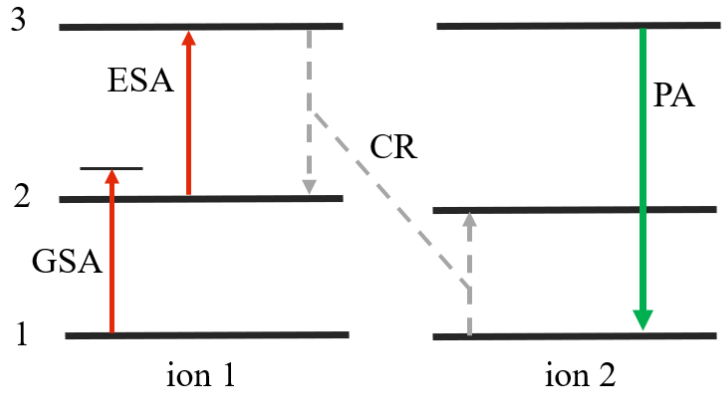

Figure 11. Energy scheme of photon avalanche process.

4.5. Photon avalanche in lanthanides ions

Pr^{3+}

The PA phenomenon, initially observed in Pr^{3+} ions doped into $LaCl_3$ and $LaBr_3$ [1] matrices, involves highly nonlinear changes in optical properties. This results in an avalanche-like increase in emitted light intensity when the laser excitation power surpasses a specific threshold. The mechanism behind PA includes energy looping between the lowest energetic levels of Pr^{3+}, creating a positive feedback loop that leads to gain. PA has been successfully demonstrated in various Pr^{3+}-doped hosts, including fibers, SiO glass fibers [46], $LiYF_4$ [47], ZBLAN fibers [48], Y_2O_3 [47], and BaY_2F_8 [49][50].

In co-doping scenarios with Yb^{3+} ions [47], PA can be achieved with lower concentrations of Pr^{3+} ions. The resulting emitting state typically involves the metastable $^3P_0$ level, leading to multiple emission peaks in the visible range. The observed emission peaks cover various colors, including blue, green, orange, and red.

The versatility of PA in different host materials, along with its ability to achieve enhanced emission with lower dopant concentrations, holds promise for various applications. The metastable $^3P_0$ level, serving as a common emitting state, opens avenues for practical utilization in diverse fields, making PA a subject of continued interest and exploration.

Nd^{3+}

In the case of neodymium, the phenomenon of PA was initially observed in Nd-doped $LiYF_4$ bulk crystal. The crystal was pumped at 603.6 nm, resulting in the anti-Stokes emission at 413 nm. This emission corresponds to the $^2P_{3/2} \rightarrow {}^4I_{11/2}$ transition, where energy looping occurs through the CR mechanism. This mechanism leads to an increased population of the $^4F_{3/2}$ metastable state after multi-phonon relaxation from higher levels [51]. A similar mechanism was also observed in Nd-doped $LiKYF_5$ single crystal. It is worth mentioning that a non-linear increase in emission intensity was observed in nanocrystalline powders of LiLa1-xNdxP_4O_{12} under NIR excitation at room temperature. The emissions were observed at 585, 656, 685, and 750 nm, corresponding to transitions: $^2G_{7/2} + {}^4G_{5/2} \rightarrow {}^4I_{9/2}$, $^2G_{7/2} + {}^4G_{5/2} \rightarrow {}^4I_{11/2}$, $^4F_{9/2} \rightarrow {}^4I_{9/2}$ and $^4F_{7/2} + {}^2S_{3/2} \rightarrow {}^4I_{9/2}$ [52]. However, the excitation wavelength used in this case (808 nm) was resonant with GSA transition in Nd^{3+}, raising questions about the PA origin of the observed emission. Similarly, Nd-doped $NdAlO_3$ nanocrystalline powders were known to exhibit bright yellow anti-Stokes emission under laser excitation at 808 nm. This emission occurred at high temperatures and under vacuum conditions. In this configuration, ytterbium ions served as sensitizers, absorbing 976 nm light, while Nd^{3+} ions acted as activators, resulting in unconventional emissions at various wavelengths[53]. Interestingly, under excitation at 976 nm, no emission from the $^4F_{3/2}$ level was observed, suggesting that phonon emission from Nd to Yb was more probable than phonon absorption from Yb to Nd. Power dependence measurements showed a nonlinear S-shape dependence (slope around 5), with the degree of nonlinearity increasing with the energy of the emitting state[52].

In $NdAl_3(BO_3)_4$ nanoparticles doped with Nd^{3+} ions, photon avalanche-like upconversion was also observed. This upconversion mechanism involved initial sideband ground-state absorption, leading to the population of the metastable $^4F_{3/2}$ level. After cross-relaxation looping, the population of the $^4I1_{5/2}\ldots_{11/2}$ state could be doubled, contributing to the enhancement of luminescence intensity through photon-avalanche-like emission. Various multicolor emission bands were observed and it was noted that non-radiative relaxations increased the temperature of the samples and simultaneously increased the luminescence intensity [54].

The PA-like process under excitation with 1064 nm was investigated, and an increase in luminescence intensity with temperature was observed [55]. The PA threshold also shifted to lower values of pump power density with increasing temperature. It is believed that energy transfer from Yb^{3+} ions, excited as activators, to Nd^{3+} ions facilitated the occurrence of ESA. Nd^{3+} ions have also found applications in luminescence thermometry [56], especially in bio-applications, as their emission and absorption bands do not overlap with water absorption.

Theoretical modeling of the PA phenomenon in Nd^{3+} pumped via ESA at 1064 nm shows great potential for applications in super resolution imaging. Additionally, due to the thermal dependences of the essential processes involved in PA, this phenomenon holds promise for thermometric utilizations. In particular, the single-band-ratiometric (SBR) luminescence thermometry approach, using the ratio of emission bands under GSA at 808 nm (corresponding to $^4I_{9/2} \rightarrow {}^4F_{5/2}$) and ESA at 1064 nm (ESA, corresponding to $^4I_{11/2} \rightarrow {}^4F_{3/2}$), shows potential for temperature measurement with sub-micron resolutions.

Tm^{3+}

Thulium ions are renowned for displaying blue, red, and NIR emissions. Blue emissions result from $^1D_2 \rightarrow {}^3F_4$ and $^1G_4 \rightarrow {}^3H_6$ transitions (around 455 nm and 480 nm, while NIR emission at 800 nm is observed for the $^3F_4 \rightarrow {}^3H_6$ transition. Thulium ions have been extensively studied for PA observations, with early demonstrations occurring at low temperatures in various bulk materials doped with Tm^{3+}.

PA phenomena in Tm^{3+} ions were initially demonstrated under low-temperature conditions in various bulk materials. These materials include $LiYF_4$ [57] crystal, YAP ($YAlO_3$)[58], YAG ($Y_3Al_5O_{12}$) [59] , LaF_3 YSO (Y_2SiO_5) single crystals, Y_2O_3 crystals [60], ZBLAN fiber [61], and fluoroindate glasses [62]. Typically observed after red or infrared photoexcitation, the PA emissions were in the blue range, with wavelengths around 480-486 nm and 450 nm.

Recently, the pure PA phenomenon was observed for the first time in $NaYF_4$: Tm^{3+}@$NaYF_4$ core-shell nanoparticles [44], even at room temperature. Different concentrations of Tm^{3+} ions were doped into the core, resulting in PA emissions around 800 nm under 1064 nm light excitation. The optimized architecture and quantum yield analysis identified 8% doped nanocrystals as optimal for super-resolution imaging, achieving resolutions significantly beyond the diffraction limit.

Ho^{3+}

The complex energy level system in Ho^{3+} facilitates several possible CR transitions, suggesting the potential for PA. Early demonstrations of PA in Ho^{3+}-doped materials date back to 1996 in ZBLAN glass [63], with subsequent reports in 1999 for various hosts (YAP crystal [64] and ZBLAN glass [65]). The mechanism involves ESA pumping from the metastable state ($^5I_7$) to $^5G_6$ + $^5F^1$ levels, resulting in green emission at 545 nm. Notably, the excitation line resonates with other transitions, complicating the identification of a single clear CR transition.

In the early 2000s [64][66], alternative approaches and materials such as $LiYF_4$ were explored for PA investigations in Ho-doped systems. Different excitation schemes, including 750 nm ESA excitation, were employed, revealing PA emissions at various wavelengths. Co-doping with Tm^{3+} ions and Yb^{3+} sensitization further improved system performance.

In sensitized PA, Yb^{3+} initiates the loop under weak ESA excitation (e.g., 746 nm). This process efficiently enhances the energy loop between Ho^{3+} pairs by transferring energy between Yb^{3+} and Ho^{3+} ions, leveraging their respective energy levels.

Furthermore, MPA was observed for Ho^{3+} ions using energy transfer between Yb^{3+} ions after excitation with 852 nm in a four-layer structure. This effective PA process transferred energy to Ho^{3+} ions, resulting in PA emissions at 541 nm and 646 nm. Notably, nanoparticles with single Ho^{3+} or co-doped with Ho^{3+} and Yb^{3+} did not exhibit PA emission under 852 nm excitation.

4.6. Applications of photon avalanche emission

Super resolution imaging

Optical microscopy provides profound insights into dynamic biological processes and cellular functions. However, conventional optical microscopes face limitations due to light diffraction. In the visible light spectrum, the diffraction limit restricts resolution to approximately half the photoexcitation wavelength in the lateral (X-Y) plane and three times as long along the optical axis (Z) [67]. Such magnification is not always sufficient for biological imaging. Resolution challenges become particularly evident when employing NIR excitation for deeper tissue penetration, which suffers less scattering and autofluorescence.

Two-Photon Microscopy offers improved tissue penetration, superior point spread function (PSF) confinement, and enhanced spatial resolution under NIR photoexcitation. However, it necessitates the use of powerful, expensive, and bulky femtosecond lasers due to the low 2- or 3-photon absorption cross-sections of fluorophores (whether endogenous or exogenously administered) [68][69] .

Recent advancements in far-field super-resolution techniques: Stimulated Emission Depletion (STED) microscopy, Stochastic Optical Reconstruction Microscopy (STORM), Photo Activated Localization Microscopy (PALM), 4Pi microscopy, and Structured Illumination (SIM) [70][71] have demonstrated the ability to surpass diffraction limits through clever optical design, innovative photon excitation/detection methods, specialized fluorescent labels, and dedicated data processing. For instance, STED operates on a concept, providing raw data akin to confocal microscopy images. However, it poses technical challenges involving the spatial overlap of excitation and depletion beam, issues with multiplexing (detecting different fluorescent labels within sample, require typically different wavelengths for stimulated and depletion beams) specialized probes with high stimulated emission cross-sections, high depletion excitation intensities leading to rapid photobleaching, and potential bioincompatibility. Despite significant progress in these areas over the last decade (e.g., multi-color STED [72][73]), researchers continue to seek alternative techniques and labels.

Other methods include:

1. Stochastic Optical Reconstruction Microscopy (STORM): Relies on stochastic activation and localization of individual fluorophores, allowing precise determination of their positions and subsequent image reconstruction.
2. Photoactivated Localization Microscopy (PALM): Similar to STORM, PALM uses photoactivatable fluorescent proteins to stochastically activate and precisely locate individual molecules.
3. 4Pi Microscopy: Employs two opposing objective lenses and a central illuminating lens, providing improved axial resolution by overlapping excitation and emission beams.
4. Structured Illumination Microscopy (SIM): Enhances resolution by projecting patterned light onto the sample and analyzing the resultant moiré pattern, enabling sub-diffraction imaging.

A method for PA-based super-resolution imaging was proposed in 2019 [74]. In contrast to STED, this approach utilizes a single excitation beam, eliminating the necessity for a second depletion beam. It effectively addresses the challenges of previous methods (no depletion beam as in STED, no complex hardware) using highly non-linear nanomaterials that are capable of converting light frequencies.

The paper demonstrates photon-avalanche single-beam superresolution imaging (PASSI) [75] on a single avalanche nanocrystal for different pumping powers. This is due to the fact that when the power of the excitation laser is finely tuned to be just above the PA threshold, the Gaussian-shaped excitation beam only has sufficient power in its central region to surpass the threshold. The sides of the Gaussian beam are too weak and practically do not excite the medium. Consequently, only the crystal in the maximum of the beam lights up, while the adjacent one, although seemingly within the beam's range, is excited below the threshold and does not emit.

Multi-photon imaging enhances light resolution following the equation: $\delta = \frac{\lambda}{2 \cdot NA \cdot \sqrt{N}}$, where δ is the resolution, λ is the excitation wavelength, NA is the numerical aperture, and N is the order of non-linearity. High nonlinearity of the process enhances optical resolution [74].

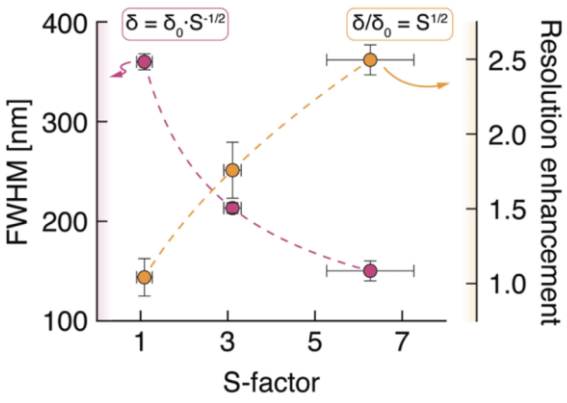

Figure 12. Comparison of changes in the full width at half maximum (FWHM) of the depicted spot with a changing parameter S (left axis), as well as the resulting increase in resolution (right axis); corresponding adjustments are also shown [75].

Photon avalanche lasers

Rare earth ions play a crucial role in laser techniques, offering significant advantages such as high stability, narrow emission lines, and long-lasting metastable electronic states. They also enable 3- and 4-level laser operations with various pumping sources and output wavelengths. Since the first laser utilizing upconversion processes in 1971 [76], both fiber and bulk lasers utilizing rare earth ions have been developed. An intriguing alternative to traditional pumping energy schemes is lasers based on the PA mechanism [77]. The PA pumping scheme was first explored in 1990 [78], demonstrating efficiency in transforming input photons into laser output. Further observations of PA lasing occurred in different materials, including $LiYF_4$ and BaY_2F_8 crystals co-doped with various rare earth ions. PA lasers have also been reported in bulk materials and inspired the development of fiber-based PA lasing materials [76].

In 1997, Xie and Gosnell reported on Yb^{3+} and Pr^{3+} co-doped ZBLAN fibers [79], resulting in multicolor emission lines. Similar systems were studied by other researchers, generating laser beams at different wavelengths. PA lasers encompass a wide range of visible radiation, offering possibilities for red, green, and blue emissions [48].

Most PA laser systems, particularly those with high efficiencies, are based on Pr or Pr-Yb co-doped materials. It's important to note that many reports on this topic were published in the 1990s and early 2000s, lacking the benefits of current knowledge and technologies developed in the last decade, including those in nanotechnology [80][81].

PA-based lasers retain the fundamental advantages of traditional upconverting lasers but introduce novel opportunities. They broaden the range of pumping wavelength combinations and exhibit emission within the visible range. Unlike conventional upconversion mechanisms, PA schemes benefit from higher dopant concentrations, leading to larger absorption cross-sections and increased intensity.

The PA phenomenon at the nanoscale level opens up fresh possibilities in nanotechnology, nanophotonics, optical computing, and telecommunication. PA lasers offer exceptional efficiency in terms of input-output performance, although they require higher pumping power densities for optimal operation. The nonlinear correlation between pumping power and output efficiency makes PA lasers promising for various applications in advanced technologies [77]. Unfortunately, despite initial interest, there are no commercially available PA lasers due to limitations such as low efficiency and high laser threshold [82].

Medium IR photons counter

Mid-infrared (MIR) electromagnetic radiation is in the wavelength range from 3 μm to 20 μm. The detection of MIR photons is crucial in various applications, including spectroscopy, molecular gas analysis metrology, (bio)imaging, and astronomy [83][84][85][86]. However, the current availability of detectors in this wavelength range poses challenges in achieving sensitive and cost-effective MIR radiation detection. Additionally, the detection process is hindered by the presence of high noise signals resulting from natural emission at infrared frequencies above absolute zero. Consequently, there is a pressing need to develop innovative MIR photon counters that can overcome the limitations associated with the low energy of the analyzed radiation and the resulting high thermal background [87].

One of the suggested approaches for detecting MIR signals involves their conversion into visible radiation, where detectors are more sensitive, cost-effective, and readily available. An example of such a process is upconversion, which, in the most well-known case, shifts NIR photons to higher energy in the visible range, enabling their detection using widely available [87] detectors. In 1959, Bloembergen introduced the concept [88] of an Infrared Quantum Counter (IRQC), whose operation is based on a two-step excitation process In the Bloembergen IRQC operation scheme, the first step involves infrared radiation exciting atoms to a metastable level, followed by the next step in which intense pumping

excites the atoms to a higher emission level. As a result, the IR signal is incoherently converted into emission in the spectral range where detectors are commonly available, highly sensitive, and more affordable.

In 1979, Chivian et al. first reported the development of PA medium infrared quantum counter detectors (MIRQC). During their exploration of materials for IR quantum counters, they uncovered the PA phenomenon in hosts $LaCl_3$ and $LaBr_3$ doped [1] with Pr^{3+}. The fundamental concept was straightforward - materials were pre-pumped with a wavelength matching ESA instead of GSA excitation. Upon surpassing a certain pump power density threshold a remarkable 100-fold increase in red luminescence intensity at 600-640 nm was observed. When the system approached the PA threshold, 4.5 μm photons (matching the ground $_3H^4$ to $_3H^5$ level of Pr^{3+} ions) were adequate to initiate avalanche emission. Granted, a fourfold increase in the sensitivity of MIR photon detection was demonstrated. The analysis of the results relied on the sequence of ion interactions, wherein the absorption of a single infrared photon triggered the generation of multiple excitations.

Luminescence thermometry

Luminescence thermometry is a technique that relies on measuring temperature through non-contact luminescence analysis [89][90]. The phosphor comes into contact with the object under investigation, then is illuminated by an excitation beam, and the resulting temperature-dependent emission is recorded by a detection system [91]. It has found applications in various fields, including materials science, biology, and industry. One fascinating aspect of luminescence thermometry is its ability to measure temperature with high precision and accuracy. Among the different luminescence phenomena used for thermometry, one of the most intriguing is PA emission amplification.

Luminescence is the emission of light observed when a material absorbs energy and then re-emits it as photons. Luminescent materials, known as phosphors, exhibit temperature-dependent luminescent properties. These properties make them good candidates for temperature sensing. The basic principle of luminescence thermometry involves exploiting the temperature sensitivity of the luminescent signal. When a phosphor is excited by an external energy source, such as light, it emits photons. The intensity and spectral characteristics of this emitted light depend on the temperature of the phosphor. By measuring these luminescent properties, the temperature of the material can be

determined accurately. Temperature affects the density of phonons, which are quantized vibrations of the crystal lattice. Phonons result from temperature-related vibrations of the crystal lattice, and their intensity is related to thermal energy and phonon energy (oscillation frequency) is related to a particular vibration mode. Phonons are involved in phonon-assisted transitions, which occur via phonons when there is an energy mismatch and in PA these transitions involving phonons take place. In addition, when two energy levels are close to each other, there is established a thermodynamic equilibrium between them defined by the Boltzmann statistical distribution. As the temperature increases, there is a broadening of the spectral lines. This means that there can be more energy incompatibility during absorption and the emission becomes spectrally broader.

The intensity of PA strongly depends on the excitation power, or more precisely, on the effective power absorbed by the system. This power absorption is greater the larger the absorption cross-section (which is related to the width of absorption lines) and the better the match between the excitation beam wavelength and the line. Therefore, as the lines broaden, the system will absorb more light, especially when the initial spectral matching was weak.

Moreover, many of these processes involving phonon assistance are part of an "energy loop," meaning they must occur multiple times within such a cycle. As a result, their significance is multiplied, and slight changes can disturb the balance of this process, leading to a change in its characteristics—shifting power dependence, altering slope or modifying the growth dynamics. Alternatively, it can simply affect the emission intensity.

Optical synapse

Various methods of optical data processing, such as logic gates, are currently under development, and they have been successfully demonstrated utilizing the unique properties of avalanche. Using nanomaterials NaYF4: 8% Tm^{3+}, a series of effects similar to those exhibited by elements of nervous systems in living organisms has been demonstrated. For example, paired-pulse facilitation (PPF), where the response amplifies depending on previous stimulation, and a logical AND gate, which combines signals to surpass the PA threshold only through their combined power acting on the material.

The metastable level in lanthanide ions, characterized by a long decay time, is crucial for enabling PA. The extended lifetimes facilitate population increse through CR. Rapid decay of the metastable level's population would hinder PA, as insufficient time would be available to accumulate a significant population for efficient laser absorption through ESA from this level. Utilizing the long lifetime of the metastable level, kinetics measurements were carried out.

PA measurements [92] enable the processing of complex signals entirely optically. The way the avalanche material emitted light allowed for classifying two-dimensional images or measuring the coincidence of light pulses. The luminescence stimulated by pulses of the material depends on the time intervals between successive, identical excitation pulses. In one experiment, an optical scan of Arabic numerals was conducted, where the pixel brightness correlated with the intensity of excitation in avalanche synapses. The material's unique response to displaying each numeral allowed for the unequivocal optical identification of individual digits, eliminating the need for intricate neural networks.

Moreover, leveraging the distinctive characteristics of the material, computational processes akin to those occurring in the Nucleus Laminaris region of an owl's brain were successfully emulated. This brain region is responsible for gauging the phase difference of sound waves reaching each ear, enabling the creature to discern the sound's origin.

The described properties resemble the functioning of synapses, and these analogies can be utilized for optical amplification, fully optical signal processing, and information storage.

The work is ongoing regarding the utilization of PA for biodetection, pressure/force measurement, photodarkening, which involves recording information.

5. Experimental part

Experimental methods encompass not only the description of the measurement methodology but constitute a substantial part of tasks within this doctoral research. This is because, to investigate materials exhibiting PA, it was necessary to construct a dedicated setup that would allow the measurement of the laser power-dependent luminescence intensity, rise and decay times, as well as emission spectra.

All measurements of luminescence intensity as a function of the power density of the excitation light, as well as measurements of rise times, were made on an optical microscope specially designed and built for this purpose.

5.1. Experimental setup

The body of the microscope which was the basis of the developed measuring system is a Nikon Ti-U Eclipse inverted fluorescence microscope, shown schematically in the *Figure 12*. It is possible to measure a very wide range of excitation laser power densities, which range from 10^2 to 10^7 W/cm^2. With the appropriate positioning of the mirrors, it is possible to select choose one of three diode lasers (single mode diodes) to excite the sample. The diodes are equipped with a single-mode fiber that maintains polarization, and collimator. To precisely and automatically control the output power of the generated beam, we employed a motorized system consisting of neutral density filters (NDFs). The first filter, NDF1, is a gradient neutral density filter (NDC-100C4M, Thorlabs), which allowed for gradual adjustment of the output power. Meanwhile, a set of additional neutral density filters (NDF2), including NDUV06, NDUV10, NDUV15, and NENIR30 (Thorlabs), used to make coarse selections within the available range of light powers. This setting, where the laser beam is set to the maximum power that passes through a gradient gray filter and then through a set of gray filters, provides precise and smooth control of the light power density, without affecting the spectral shifts in the diode laser spectrum that would arise if the laser power was adjusted by electric current.

After passing through this module, the beam is directed towards the beam splitter, which reflects a portion of the radiation to the optical power meter sensor (S121C+PM100, Thorlabs). The reference power value is continuously monitored, enabling us to calculate the power density of the light illuminating the sample. Approximately 90% of the light is transmitted through the beam splitter, and it is reflected by a dichroic mirror, appropriately matched to the wavelength of the laser, which reflects the beam, thereby

introducing it into the body of the microscope (Nikon Ti-2 Eclipse) to the left port. Afterwards, the laser beam passing through the objective is focused on the sample, which is placed on a coverslip. Photons of light emitted from the sample have higher energies (shorter wavelengths) than photons of excitation light. Emitted light is collected through the objective lens and then exits through the same left port from the microscope. The beam then passes through a pair of filter wheels. One of these wheels is equipped with spectral band-pass filters, while the other contains neutral density filters (NDF3) designed to control the intensity of the signals, preventing them from exceeding the dynamic range of the detectors.

The emitted light then passes through a dichroic mirror and can be recorded in two ways. When the mirror in the emission arm is raised the intensity of the luminescence light is recorded by two photomultiplier modules, so dual channel (PMT1001M and PMT2101M from Thorlabs), which are connected to a photon counter (quTAG). The PMTs are placed in a box, in which PMTs cooling is done with Peltiers modules to reduce temperature of active photo-sensitive elements and thus reduce the inherent noise of the detectors. The box is closed and is purged with nitrogen, so that the water vapor in the air does not condense on the devices. The light entering the PMTs is separated by a dichroic mirror, and then only the narrow wavelength range that is recorded is selected using band pass filers. With this setup, the dependence of the luminescence intensity as a function of the power density of the excitation laser is measured. When the mirror in the emission arm is lowered, the luminescence spectra from the sample are recorded using an Andor Shamrock i500 spectrogram with a Newton CCD camera (DU920P-BEX2-DD).

Depending on which lanthanide ions were studied, appropriate emission filters were selected before entering the PMTs tube and dichroic mirrors.

When temperature measurements were taking place, a THMS 600 heating stage holder (Linkam) was positioned on the microscope body. In this confluence, the laser beam was focused through a long-distance objective (f = 20 mm) (M Plan Apo 20x) on a sample placed on a microscope slide, which was inside the rotated heating stage THMS.

I actively participated in the construction of this measurement system under the leadership of dr. Marcin Szalkowski, and was engaged in various tasks such as setting up components, introducing lasers and optical fibers into the system, calibration, and fine-tuning. My responsibilities also extended to the incorporation of optics, including filters,

to achieve optimal measurement parameters. Additionally, I designed a holder for measuring crystals in various orientations on the microscope using AutoCAD, and then I 3D-printed it (*Figure 14*).

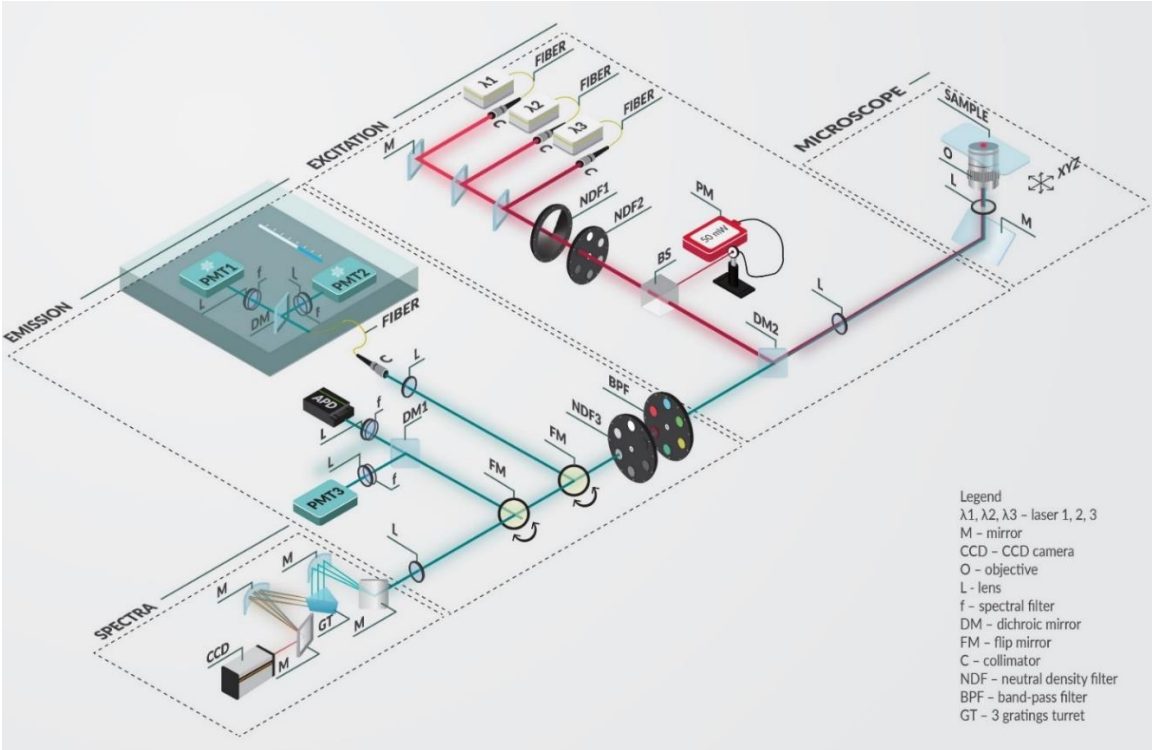

Figure 13. The scheme of microscope setup.

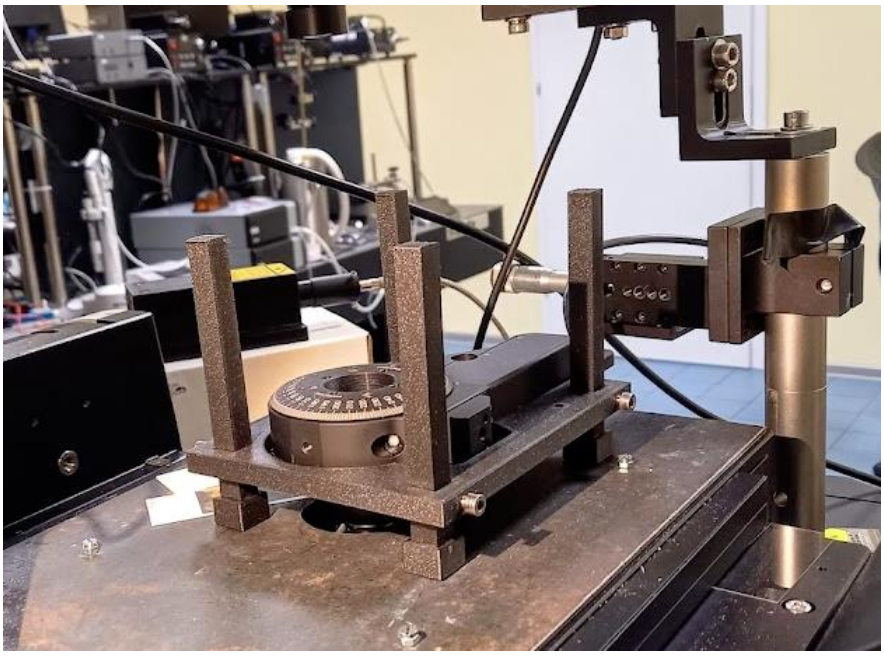

Figure 14. 3D-printed holder for measurements with varying samples orientation.

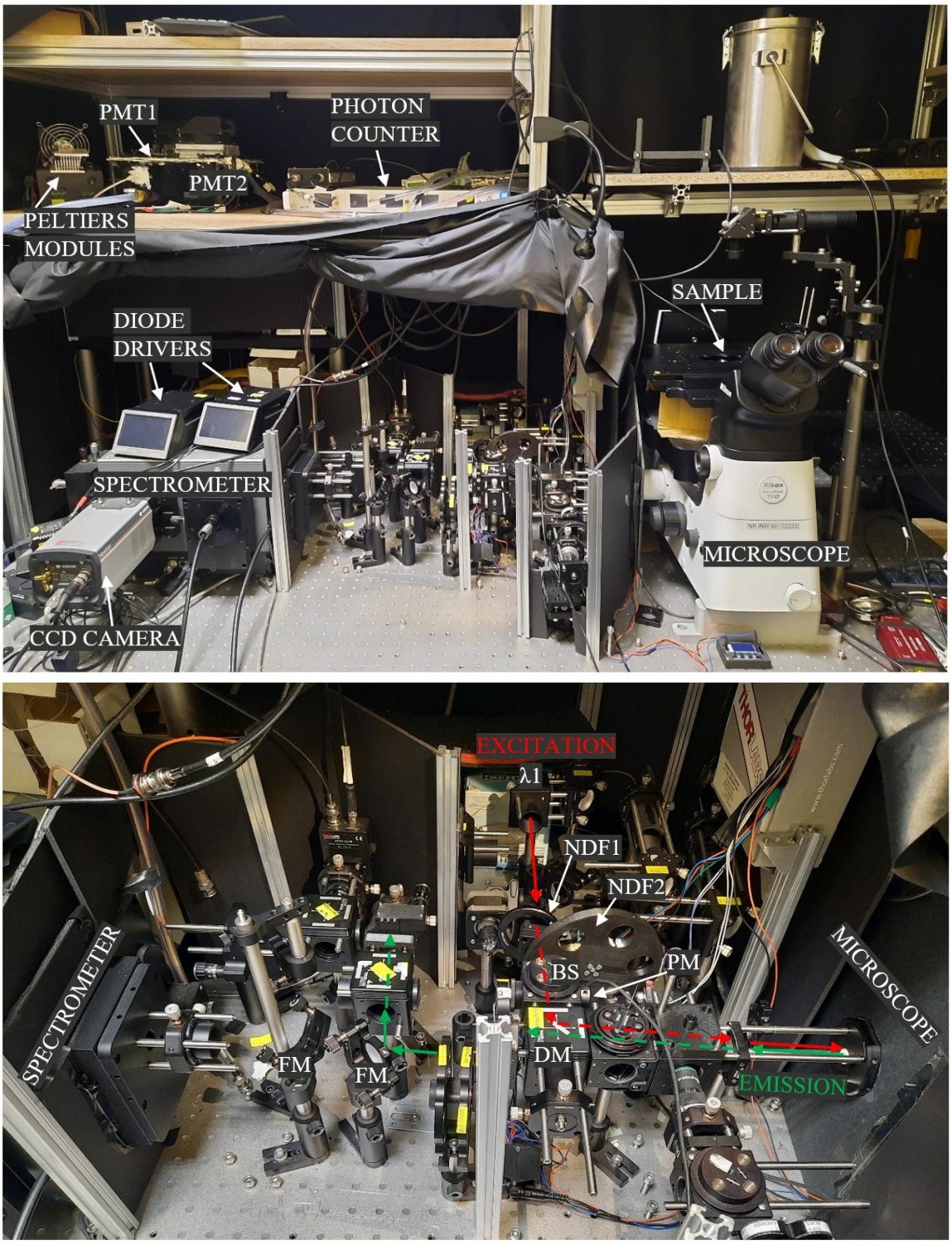

Figure 15. Photos of the microscopic system. Flip mirror (FM), neutral density filter 1 (NDF1), neutral density filter 2 (NDF)2, power meter (PM), beam splitter (BS) dichroic mirror (DM), laser 1 (λ1).

5.2. Experiment procedure

Measurements of avalanche photon emission were conducted as follows. When the measurement involved nanocrystals, they were in colloidal form in chloroform. Using a pipette, I dropped them onto a microscope slide and waited for the sample to dry. In the case of loose microcrystals, I used a spatula to sprinkle them onto the slide and then added ethyl alcohol to help them adhere to the slide. Then, using the eyepiece of the microscope, I looked for a clear image of the sample. For nanocrystals, I focused on the sharp edges of the dried colloid, while for microcrystals, I searched for a single crystal that was not in contact with others and positioned it in the center of the laser beam.

Next, using the detector, I sought the maximum signal from the sample, ensuring that the sample was precisely in the focal point of the objective. Once found, I proceeded to the measurements. PA and kinetics measurements were carried out using a program written in LabVIEW. The program controlled the diode laser, manipulated the gray filters, which smoothly changed during measurements, and saved the counted measurement points. Manually, I had to attenuate the emission filters when the signal approached the detector's saturation.

During PA measurements, the laser was set to maximum power, and its power on the sample was attenuated through gray filters. The gradient gray filter's speed could be controlled using a stepper motor. The NENIR gray filters in the filter wheel could be set manually or transition to the weakest during measurements. During the measurement of PA, for various laser powers, the rise and decay times could be measured. A time window was set for the measurement duration, and the laser started operating in pulsed mode. After this, the avalanche measurement continued for higher powers of the exciting laser. When the laser power reached its maximum, the measurement was terminated. It was essential to carefully observe the signal counts on the photon counter because, in the case of high emission intensities, appropriate gray filters had to be set. These filters were then introduced into the program, and the program automatically recalculated the emission intensity. Measurements could be performed in a dual-channel mode, meaning for two emissions simultaneously. In such a case, I inserted the appropriate dichroic mirror and band-pass filters corresponding to the emissions from the sample into the cooling

chamber, where the PMT detectors were located. In Table 2, there is a list of filters that I used during the measurements.

In the case of emission spectra measurements, I removed the mirror that directed the emission light to the detectors, allowing the light to be introduced into the spectrophotometer. Spectra measurements could also be conducted for various powers of the excitation laser.

When changing the laser for PA measurements, it was necessary to set the laser power parameters at which the gray filters in the LabVIEW program would automatically attenuate. For this purpose, I placed a power meter on the objective, recorded the power meter values while rotating the gradient filter, and then input these values into the program to ensure a smooth transition between filters during measurements. When the laser power reached a specific value, the filter would change accordingly.

During pump-probe measurements, for time-resolved experiments involving the dynamics of emission intensity rise with temporal synchronization, an additional arbitrary waveform generator (DDS JDS6600) controlled the modulation of the laser diode and the photon counting module.

In the experimental illustration of the paired pulse facilitation (*Figure 34*), a series of two impulses with varying temporal intervals was achieved by initiating the laser diode through the DDS arbitrary waveform generator. This generator generated a sequence of two electrical gating pulses via its first output channel (Ch1), each with corresponding temporal relationships. Simultaneously, the second output channel (Ch2) facilitated the synchronization of the pulse generation and the detecting module. An experiment illustrating the impact of the time gap between excitation pulses on rise kinetics (*Figure 32*) was conducted as follows. A signal characterized by temporal relations was generated using the DDS generator (Ch1). The second channel (2Ch) was employed to synchronize this procedure with the detecting module. This included fine-tuning the temporal gap between the two gating pulses generated by the arbitrary waveform generator. The demonstration of the impact of the residual pump ratio on the rise kinetics (*Figure 32*) encompassed the generation of a sequence of two excitation pulses. As previously mentioned, an adjustable pump offset intensity was applied between these pulses. Lastly, the illustration of phase-matching optical detection (*Figure 36*) was accomplished by defining, through the arbitrary waveform generator, a three-level excitation sequence

corresponding to the alignment of two digital signals with varying phase shifts. These shifts included an off state with low logic levels on both inputs, half power operation with power density below the PA threshold (corresponding to low logic level on one input and high logic level on the other), and full power operation with twice the power density of half power mode (corresponding to high logic levels on both inputs). This sequence was produced on the Ch1, with synchronization with the detecting module on Ch2.

Table 2. Filters and dichroic filter for excitation and emission for various lanthanide ions.

Lanthanide ions	Dichroic mirror before microscope	Filter before PMTs	Filter before PMTs	Dichroic mirror before PMTs
Tm^{3+}	DMSP900R	FF02809/81-25	440BP20	FF756-SDi
Pr^{3+}	DMSP805	600BP40	F01-475/35-1	DMSP505R
Ho^{3+}	DMSP1000	545BP45	FB650-40	DMSP600R

Table 3. Lasers used in the experiment. All the lasers were coupled to single mode fiber.

Butterfly lasers	Wavelength [nm]	Max pump power [mW]	Fabry Perot grating
1064CHP	1059	170	no
BL976-SAG300	976	300	no
FPL852S	852	350	yes

5.3.Characteristics of the 1059 nm and 976 nm lasers diode

In the course of optimization, we realized the stability of laser diode wavelength and power is of critical importance for reliability of data acquisition and interpretation. For this reason, to avoid temperature tuning of the laser wavelength, the diode laser was set to maximum power, so that the laser would emit at exactly the same wavelength. On *Figure 16* are shown measurements of the laser spectrum for different junction temperature (TEC) and for different current. It can be noticed that the spectra shift by a few nanometers, which in the case of lanthanides, which have narrow absorption and

emission lines, can be crucial for the ESA absorption of laser light to occur. This can be especially problematic, as it is not trivial to measure ESA spectra. Because PA is highly susceptible to beta and exhibit very high non-linear dependence, it is of utmost importance to keep the laser source at fixed wavelength.

For a TEC temperature of 10°C, the wavelength of the laser was 1052 nm; for higher temperatures, the spectrum shifted toward longer wavelengths, until by 40°C it was 1063.5 nm. For a current of 200 mA the wavelength of the laser was around 1055 nm, for higher current the spectrum shifted towards longer wavelengths, until for a current of 900 mA it was almost 1059 nm (*Figure 16.*)

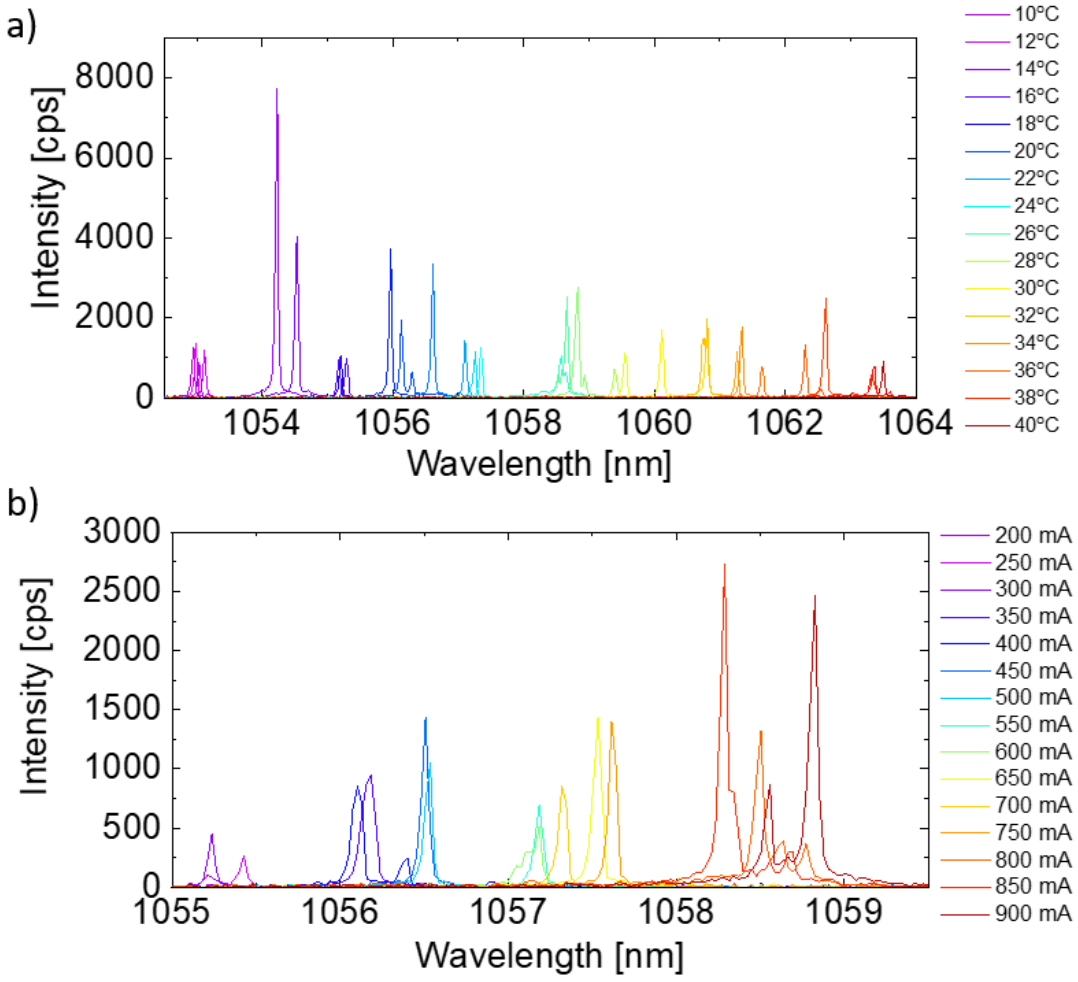

Figure 16. Spectrum of laser beam 1059 nm for a) different TEC junction temperature b) for different current.

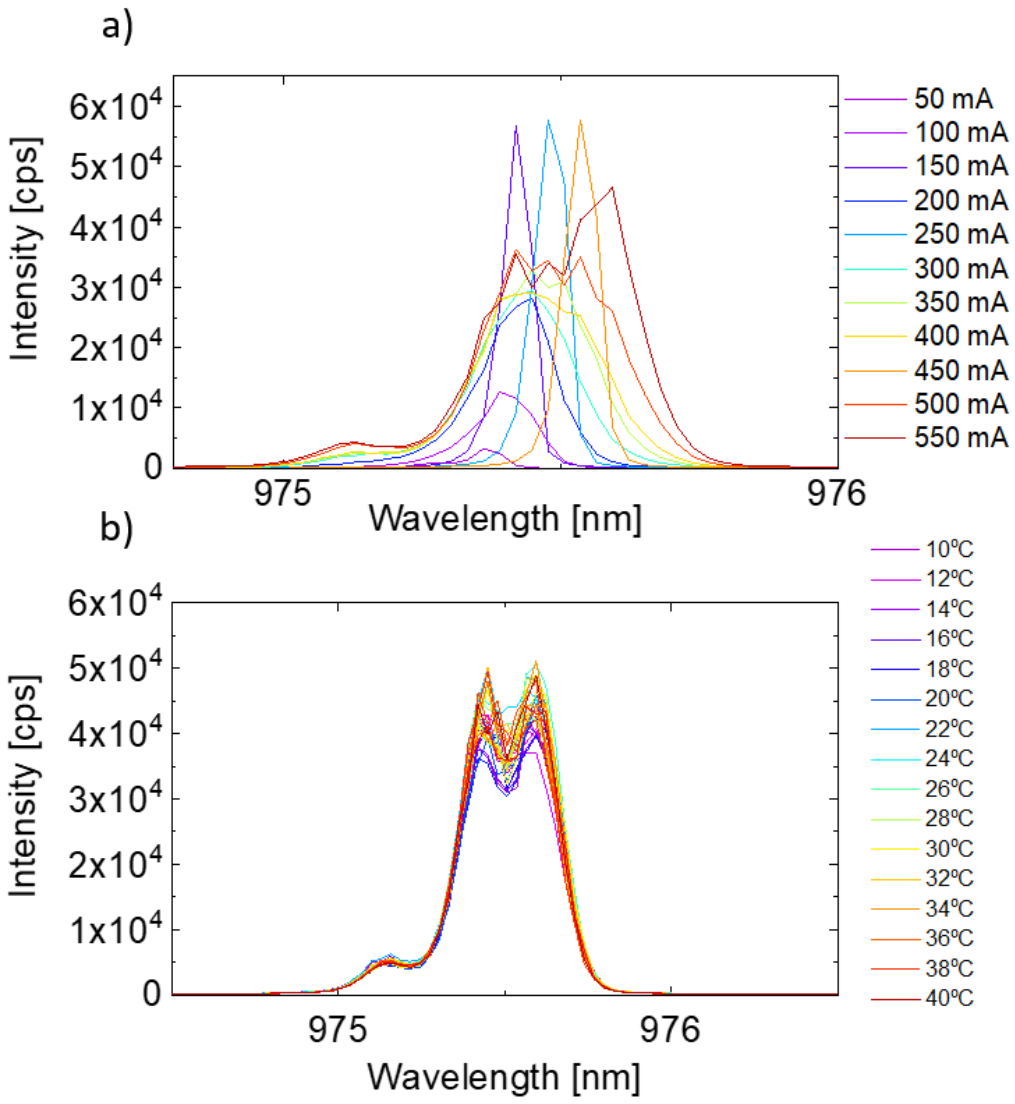

Figure 17. Spectrum of laser beam 976 nm for a) different current b) different TEC junction temperature.

Laser diode 976 nm (*Figure 17.*) was equipped with a Fabry-Perot resonance grating to control and achieve wavelength stability, so that a change in the junction temperature does not affect the change in the laser wavelength.

5.4. Algorithm for data analysis

In order to speed up, facilitate and make the analysis of data from PA measurements (i.e. emission rise/decay curves) operator independent, an algorithm was written in Matlab. In the program, parameters describing PA properties such as the slope of the s-shape curve, threshold (I_{th}), and parameters describing lifetime are calculated. The code is accessible through our web repository (https://github.com/LuNASIanalysis/Photon-Avalanche-PA-). Our algorithm relied on fitting a linear function to the logarithm of the raw data, analogous to fitting the exponential function to raw data, point by point.

In this process, for each point, the fit encompassed the maximum range of the surrounding data, meeting the specified certainty criterion. This approach effectively mitigated the impact of noise as well as operator specific, manually selected range of data fitting on the determined S values. The highest S values were obtained in a similar and comparable manner.

Additionally, the thresholds values were defined as the power corresponding to the point of the cross-section of lines tangent to the logarithm of the raw data in the area before the avalanche region and the tangent to the logarithm of the raw data concerning the maxima of S.

I want to note that I contributed to a portion of this Matlab program and prepared a simplified version for sharing on GitHub.

6. Results and discussion

6.1. Photon avalanche in Tm^{3+}

PA in Tm^{3+} ions is a complex phenomenon governed by several parameters, each playing an important role in shaping the characteristics of the emitted photons. Understanding and manipulating these factors are essential for unraveling the intricacies of this process.

One such factor is the concentration of ions within the material significantly impacts the PA. The density of Tm^{3+} ions in the crystal lattice has a direct correlation with the efficiency of PA emission.

In addition, the size of the crystal plays a pivotal role. Different sample volumes translate into differences in parameters describing PA.

The thickness of the shell surrounding the Tm^{3+} ions is another critical parameter. The passive shell protects against surface quenching and contributes to improving PA.

Furthermore, the selection of the matrix in which Tm ions are embedded plays a crucial role in shaping the overall behavior of PA. The vibrations of the crystal lattice, known as phonons, within the matrix can impact PA, even when the concentration of Tm ions remains constant.

The presence of another ion, such as Tb^{3+} or gold nanorodes further adds a layer of complexity to the PA process in Tm^{3+} ions.

In this chapter, we will explore the influence of these parameters on avalanche photon emission (PA) in Tm ions. This underscores that PA in Tm ions is a multifaceted and intricate phenomenon. A thorough comprehension of these factors is essential for effectively utilizing and optimizing PA in diverse applications.

6.1.1. Investigation of particle size on PA in Tm^{3+}

In the pursuit of understanding the influence of host material size and nanoparticle passivation on the PA phenomenon, a systematic synthesis of various $LiYF_4$ [75] materials was carried out. These materials encompassed bulk crystals, microcrystals, core nanocrystals, and core–shell nanocrystals, all doped with Tm^{3+} at concentrations of either 3% or 8%. This methodology facilitates comparative analyses across different crystal

forms, while maintaining a consistent 3% Tm^{3+} composition. The choice to focus on $LiYF_4$ microcrystals, core nanocrystals, and core–shell nanocrystals doped with 8% Tm^{3+} was following previous studies which established optimal concentration for inducing the PA phenomenon within a similar $NaYF_4$ matrix [44].

Nanocrystals (NCs), in both core and core-shell architectures, were synthesized by thermal decomposition of lanthanide salts by dr. Małgorzata Misiak. The microcrystals were prepared by a hydrothermal method.

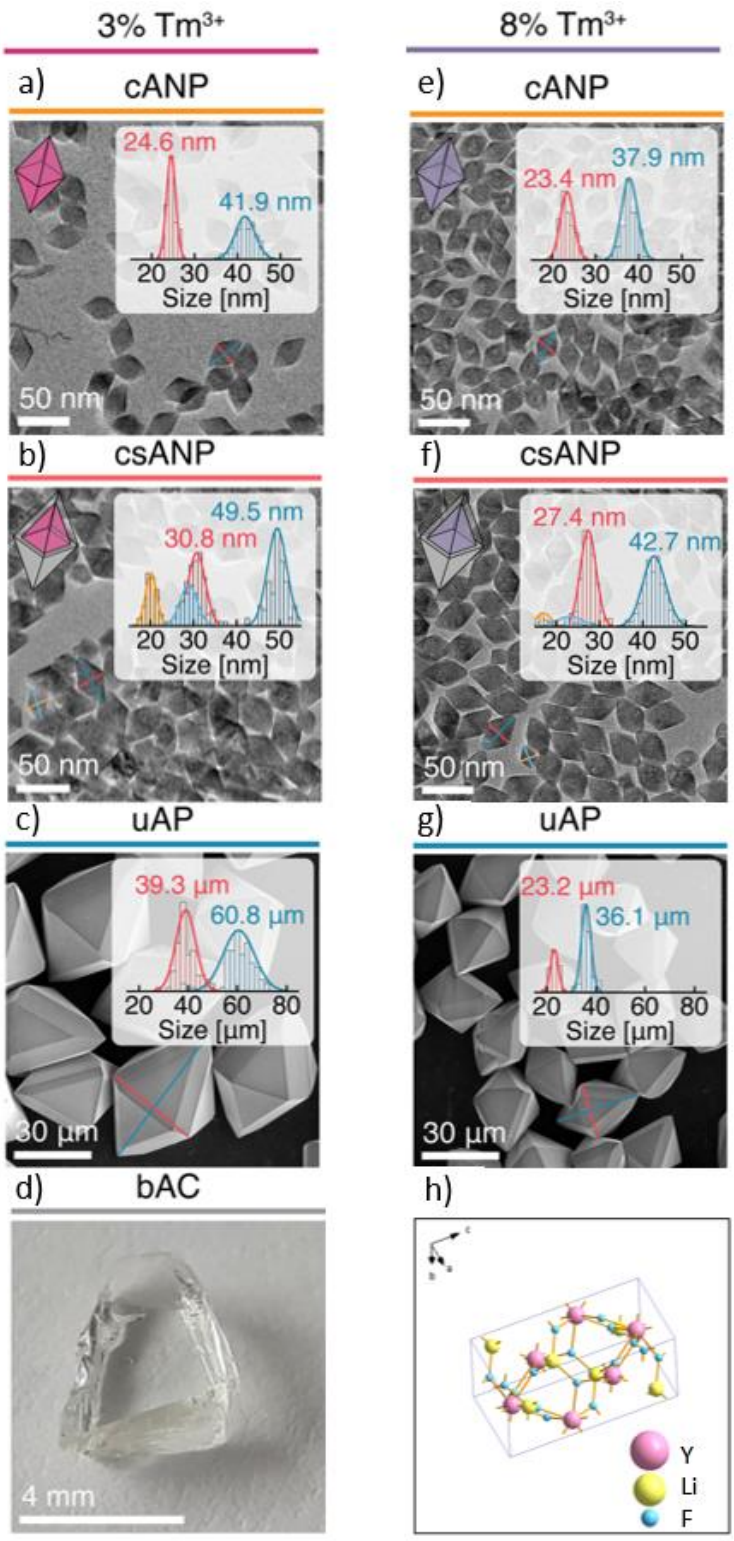

Figure 18. Morphology and size comparison of the crystals under investigation : a), e) core avalanching nanoparticles b), f) core-shell avalanching nanoparticles c),g) micro avalanching nanoparticles d) bulk avalanching $LiYF_4$ crystals with 3% or 8% Tm^{3+} doping [75].

To ensure the quality and integrity of the crystal samples, X-ray diffraction and electron microscopy analyses were conducted and are illustrated in *Figure 19*. Based on the average dimensions of the nanocrystals, the shell thickness was determined to be 3.1 nm in width and 3.8 nm in length for csANPs doped with 3% Tm^{3+} and 2 nm in width and 2.4 nm in length for csANPs doped with 8% Tm^{3+}.

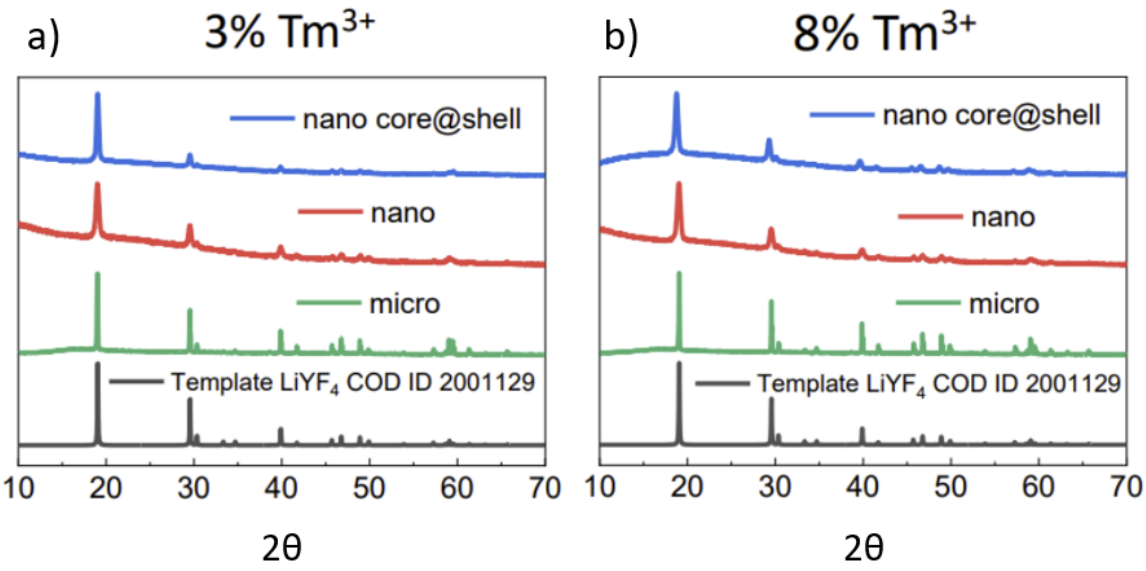

Figure 19. XRD diffraction patterns of the investigated $LiYF_4$ materials nanocore, nanocore-shell, and microparticles doped with a) 3% b) and 8% Tm^{3+} are presented.

A comprehensive examination of the optical properties of these materials was also carried out using a consistent optical setup and methodology. In these experiments, nanoparticles were deposited as thick films on glass slides, and signal averaging was based on 10 measurements taken at distinct locations on each slide. Additionally, for micron-sized avalanching particles (μAP), individual microparticles were analyzed, with meticulous sample positioning optimization relative to the excitation beam to maximize luminescence signal intensity.

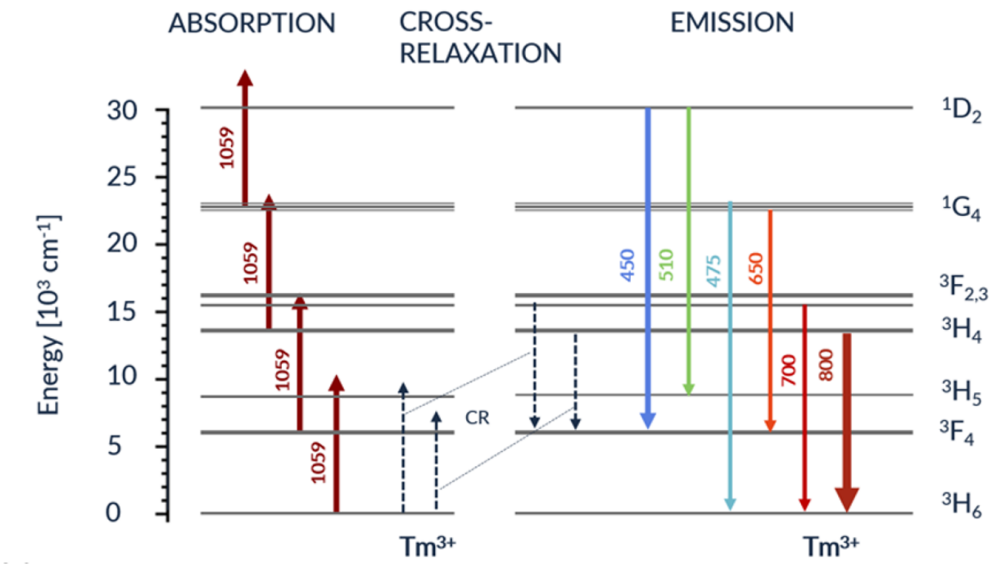

Figure 20. Energy scheme of Tm^{3+} with transition.

Notably, our findings revealed the versatile capability of Tm^{3+} ions to generate photoluminescent avalanching (PA) emissions at two distinct wavelengths: 800 nm originating from the $^3H_4$ level, as previously documented, and 475 nm originating from the $^1G_4$ level (*Figure 20*). It is worth noting that both emissions displayed a markedly nonlinear relationship between intensity and risetime, characteristic for the PA effect. The avalanche-like behavior of the 475 nm blue emission can be attributed to the accumulation of population on the $^1G_4$ level, resulting from energy looping and PA processes between the $^3H_6$, $^3H_5$, and $^3H_4$ levels, assisted by the ESA mechanism where $^3H_4$ is excited by a photon to transition to $^1G_4$. It's important to highlight that the 475 nm PA emission was approximately 100 times weaker in intensity compared to the 800 nm emission.

The discovery of the 475 nm PA avalanche emission for core-shell nanocrystals opens up opportunities for designing a wider range of PA colors by introducing other lanthanide co-dopants that can be excited by these high-energy photons.

Measurements of luminescence intensity power dependence at room temperature were conducted for various sample types. The excitation power density ranged from 1 kW cm^{-2} to 14 MW cm^{-2}. To ensure a reliable statistical representation, the experimental routine was repeated 10 times, each for a distinct sample region. Subsequent measurements for a particular sample exhibited only minimal variations.

For each sample, notable alterations in power dependencies can be attributed to three distinct regimes: (1) the pre-avalanche region, below the PA threshold, with slopes

approximately 2, (2) the avalanche region, above the threshold, with slopes exceeding 6-12, and (3) the saturation region of higher power densities with slopes approaching 1.

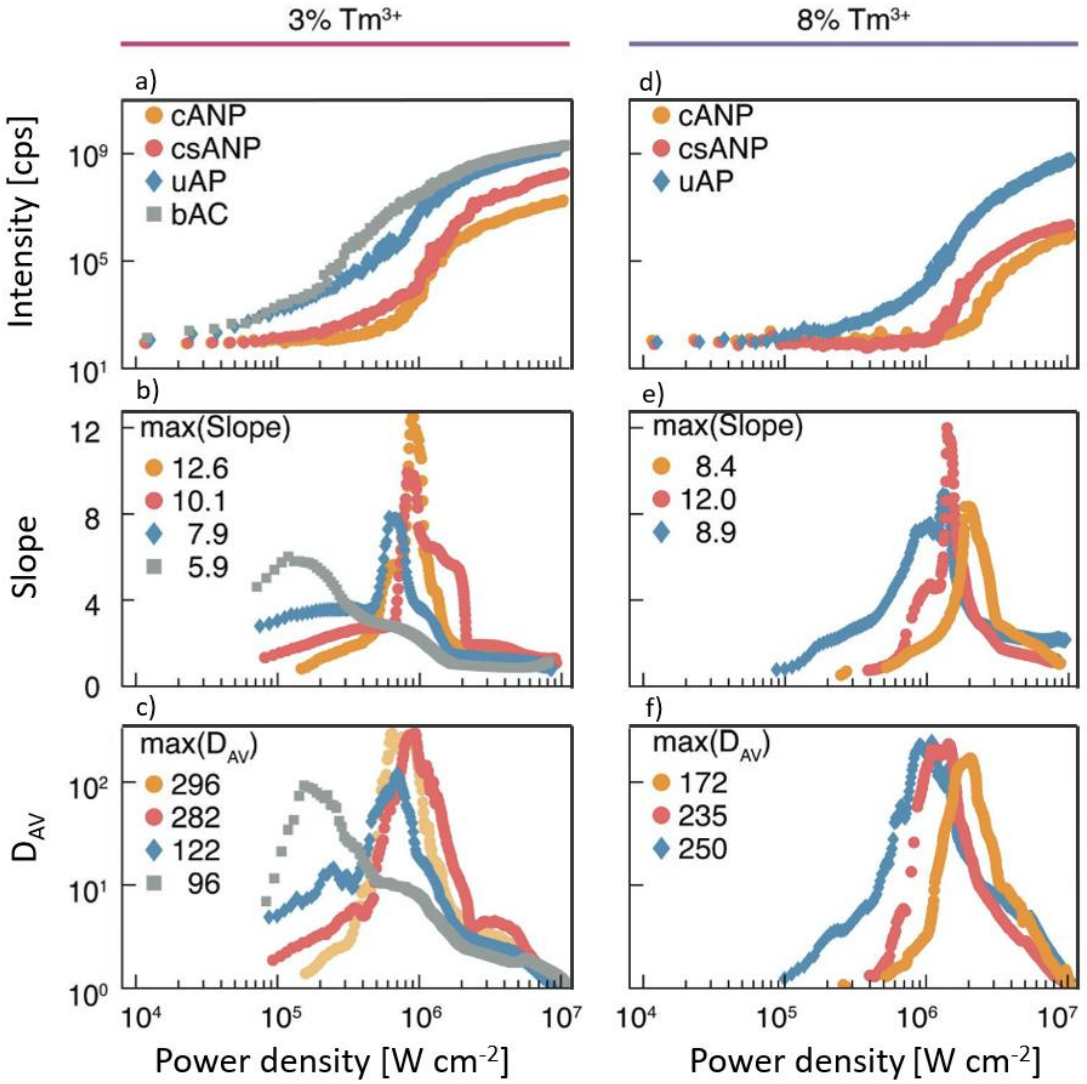

Figure 21. Examining 800 nm ($^3H_4 \rightarrow {}^3H_6$) PA behavior across nano, micro, and bulk crystals, we conduct a comparison of pump power-dependent PA emission intensity - row 1, PA slopes - row 2, and PA gains - row 3 at 800 nm for the following materials doped with a), b), c) 3% and d), e), f) 8% Tm^{3+} [75].

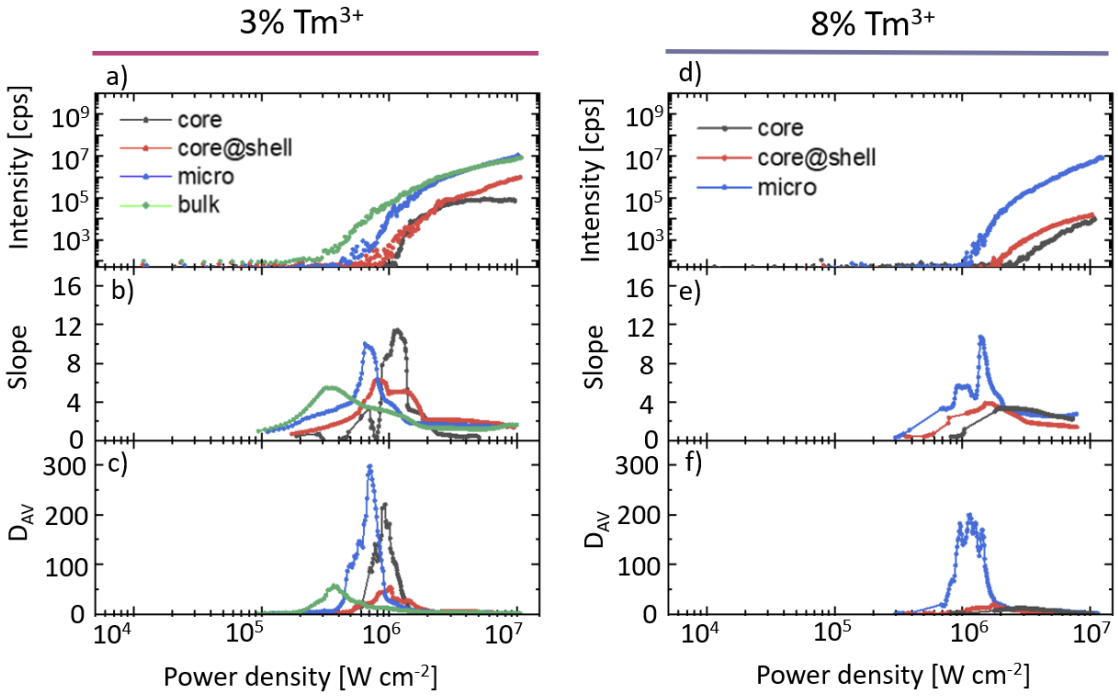

Figure 22. Comparative analysis of power-dependent 475 nm ($^1G_4 \rightarrow {}^3H_6$) PA emission intensity, along with corresponding PA slopes. In this study, we explore the behavior of bulk - green, micron-sized - blue, core nanoparticles – gray and core-shell nanoparticles - red in two sets of samples, doped with 3% - left column) and 8% - right column of Tm^{3+}. We focus on the emission at 475 nm under the PA regime with excitation at 1059 nm. The software used for analysis automatically calculated the slopes, gains [75].

A distinct size-dependent pattern emerges when analyzing luminescence intensity, slopes, and photoluminescent avalanching (PA) thresholds in the 8% Tm^{3+}-doped core avalanche nanoparticles (cANP), core–shell avalanche nanoparticles (csANP), and micron-sized avalanche particle (μAP) samples. For the 3% Tm^{3+} doped samples, size-dependent relationships are also evident, although the interpretation of both qualitative and quantitative results is less straightforward compared to the 8% Tm^{3+} samples.

As the volume of PA material decreases from bulk to microcrystals and nanocrystals, the PA threshold exhibits a progressive increase by nearly one order of magnitude: starting at ≈ 200 kW cm^{-2} (for bulk), it reaches 300–400 kW cm^{-2} (for μAP), and 700–800 kW cm^{-2} (for cANP and csANP). Additionally, notable differences are observed in relation to the role of the passive shell surrounding the Tm^{3+}-doped ANP core nanoparticles, depending on the analyzed nanocrystal architectures.

The addition of a passivating shell to the 3% Tm^{3+}-doped nanoparticles neither alters the threshold pump power nor significantly enhances PA performance (as measured by S values and D_{AV}). However, it does result in approximately a tenfold improvement in brightness. In the case of the 8% Tm^{3+}-doped sample, the passive shell around cANP yields different effects, notably lowering the PA threshold and enhancing the nonlinearity. These effects in the 8% ANPs align with expectations and can be attributed to the protective role of the shell in reducing surface quenching. Interestingly, smaller materials exhibit higher nonlinearities and larger PA thresholds, potentially attributable to increased surface/ligand phonon-assisted quenching and ground-state absorption (GSA).

In the case of the 8% doped cANP, csANP, and μAP, PA gains are in line with those of the 3% samples, reaching values of up to 200. Simultaneously, the threshold for pump power, at which the PA nonlinearity becomes pronounced, is lowest for bulk materials. These effects can be attributed, at least in part, to the geometric relationship between the size of the material and the focal spot of the laser beam.

Conclusions

In summary, grasping the link between PA emission and material volume holds significant implications for various nano-bio-photonics applications. Consequently, this study compares nanomaterials (both core and core-passive shell), micro-scale materials, and bulk $LiYF_4$ crystals, all doped with 3% Tm^{3+}. Additionally, we synthesized corresponding core-only and core–shell nanomaterials, along with microcrystals doped with 8% Tm^{3+}, allowing us to quantitatively analyze their pump power dependent PA slopes, thresholds and gains.

The luminescence of all the materials under investigation at 800 and 475 nm exhibits the characteristic features of PA emission, including a discernible pump power threshold, a pronounced 6–12 nonlinearity in PA emission. The largest values of the slope of the luminescence curve as a function of pumping power density were 12 (8% Tm^{3+} core-shell NCs) and 12.6 (3% Tm^{3+} core NCs) .

The volume and scale of the material affect the PA phenomenon significantly, and two phenomena can result from this. As the size of the material increases, the number of ions contained in it also increases. In the context of PA, which is a collective phenomenon, the

effective interaction between multiple ions, which must efficiently accumulate energy in the metastable state, is important.

A larger number of ions opens up a number of possibilities for interaction, and larger material minimizes the contribution of surface quenching. This process involves the transfer of energy to quencher molecules. For smaller materials, especially at the nanoscale, the role of surface effects becomes more significant, thus two architectures were tested, bare core or a core with a protective shell.

The influence of these factors on PA manifests itself in a shift of S-shape characteristics. For smaller materials, where the number of ions is limited, the contribution of surface effects is greater, resulting in a shift in the PA threshold correlated with the host size. Moreover, for larger materials, the luminescence intensity is higher.

In addition, different Tm^{3+} ion concentrations affect the dependence of the luminescence intensity on the power density of the excitation laser. At lower concentrations (3%), the effect is more localized, spreading less in volume, so that the shell in the nanomaterials does not affect it as significantly. At higher concentrations (8%), the higher number of ions means that the effect does not saturate that easily, can exchange energy efficiently with neighboring ions, and the role of the shell becomes more important, protecting the nanocrystal from quenching.

6.1.2. Influence of Tm^{3+} ion concentration on PA

The following study was conducted to see how PA behaves in ions with different Tm^{3+} concentrations. A concentration series (1%, 3%, 8%, 12%, 16% of Tm^{3+}) of $LiYF_4$ microcrystals was synthesized by Małgorzata Misiak. Electron microscope images (*Figure 23*) and X-ray diffraction (*Figure 24*) confirm the structural purity and morphology of the crystals. Diffraction peaks from the crystals overlap with the reference standard spectrum. The size of the microcrystals ranged from 61.8 to 88.9 micrometers, and were all larger than the size of the photoexcitation beam (c.a. 1 um in diameter).

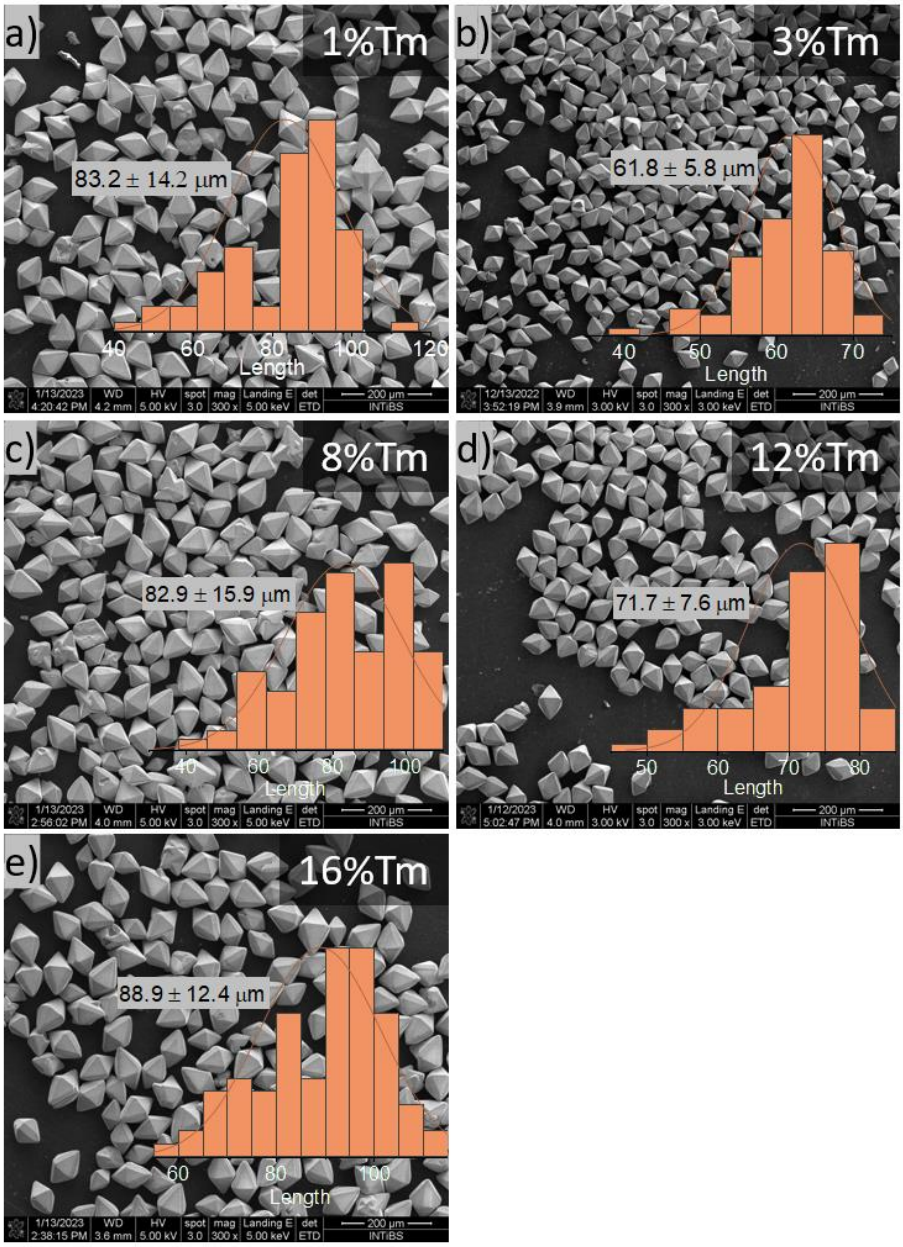

Figure 23. Scanning electron microscope (SEM) images with size distributions of microcrystals $LiYF_4$ doped with for 1%, 3%, 8%, 12%, 16% of Tm^{3+}.

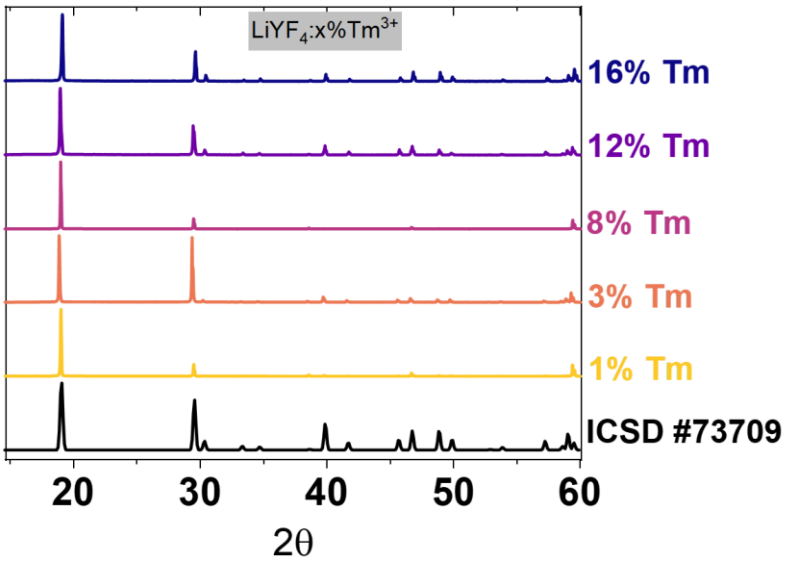

Figure 24. Powder X-ray diffraction data of the synthesized $LiYF_4$ microcrystals doped with 3% Tm^{3+} and varying concentrations of Tb^{3+} ions are presented.

Microcrystals with different concentrations of Tm^{3+} (1%, 3%, 8%, 12%, 16%) were excited with a laser beam with a wavelength of 1059 nm. A beam of this wavelength is non-resonant to the transition from the basic level and resonant to the absorption from the excited level ($^3F_4 \rightarrow {}^3F_2$) and ($^3H_4 \rightarrow {}^1G_4$). For PA to occur CR is necessary, which helps to populate the $^3F_4$ level, from where absorption from the excited state occurs. From Tm^{3+} ions occurs multicolor emission: 450 nm, 475 nm, 510nm, 646 nm, 655nm, 800 nm.

Emission spectra under 1059 nm excitation have been measured (*Figure 25*). The strongest emission occurs from level $^3H_4$ to baseline $^3H_6$. The rest of the emission occurs from the visible range.

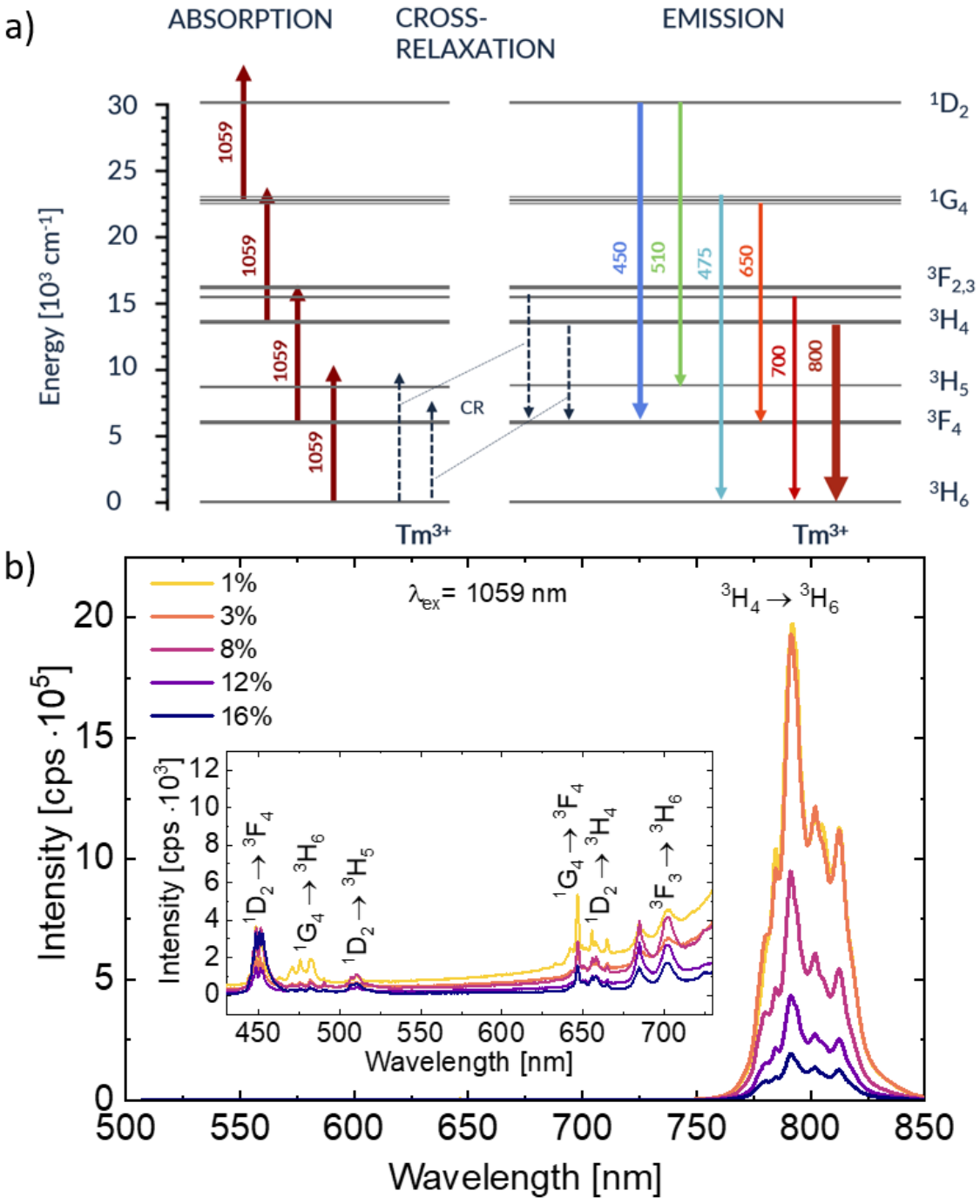

Figure 25. (a) Energy diagram of Tm^{3+} with energy transitions: absorption, energy looping and emission. (b)Emission spectrum for x% Tm doped microcrystals with energy transitions marked under 1059 nm excitation.

Then, for a few crystals from each concentration, the dependence of the luminescence intensity on the power density of the excitation laser was measured for the two strongest emissions at 800 nm and 450 nm. A single microcrystal was selected for each measurement. During measurement, the laser beam was always set to the center of the

microcrystal, so the difference in size in the crystals should not make any difference, assuming a beam that is about 1 micrometer is much smaller than the surface of the microcrystal. Each measurement was repeated several times, so the average of the parameters that describe the avalanche could be calculated. PA was successfully obtained for each concentration, as can be seen by the high nonlinearity and the characteristic s-shaped shape of the measurement results (*Figure 26*.).

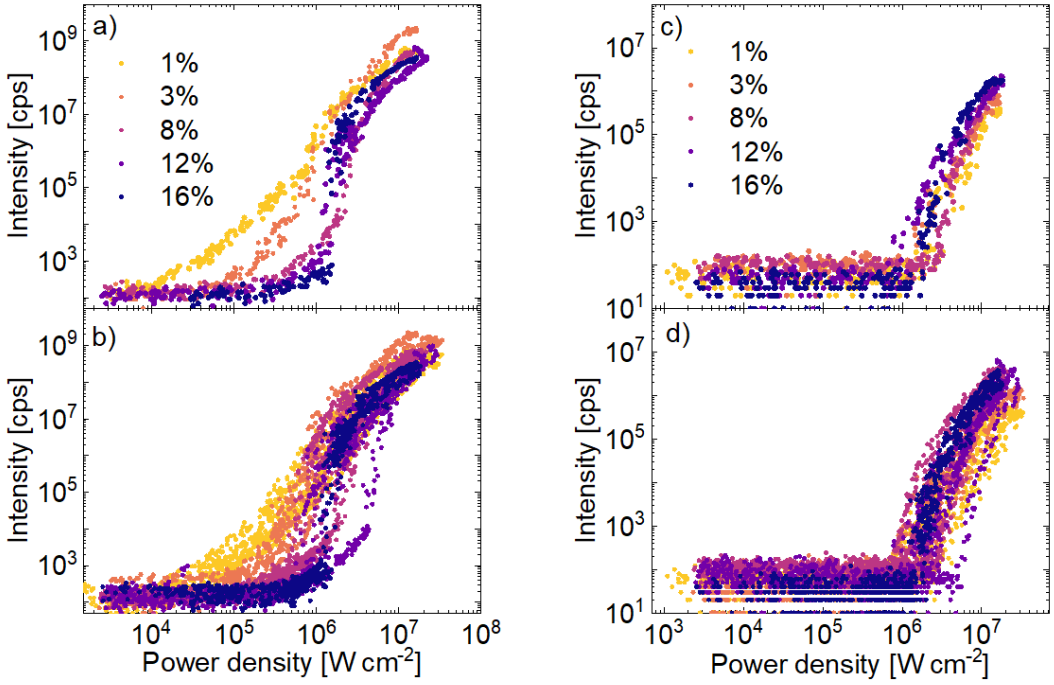

Figure 26. Dependence of luminescence intensity on the power density of the excitation laser for different concentrations of Tm in $LiYF_4$ microcrystals. a) and b) emission for 800 nm; c) and d) emission for 450 nm. a) and c) presents single middle results. b) and d) presents results from all measured crystals.

As can be seen in *Figure 26*, the concentration affects the shape of the luminescence dependence curve on the power density of the pump laser At the lowest power densities, there is an enhancement in the 800 nm luminescence for microcrystals with a 1% concentration. At first, it is an exponential increase, but with a low exponent, only then the emission begins to increase rapidly. Then luminescence appears in 3% Tm doped sample. For higher concentrations, the emission begins to appear for similar power densities. The saturation of luminescence intensity reaches a value of 10^9 [cps]. For emission at 450 nm, there is no such a clear separation in the s-shapes. The maximum luminescence intensity is of the order of 10^6 [cps], which means that the maximum

emission intensity at 475 is as much as 1000 times weaker than the maximum emission intensity at 800 nm. Panels (b) and (c) show how the PA curves for several measurements of different crystals were distributed.

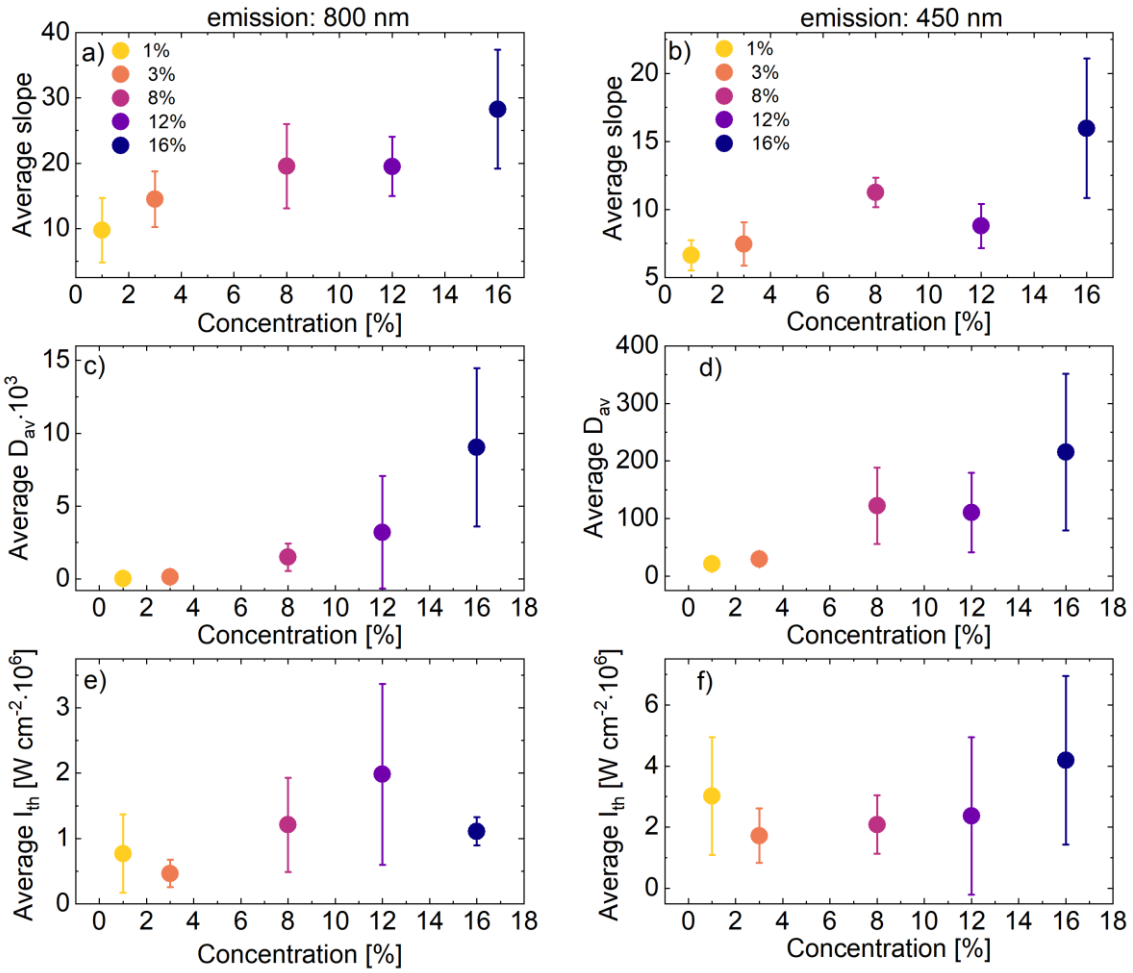

Figure 27. (a) and (b) Average PA pump non- linearity slope and (c) and (d) average PA gain D_{av} and (e) and (f) average threshold for various concentrations of Tm^{3+} ions.

For emission at 800 nm, the maximum slope of the curve increases with increasing concentration. However, the error bar increases in the same way. Average maximal slope for a concentration of 1% oscillates around 10, and for the highest concentration of 16% it averages 28. For emissions at 450 nm, the maximum slope of the curve also increases with increasing concentration. The slope for a concentration of 1% is about 6, and for the highest concentration of 16% it averages 15. Analogically, the profit parameter D_{av} increases as the concentration increases. For emission at 800 nm the average D_{av} was 39 for a concentration of 1%, and the highest for a concentration of 16% was 9028. For

emission at 450 nm the average D_{av} was 21 for a concentration of 1%, and the highest for a concentration of 16% was 215. Error bars also increased with concentration. The PA threshold was smallest for microcrystals with a concentration of 3% for both emission at 800 and 450 nm. The exact values of the parameters describing the PA can be found in table number 3.

Table 3. Parameters calculated by the algorithm in Matlab describing the PA.

	Emission 800 nm			Emission 400 nm		
Concentration [%]	Slope	D_{av}	I_{th} [W cm^{-2}]	Slope	D_{av}	I_{th} [W cm^{-2}]
1	9.71	39.05	768916.4	6.63	21.40	3019761.6
3	14.47	140.06	464410.75	7.45	29.47	1724170
8	19.53	1487.16	1208031	11.25	122.18	2089133.66
12	19.50	3205.50	1983745.5	8.78	110.65	2371499.75
16	28.27	9028.85	1109936.5	15.97	215.21	4183580

The increasing slope of the s-shape curve, with increasing Tm^{3+} concentration, may be due to increased CR, as the distance between active ions is smaller and CR increases the population of the level from which efficient ESA occurs. Thanks to these properties of the crystals, it is possible to select the optimum sample depending on the power densities for which a PA threshold is desired and which exhibits the greatest slope for the smallest avalanche threshold.

Conclusions

$LiYF_4$ microcrystals doped with different concentrations of thulium were investigated. Each of the samples exhibited PA. As the concentration increased, the avalanche samples and the slope of the luminescence intensity-power density dependence curve increased. Presumably, this is related to the more efficient CR, which influence the population of the metastable level from which the efficient ESA occurs. In addition, for higher concentrations, the maximum luminescence intensity decreases. Optimization of these crystals would therefore depend on the potential application, and this study will allow us to understand the dependence of many parameters, such as slope, D_{av}, PA threshold on the concentration of the dopant Tm^{3+}.

6.1.3. A role of AuNR on PA in Tm^{3+}

For the first time, this study delves into the interaction of thulium-doped $LiYF_4$ crystals (3% Tm^{3+} content, synthesized by Małgorzata Misiak) with plasmonic nanoparticles, specifically gold nanorods (AuNRs). The objective was to explore whether combining these materials would amplify or attenuate the emission of Tm^{3+} PA. *Figure 28* shows that the extinction of the AuNR influence the emission at 800 nm with Tm^{3+}. The investigation focused on both nano and microcrystals of 3% Tm-doped $LiYF_4$. AuNRs were intentionally chosen for their pronounced extinction band around 800 nm, aligning with the emission wavelength of Tm^{3+} ions at 800 nm. This choice differed from spherical AuNPs, which exhibit a small, single plasmonic band near 500 nm, significantly distant from the Tm^{3+} emission wavelength.

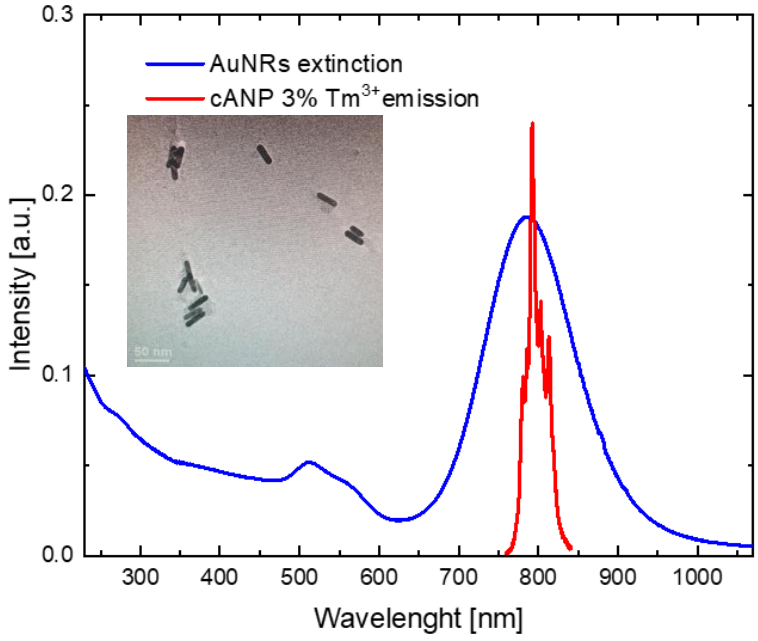

Figure 28. Extinction of gold nanorods juxtaposed with 3% Tm^{3+} ion emission in $LiYF_4$ matrix with TEM images.

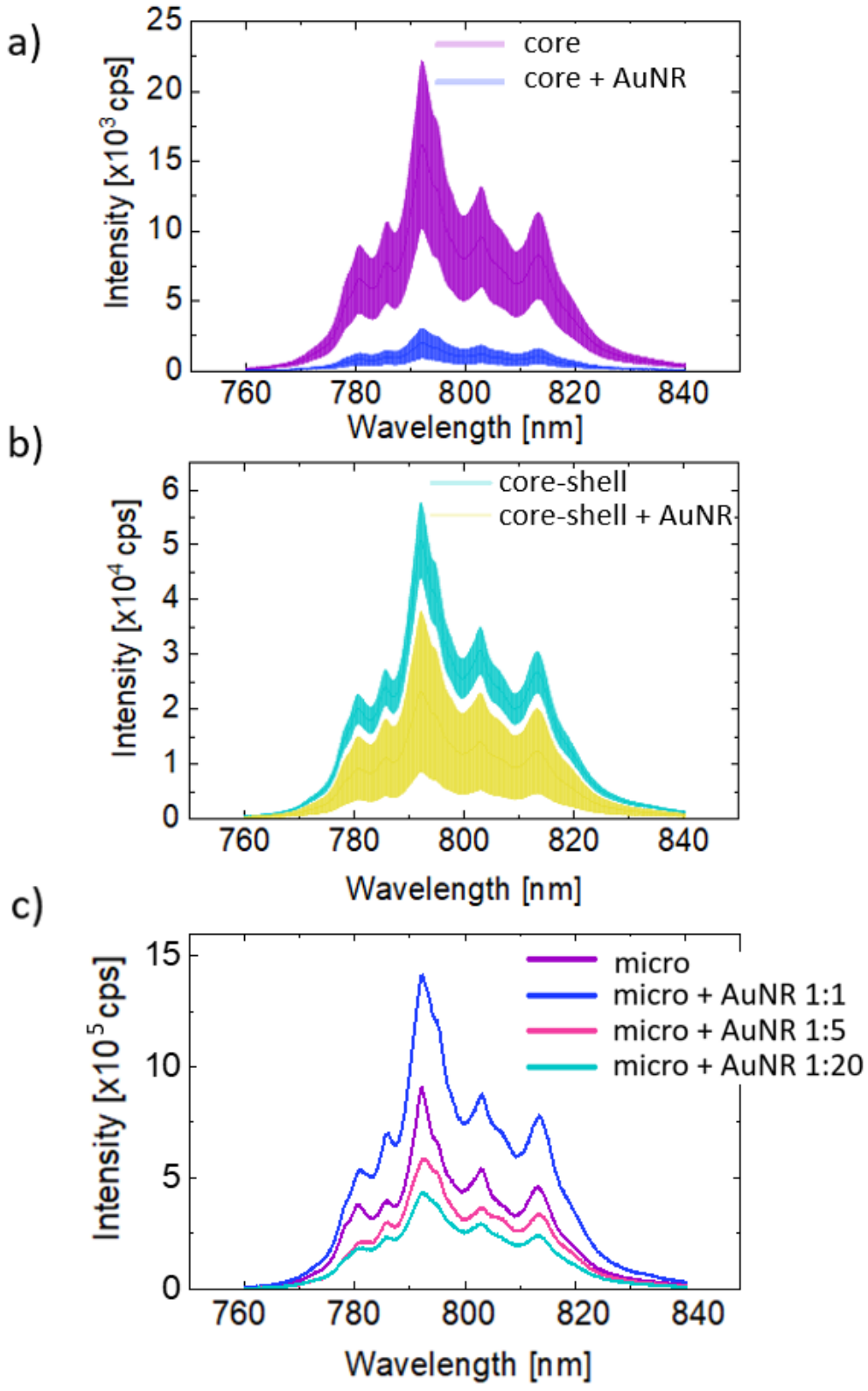

Figure 29. Tm^{3+} PA emission spectra under 1059 nm excitation. a) for core nanocrystals and core nanocrystal with gold nanorods. b) for core-shell nanocrystals and core-shell. nanocrystals with gold nanorods. c) for microcrystals and microcrystals with gold nanorods Any sample doped with 3% of Tm^{3+}.

Spectra were measured for pure core, core-shell and micro crystals and for the same materials combined with gold nanorods. The combining of gold nanorods in the case of nanocrystals involved blending two colloidal solutions, while in the case of larger microcrystals, it entailed the dropwise addition of a nanorod solution onto them. For nanocrystals, higher luminescence intensity occurs for samples without gold, when gold is added, luminescence decreases. Reduction in emission intensity of nanocrystals mixed with gold nanorods may be due to reabsorption of gold nanorods at this wavelength (800 nm). There is an energy transfer from the excited nanocrystals to the gold nanoparticles. This happens in both core and core shell nanocrystals. Core-shell nanocrystals show higher luminescence intensity due to the passive shell. The passive shell protects the crystal from surface quenching. It can be noted that in the case of the core-shell sample, the emission reduction caused by the obesity of nanorods occurs to a lesser extent.

In the case of microcrystals, there is an interesting phenomenon observed, because when gold nanorods are added in a one-to-one ratio, emission enhancement occurs. Only the addition of gold in higher concentrations of 1:5 and 1:20 results in lower luminescence.

Then, the dependence of the luminescence intensity from the density of the excitation laser power (1059 nm) was measured for core, core-shell and micro crystals pure and after mixing them with gold nanorods.

For nano crystals, when AuNR is added to both core and core-shell, the s-shape shifts toward higher powers. The presence of AuNRs cause a sudden increase in luminescence to occur at higher power densities with emission at 800 as well as 475 nm. The relationships are similar to those for spectra. In s-shape analysis I focused on emissions at 800 nm.

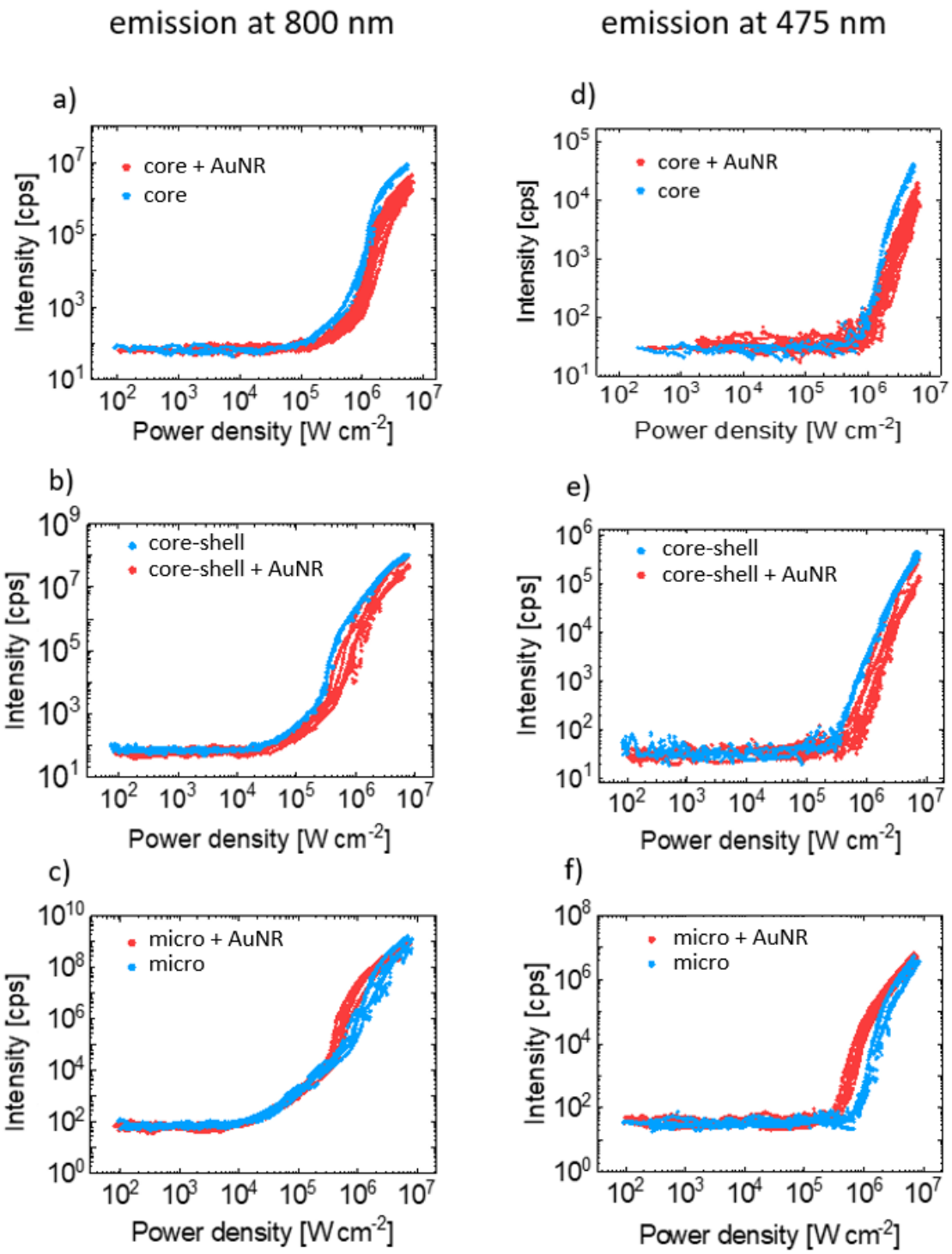

Figure 30. Dependence of luminescence intensity on the power density of the excitation laser (1059nm) a) and d) core; b) and e) core-shell. c) and f) microcrystals for emission at 800 nm and 475 nm for clean crystals and crystals with AuNR.

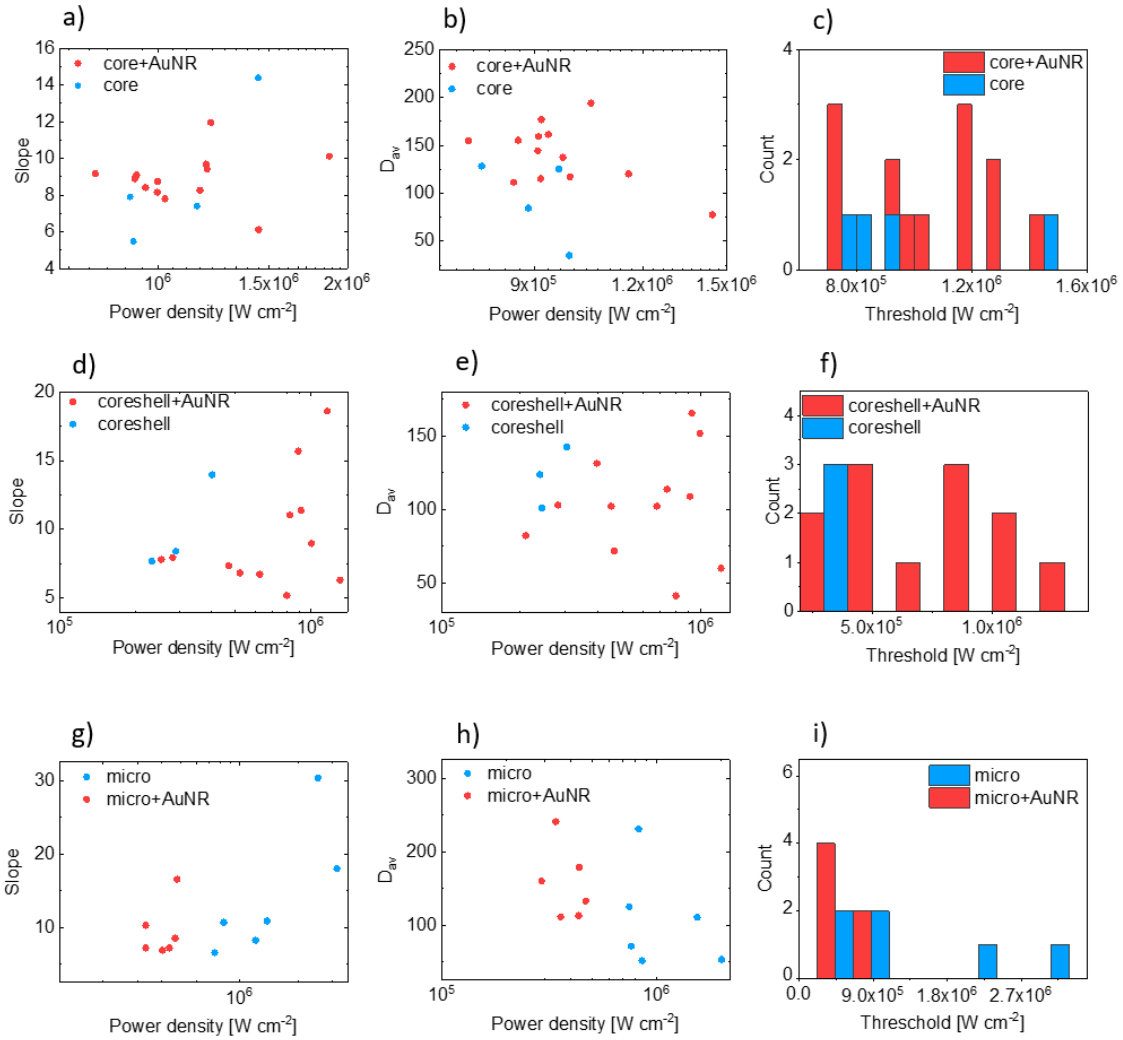

Figure 31. PA parameters. a) – c) slope, D_{av} and threshold for core and core with AuNRs, d) – f) slope, D_{av} and threshold for core-shell and core-shell with AuNRs g) – i) slope, D_{av} and threshold for micro and micro with AuNRs. Emission at 800 nm.

The hypothesis is that gold mixed with nanocrystals quenches them, because they are very close and tiny - and the small separation promotes energy transfer from nanocrystals to nanorods. On the other hand, when they are microcrystals, they are larger, even as quenching occurs on the surface itself, the deeper layers of the crystal, slightly offset, can experience amplification.

Unfortunately, we do not have very precise control over the mutual orientation of ANP-AuNR or uAP-AuNPs, so we have observed an averaged effects. Certainly, this requires many more extensive and in-depth studies.

Conclusions

Nanocrystals core and core-shell crystals as well as microcrystals of $LiYF_4$ combined with gold nanorods were investigated to determine whether the nanorods quench avalanche emission. This was confirmed at the nano scale, while quite the opposite effect, such as a lower PA threshold, occurred for smaller power densities when gold nanorods were present on the surface of microcrystals.

6.1.4. PA emission kinetic response to photoexcitation

Storage and data processing in electronic devices typically involve a series of elementary binary operations. Emerging methods, such as neuromorphic or reservoir computing, are gaining rapid interest. In these approaches, data processing occurs at a relatively slow pace but can be executed comprehensively or in parallel, much like neuronal circuits. In this context, we have discovered the time-domain, all-optical information processing capabilities of PA nanoparticles.

The demonstrated functionality is similar to the properties commonly found in neuronal synapses, including paired-pulse facilitation, short-term internal memory, in situ plasticity, processing of multiple inputs, and an all-or-nothing threshold response. Moreover, the high nonlinearity of luminescence intensity in response to photoexcitation imitates and amplifies spike-timing-dependent plasticity.

This study not only delves into the previously unexplored fundamental properties of photon-avalanche luminescence kinetics but also offers the prospect of all-optical data processing. This potential is further enhanced when combined with recent advancements in photonics.

All measurements were made on nanocrystals $NaYF_4$:8%Tm@10.2nm$NaYF_4$ synthesized by Małgorzata Misiak.

In the next step, rise times were measured for different offset (from 0 mA to 538 mA) (*Figure 32*a) and for different time delays followed by a pulse (1 ms to 100 ms) (*Figure 32b*).

The dynamics of the rise time depends on the initial occupancy of the metastable state. This has been demonstrated using two methods: using pre-pumping (where a higher initial occupancy led to a faster increase in emission) and not allowing the system to fully "discharge" energy after the previous excitation. In the latter case, the increased occupancy of the metastable state resulted in a faster rebuilding of emission during subsequent excitation pulses. As there is an initial, oddment/residual population of electrons in the metastable state, the whole energy looping process is more efficient as compared to the situation when this levels is empty - assuming that each step of ESA and then CR doubles the population of this metastable level, then at the beginning we have this occupancy changing in the simplest case like this: 1, 2, 4, 8, 16, 32, 64,... grows exponentially. But as we start when there is still, for example, 32 there, it grows like this: 32, 64, 128, 256, 512, 1024, 2024 - in the same number of steps we already have many more.

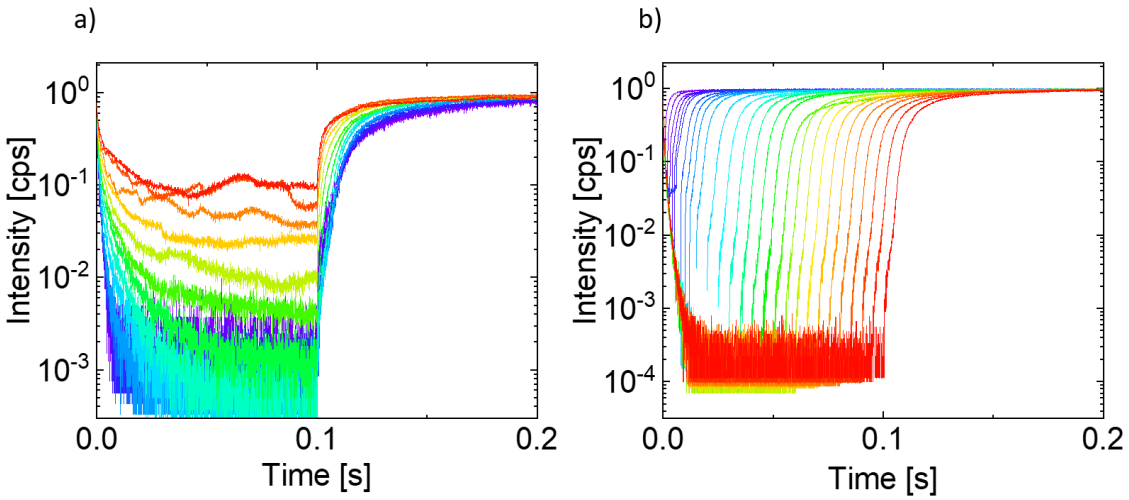

Figure 32. Rise times for (a) different offset and (b) for different time delay.

Variations in the duration of illumination needed to achieve half of the steady-state emission intensity (t50% is the time (t) after which the luminescence intensity (I_L) reaches 50% of its maximum saturated intensity (I_{SAT}), i.e. $I_L(t50\%) = ½\ I_{SAT}(t= \infty)$) were examined for different delays between consecutive excitation pulses (Δ). The data were fitted using an exponential curve, depicted in red, with a time constant (τ) of 18.7 ± 3.1 ms. The t50% values were derived from the experimental outcomes presented in *Figure 32*. The experiments were conducted with an excitation power density of 250 kW cm^{-2}.

PA regeneration strongly depends on the temporal interval between successive pulses (*Figure 32*b) or the population of remaining ions in the intermediate level (*Figure 32*a),

which are key components of the short-term synapse memory effect. Longer intervals, or lower residual stimulus intensities, slow down the regeneration time (50% rise time parameter).

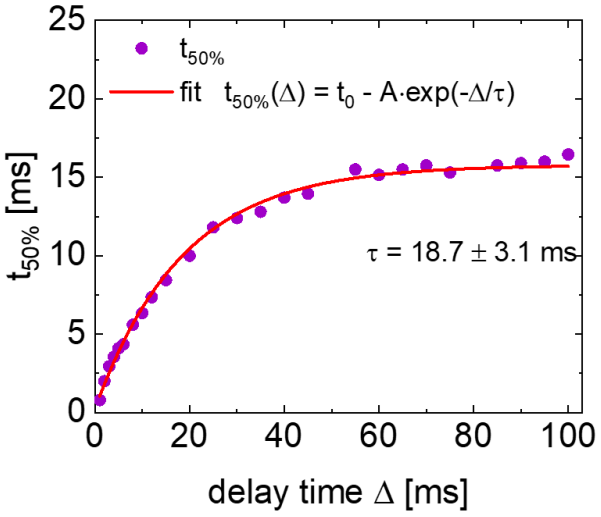

Figure 33. t50%, depending on the time delay between incremental times.

The optical synapse emulates the principle of operation of biological synapses, as their optical response varies depending on the spatial-temporal modulation of optical excitation signals. The optical synapse exhibits short-term memory.

The next experiment involved increasing the time distance between the two pulses (*Figure 34*). It can be seen that the shorter the gap between two subsequent pulses is, the higher the luminescence intensity, which means that the circuit has not been fully 'discharged'. Bare in mind the logarithmic Y scale, emphasizing the substantial differences between consecutive impulses. The PA synapse exhibits the paired-pulse facilitation (PPF) effect, as evidenced by the fact that the intensity of avalanche emission depends on the time interval between successive pulses. PPF amplifies the response depending on previous stimulation.

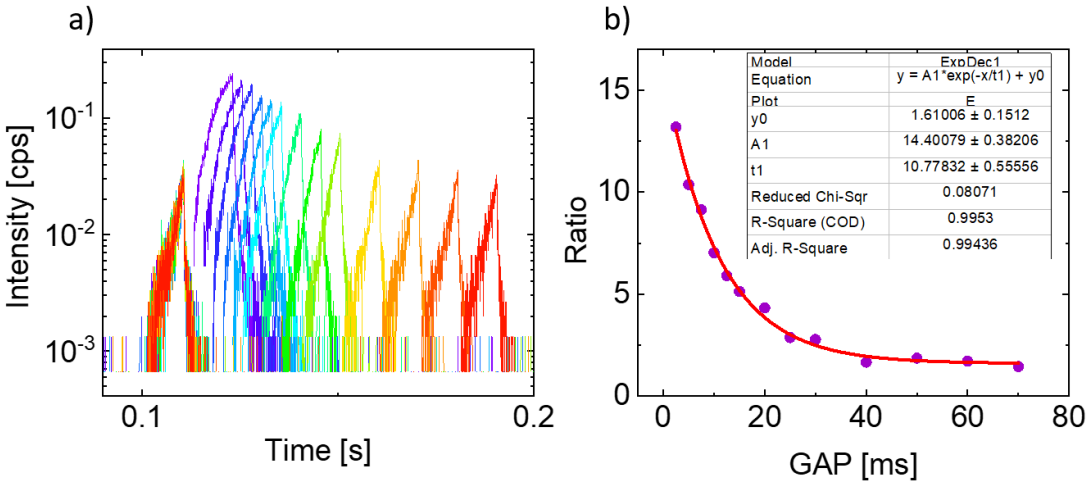

Figure 34. Intensity of pulses with different time distance b) The ratio of the sum of the second pulse to the first depending on the gap between them.

In the next step, the ratio of the sum of the second pulse to the first was calculated (*Figure 34*). The smaller the distance, the greater the ratio was. For the smallest gap between pulses the ratio was 13, and for the largest the ratio was less than 2.

Then an experiment simulating logic gates was performed. The graphs show luminescence intensities as a function of time. *Figure 35. a)* shows an AND logic gate, for a shorter pulse *Figure 35. b)* an AND logic gate for a longer pulse, and *Figure 35. c)* shows the superimposition of two pulses offset from each other. Where the two pulses overlapped, the intensity of the luminescence was significantly (ca. 10-fold) higher.

The distinctly nonlinear relationship between PA emission intensity and pump intensity, combined with a comparatively extended existence of the intermediate level, along with ESA excitation and inefficient GSA, results in a behavior that stands out from conventional fluorescent species. By precisely adjusting the intensities of input pulses, the input information can selectively initiate PA emission, mimicking the functionality of a digital AND gate (*Figure 35*). Intriguingly, this artificial PA synapse can handle more than two inputs and accommodate analog input weighting, introducing associativity and spatiotemporal behavior—features originally identified in biological and artificial neural networks. These findings underscore the suitability of the PA synapse for detecting temporal coincidences between input signals.

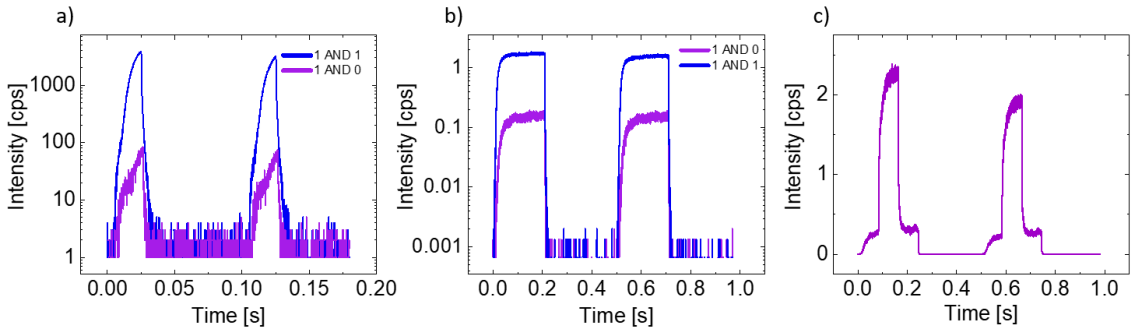

Figure 35. Logic gate AND (a) shorter pulses (b) longer pulses (c) offset pulses.

Phase-sensitive detection

Experiments exploring the phase detection between two signals of the same frequency were conducted using a microscopic setup. This setup allowed for time-resolved excitation of the photon-avalanching nanocrystals, simulating phase-controlled overlap of these excitation signals. The signal was adjusted to ensure that, during signal overlap, the excitation power density equaled 250 kW cm-2, while outside the overlap, the signal power density was twice as low. The phase was systematically changed from 0° (perfect signal overlap) to 180° (signals in anti-phase) in 5° increments. The diagrams depicting the corresponding emission from the photon-avalanching nanocrystals are presented in *Figure 36.* In the case of a linear dependence between luminescence intensity and pump intensity, there would be no variation in integral luminescence intensity concerning phase-shifted fluorescence signals.

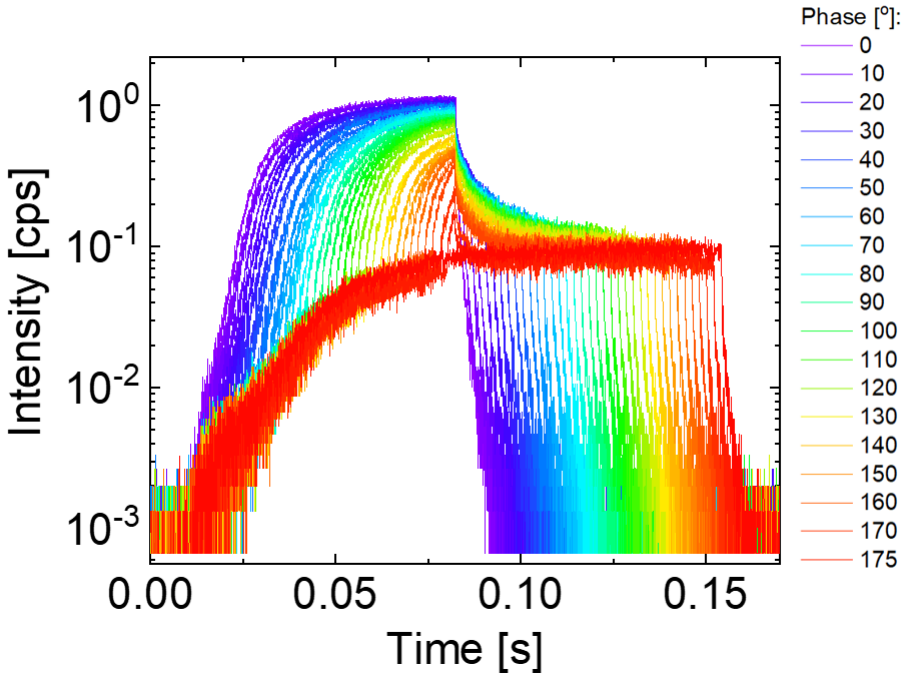

Figure 36. Experimental illustration of the emission intensity dynamics in a photon avalanching system during excitation by a signal formed by combining two signals with different phase shifts (0°-180°) between them.

Conclusions

PA measurements enable the entirely optical processing of intricate signals. The luminescence induced by material pulses is influenced by the time intervals between successive, identical excitation pulses. PA synapse exhibit a phenomenon called PPF, which amplifies the response depending on previous stimulation.

The mentioned properties share similarities with synaptic functioning, and these analogies can be applied for optical amplification, entirely optical signal processing, and information storage.

6.1.5. Influence of Tb^{3+} doping on PA in Tm^{3+} microcrystals

In this study, we aimed to demonstrate and evaluate the sensitivity of the PA phenomenon to the presence of an energy acceptor resonating with the looping state. To achieve this, $LiYF_4$ microcrystals were co-doped with 3%Tm^{3+} and various percent of Tb^{3+} ions and analyzed the results of experiments. PA-based sensing or biosensing relies on detecting substantial changes in the emission response caused by small perturbations in the energy looping required for the PA phenomenon.

The energy level - $^7F_0$ in Tb^{3+} was found to be resonant with the $^3F_4$ energy level in Tm^{3+}, which actively participates in the CR based energy looping, which is necessary for the PA phenomenon to obtain. This resonance leads to a high probability of ET from the Tm^{3+} ions excited state to Tb^{3+}, followed by subsequent non-radiative relaxation to the ground state of Tb^{3+} ions.

To explore the impact of energy looping disruption on the characteristics of the PA phenomenon, dr. Małgorzata Misiak synthesized and characterized $LiYF_4$ microcrystals doped with Tm^{3+} ions and co-doped with varying concentrations (0.01%, 0.05%, 0.1, 0.3%, 0.5%, 1% 3%) of Tb^{3+} ions. Through this study, we sought to understand how the presence of terbium ions affects the PA behavior in the microcrystals and gain insights into the potential modulation of the PA response by varying the terbium doping concentration. In the microscale studies, we aimed to deliberately eliminate surface effects that would undoubtedly occur in nanomaterials, in order to focus solely on the interaction/quenching of Tm^{3+} to Tb^{3+}.

The crystallographic purity of the synthesized microcrystals is confirmed by X-ray powder diffraction (XRD). It shows a pure tetragonal phase of $LiYF_4$. XRD data for all the synthesized samples are presented in *Figure 37.* In accordance with the pattern from ICSD no. 73709, all the samples exhibit a pure tetragonal structure of $LiYF_4$. The variations observed in the relative intensity of specific XRD peaks are likely attributed to the differing orientations of relatively large microcrystals concerning the incident X-ray beam.

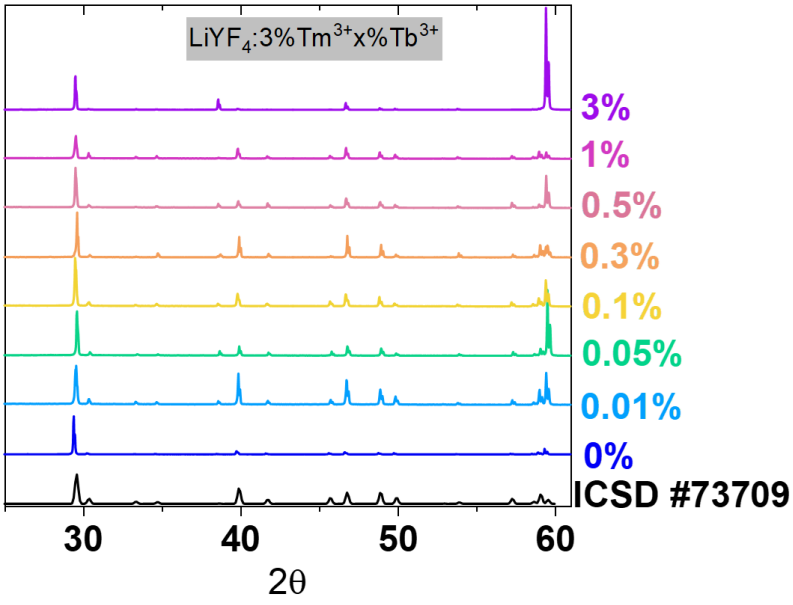

Figure 37. Powder X-ray diffraction data of the synthesized $LiYF_4$ microcrystals doped with 3% Tm^{3+} and varying concentrations of Tb^{3+} ions are presented.

The purity of the synthesized microcrystals was subsequently confirmed through SEM images (*Figure 38*), which reveal microcrystals with a bipyramidal morphology for all the samples synthesized. These microcrystals exhibit varying sizes, ranging from an average of 62 µm for the undoped terbium materials to 124 µm for microcrystals doped with 3%Tb 3%Tm.

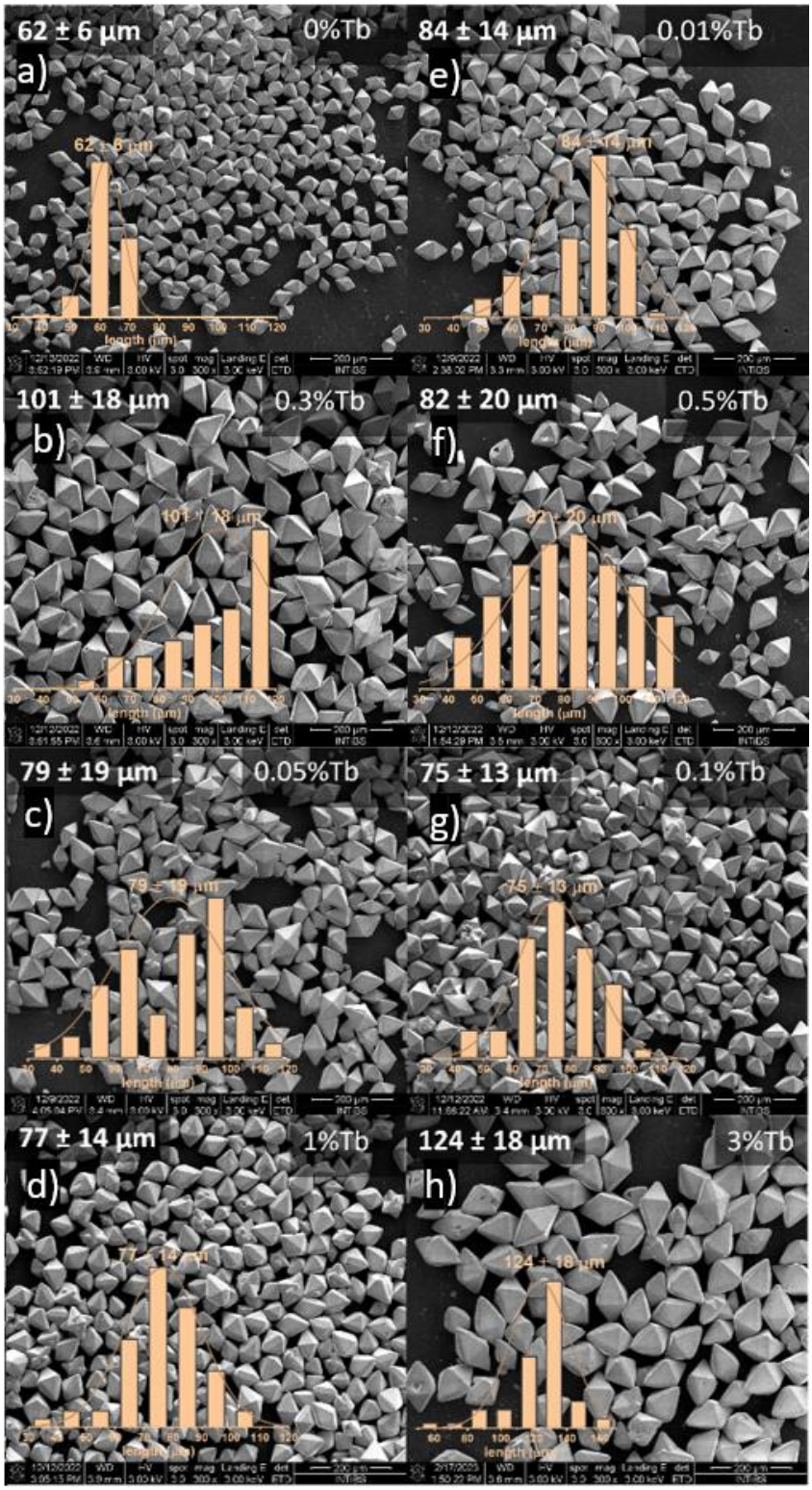

Figure 38. Scanning electron microscope images of the synthesized $LiYF_4$ microcrystals doped with 3% Tm^{3+} and co-doped with varying concentrations of Tb^{3+} ions are provided. The average microcrystal size for each sample is determined from the respective normal distribution curve of microcrystal lengths.

Under excitation at 1059 nm, $LiYF_4$:3%Tm^{3+} microcrystals emit light from the visible and NIR regions. These emissions correspond to the following transitions from $^1D_2$ (for 450, 510 and 650 nm), $^1G_4$ (for 475 and 650 nm), $^3F_2$ (for 684 nm), $^3F^3$ (for 700 nm) and by far the most intense from $^3H_4$ (for 800 nm). In the Tb^{3+} doped system, CR and ET processes contribute to a drastic reduction in all observed emissions.

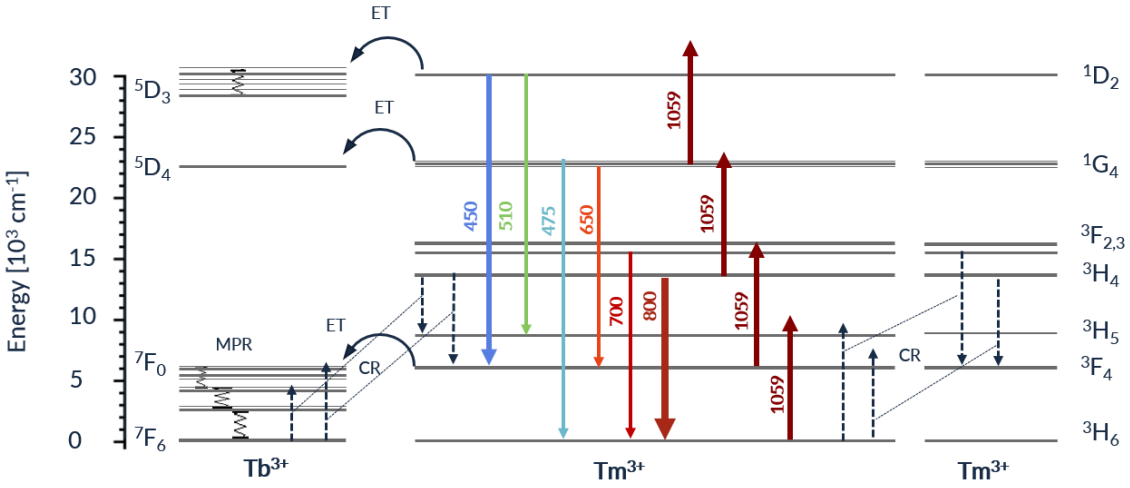

Figure 39. Energy diagram in Tm^{3+} and Tb^{3+} ions.

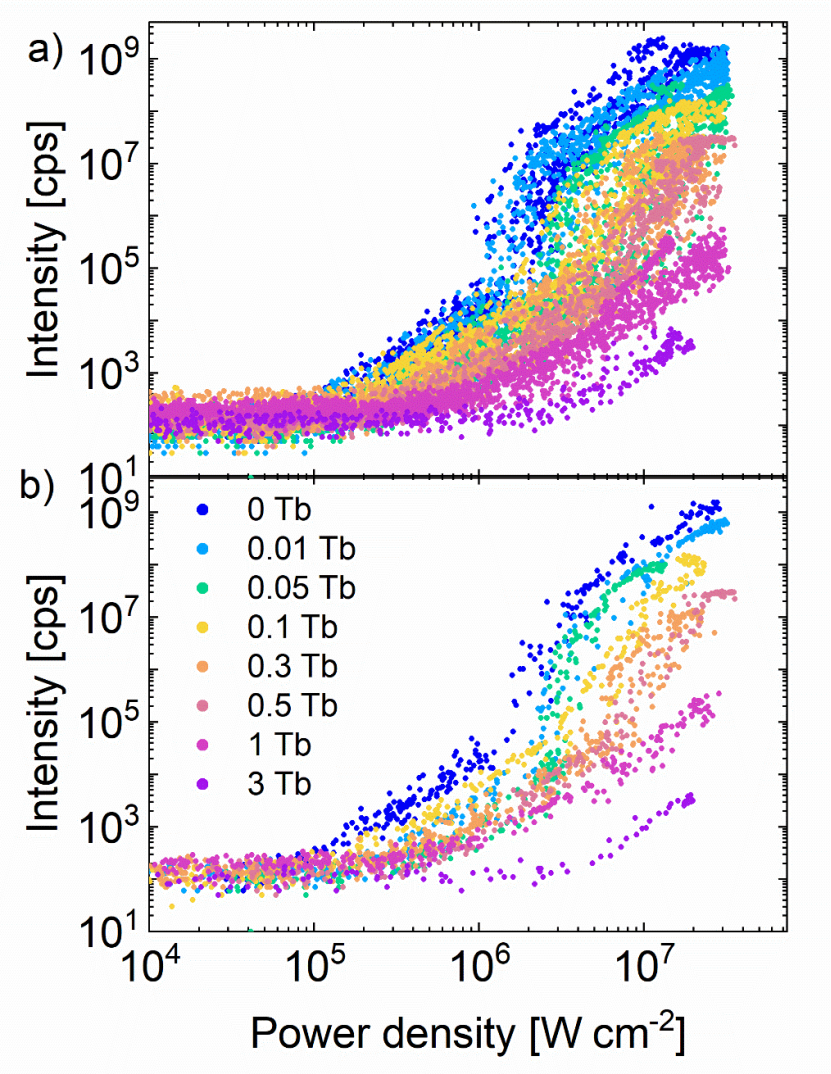

Figure 40. Power dependent luminescence of Tm^{3+} ions, emission at 800 nm.

The luminescent intensity of the $^3H_4 \rightarrow {}^3H_6$ transition, upon excitation at 1059 nm, exhibits a notable decrease with an increasing concentration of terbium ions. With a rise in the concentration of Tb^{3+} ions, the likelihood of a Tb^{3+} ion being in close proximity to a Tm^{3+} ion also rises.

In samples where the terbium ion concentration matches that of thulium ions (i.e., 3%), the PA threshold experiences a significant increase. Consequently, there is no complete S-shaped pattern of PA observed within the utilized power density range. Furthermore, the PA slope, initially reaching 30 at 0.05% Tb^{3+} doping (*Figure 41*), begins to decline as terbium ion concentrations increase, ultimately reaching a value of approximately 3 for a sample containing 3% Tm^{3+} and 3% Tb^{3+} . Similar changes are observed for the PA blue emission from the higher $^1D_2$ energy level of Tm^{3+} measured at 450 nm.

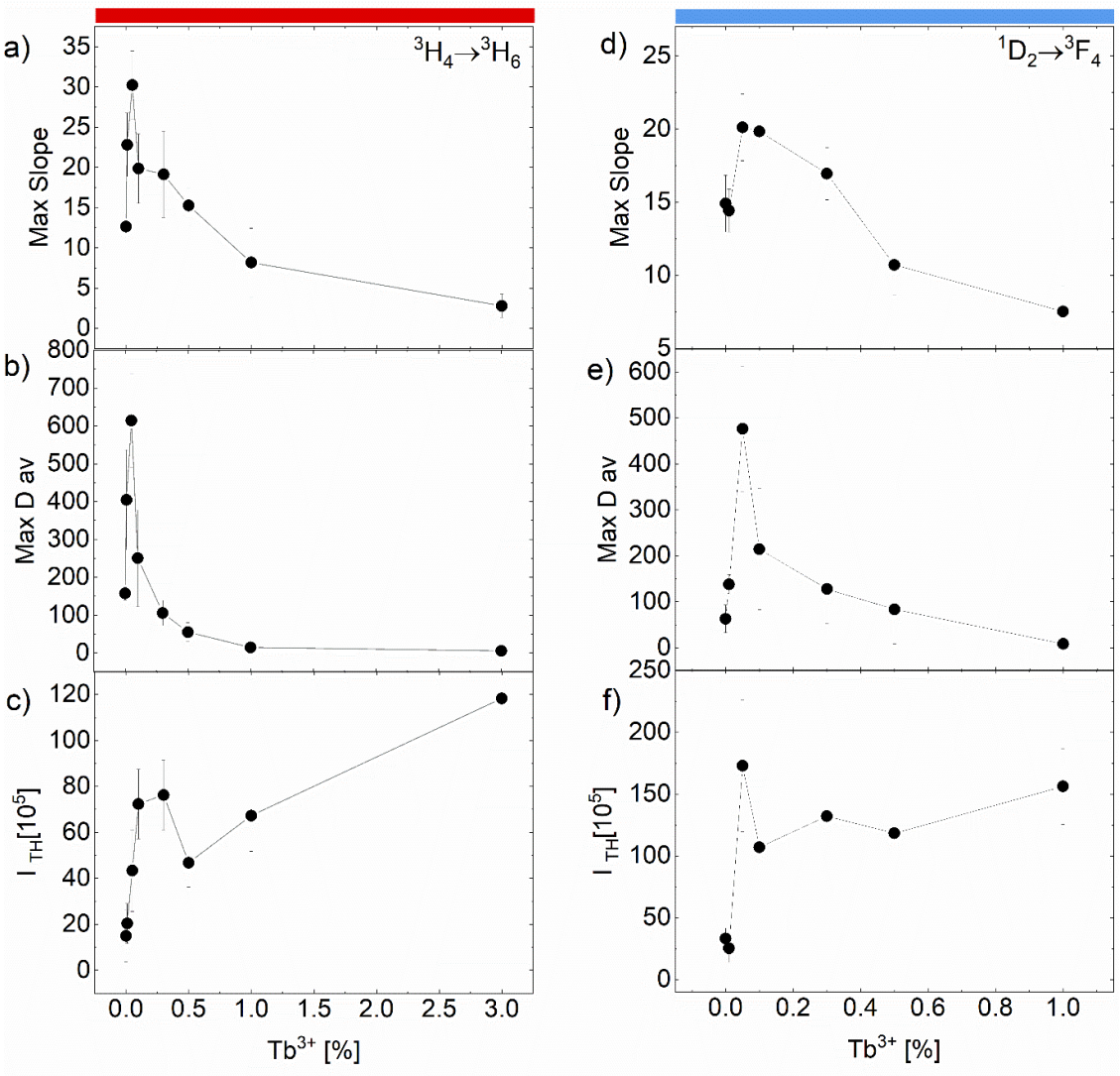

Figure 41. PA parameters calculated using a Matlab script obtained from measuring the power dependence of Tm^{3+} emission at 800 nm ($^3H_4 \rightarrow {}^3H_6$) a) b) and c) and at 450 nm ($^1D_2 \rightarrow {}^3F_4$) d) e) and f) for various concentration of Tb^{3+} ions. PA parameters for the emission at 450 nm were calculated only to 1% concentration of the Tb^{3+} with because for higher Tb^{3+} concentrations the emission was completely quenched.

As we increased the Tb^{3+} concentration, the interruption of the energy looping became more pronounced, leading to substantial changes in both the $^3H_4 \rightarrow {}^3H_6$ emission intensity and the PA threshold.

Conclusions

In summary, the avalanche emission behavior of thulium is notably influenced by the presence of Tb^{3+} ions – energy acceptors. This influence is evident in the shift of the PA threshold towards higher excitation power densities and a reduction in the PA slope at higher terbium concentrations and a reduction of several orders of magnitude in luminescence intensity. This observation highlights the potential of Tb^{3+} doping as a viable method to modulate and control the PA response. In the future, such discoveries could have promising implications for the development of PA-based biosensing and sensing applications, where precise control over the PA phenomenon can significantly enhance the sensitivity and accuracy of the detection process.

6.1.6. Impact of the passive shell thickness on PA in Tm^{3+}

In order to further investigate and learn about avalanche photon emission in nanomaterials and see how shell protects the nanocrystal from surface quenching, a series of nanoparticle samples with a circular core-shell architecture, differing in coating thickness, were synthesized by dr. Małgorzata Misiak. These are nanoparticles with $NaYF_4$ matrix doped with 8% Tm^{3+}.

TEM (*Figure 42*) images and X-ray diffraction (*Figure 43*) confirm the morphological and structural purity of the nanocrystals. TEM images determined the average size of the nanocrystals, which were as follows: nanocrystals with a core architecture were around 18 nm, crystals with a core shell architecture with a shell thickness of 2 nm - 22nm, crystals with a core shell architecture with a shell thickness of 6.5 - 31 nm, crystals with a core shell architecture with a shell thickness of 10.2 - around 38.8 nm.

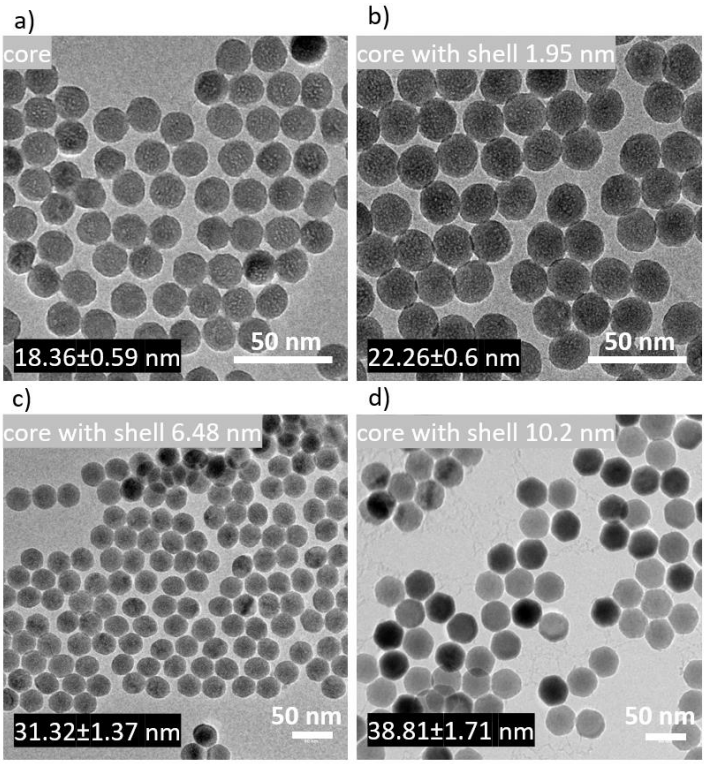

Figure 42. TEM images of $NaYF_4$ a) core, b) core with shell thickness 1.95 nm c) core with shell thickness 6.48 nm d) core with shell thickness 10.2 nm.

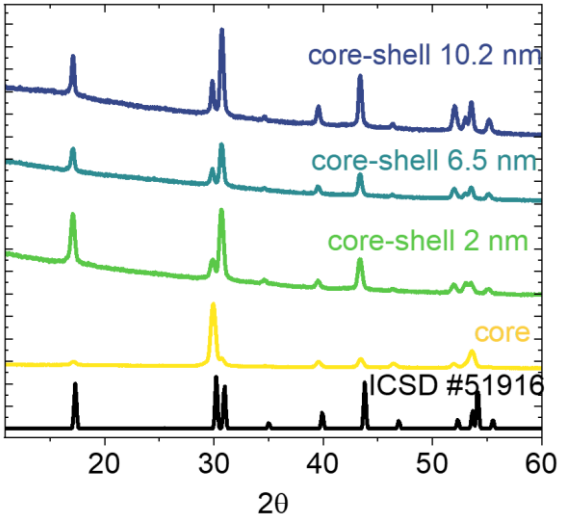

Figure 43. Powder X-ray diffraction data of the synthesized $NaYF_4$ nanocrystals doped with 8% Tm^{3+} with varying shell thickness are presented.

Emission spectra were measured for each sample at 1059 nm excitation. It is not possible to compare the emission intensities because the nanocrystals were deposited on a slide and then measurements were taken from the dried layer.

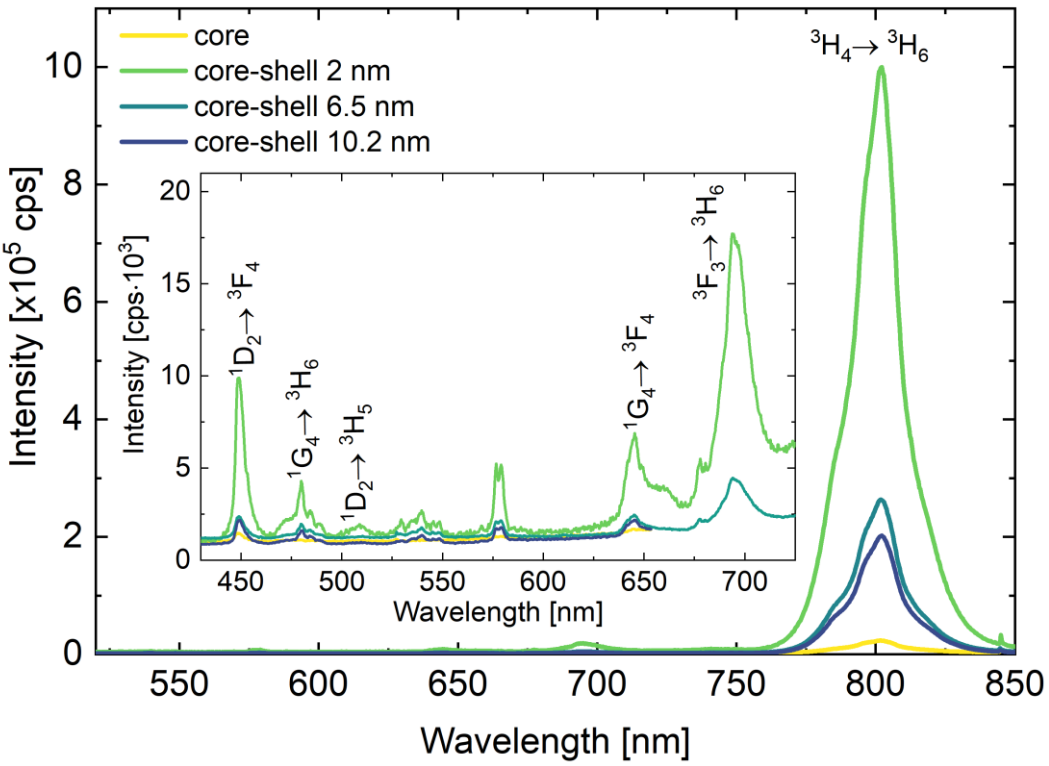

Figure 44. Emission spectrum of $NaYF_4$:8%Tm^{3+}@$NaYF_4$ with various shell thickness: 2 nm, 6.5 nm, 10.2 with signed energy transitions.

Luminescence intensities as a function of power density were measured for emission at 800 nm and 450 nm (*Figure 45*). The excitation beam emitted light with a wavelength of 1059 nm.

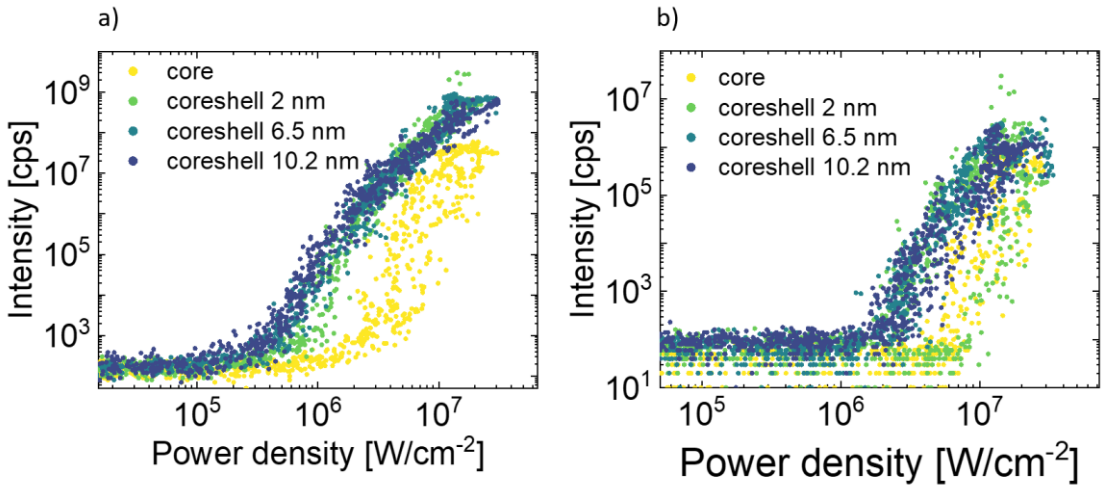

Figure 45. Power dependent luminescence of Tm^{3+} ions, emission at a) 800 nm and b) 450 nm.

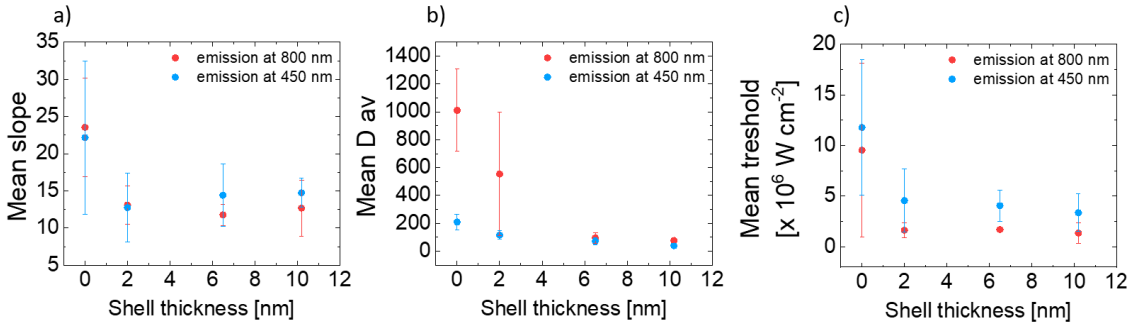

Figure 46. PA parameters calculated using a Matlab script obtained from measuring the power dependence of Tm^{3+} emission at 800 nm and 450 nm. a) mean slope, b) mean Dav and c) mean threshold.

The steepest slope of the s-shape curves is around 23 for the nanocrystals that have the largest shell of 10.2 nm, for other shell thicknesses it varies around 13-15 (*Figure 46*). The highest threshold occurred for core nanocrystals and decreased with increasing shell.

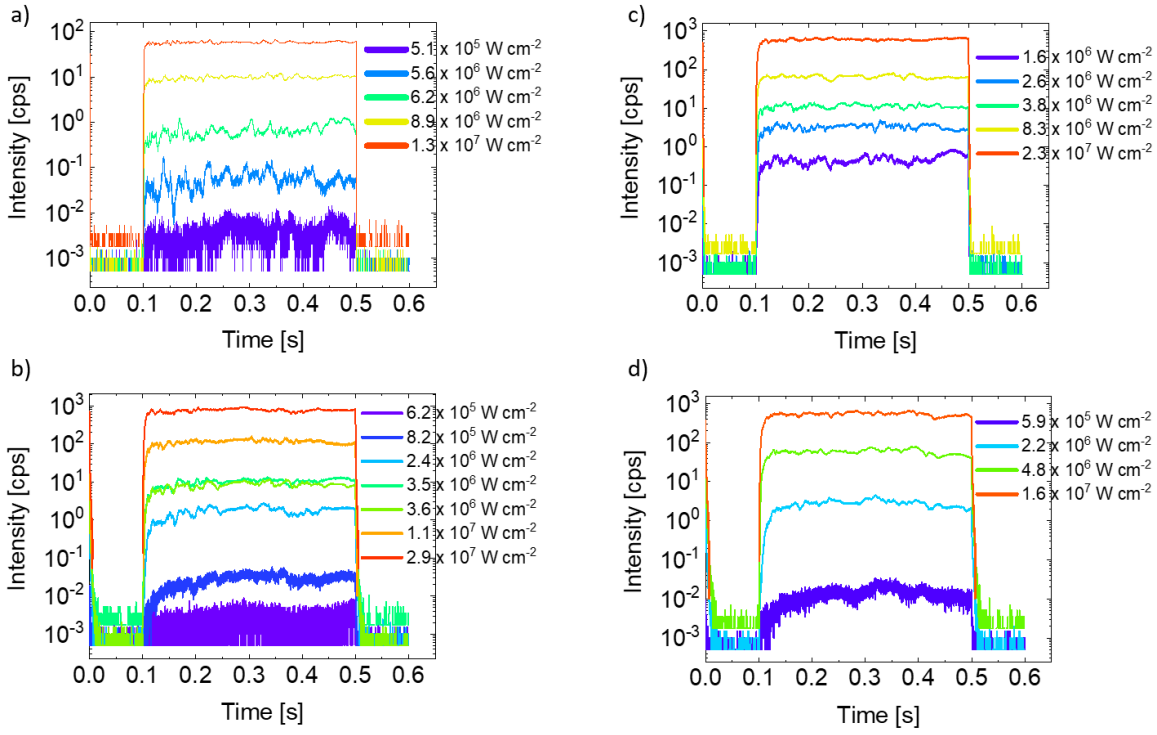

Figure 47. Rise and decay times for different excitation laser powers under the excitation 1059 nm for a) core b) core-shell 2 nm, c) core-shell 6.5 nm, d) core-shell 10.2 nm.

To further investigate and understand the phenomenon of PA emission in nanomaterials and to examine how the shell protects the nanocrystal from surface quenching, dr. Katarzyna Prorok synthesized a series of samples with varying shell thickness (Table 4). These nanoparticles are composed of $NaYF_4$ matrix doped with 8% Tm^{3+}. This time, the shell, in some cases, was not spherical but elongated. TEM images (*Figure 48*) and X-ray diffraction (*Figure 49*) confirm the morphological and structural purity of the nanocrystals. The TEM images determined the average size of the nanocrystals.

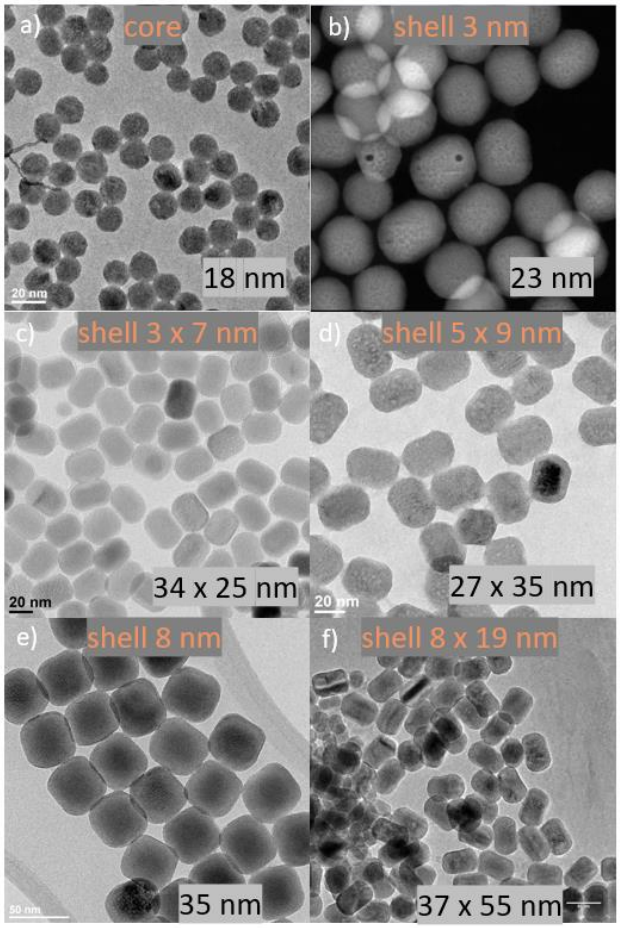

Figure 48. TEM images of $NaYF_4$ a) core, b) core with shell thickness 3 nm c) core with shell thickness 3 x 7 nm d) core with shell thickness 5 x 9 nm e) core with shell thickness 8 nm f) core with shell thickness 8 x 19 nm.

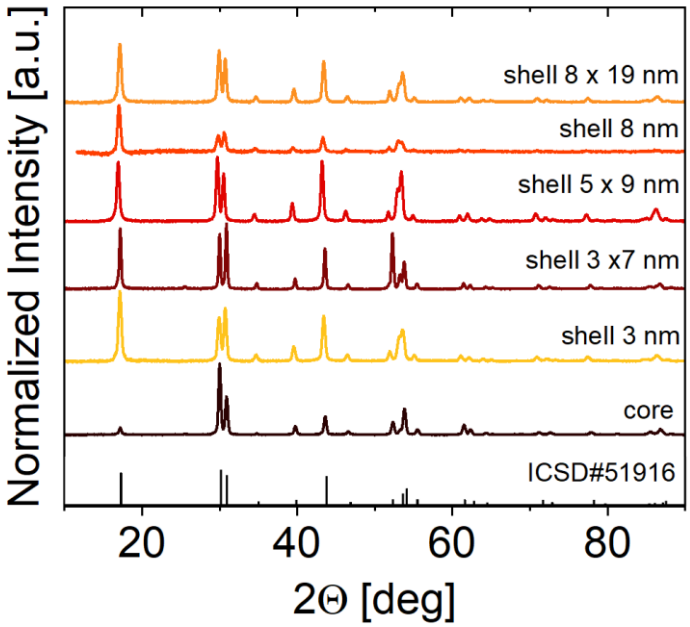

Figure 49. Powder X-ray diffraction data of the synthesized $NaYF_4$ nanocrystals doped with 8% Tm^{3+} with varying shell thickness are presented.

Below, Table 4 shows the size of the nanoparticles, the thickness of the shell and the ratio of the volume of the shell to the volume of the nanoparticle.

Table 4. Table comparing nanoparticle sizes, shell thickness and the ratio volume of the shell to the volume of the nanoparticle.

sample	Size NPs [nm]	Shell thickness [nm]	Ratio volume shell/ volume NPs
Core $NaYF_4$:8%Tm^{3+}	18	0	-
Core-shell $NaYF_4$:8%Tm^{3+}@ $NaYF_4$	34x25	3x7	0.98
Core-shell $NaYF_4$:8%Tm^{3+}@ $NaYF_4$	37x55	8x19	0.99
Core-shell $NaYF_4$:8%Tm^{3+}@ $NaYF_4$	27x35	5x9	0.98
Core-shell $NaYF_4$:8%Tm^{3+}@ $NaYF_4$	35	8	0.71
Core-shell $NaYF_4$:8%Tm^{3+}@ $NaYF_4$	23	3	0.32

First, I measured the spectra for all the samples (*Figure 50*). There is a very strong emission at 800 nm, which is responsible for the energy transition from the level of $^3H_4 \rightarrow {}^3H_6$. Then I measured spectra in the visible light range. I focused on the 450 nm emission, which corresponds to the transition from the energy level of the $^1D_2 \rightarrow {}^3F_4$. For these two emissions bands, I measured their pump power dependence.

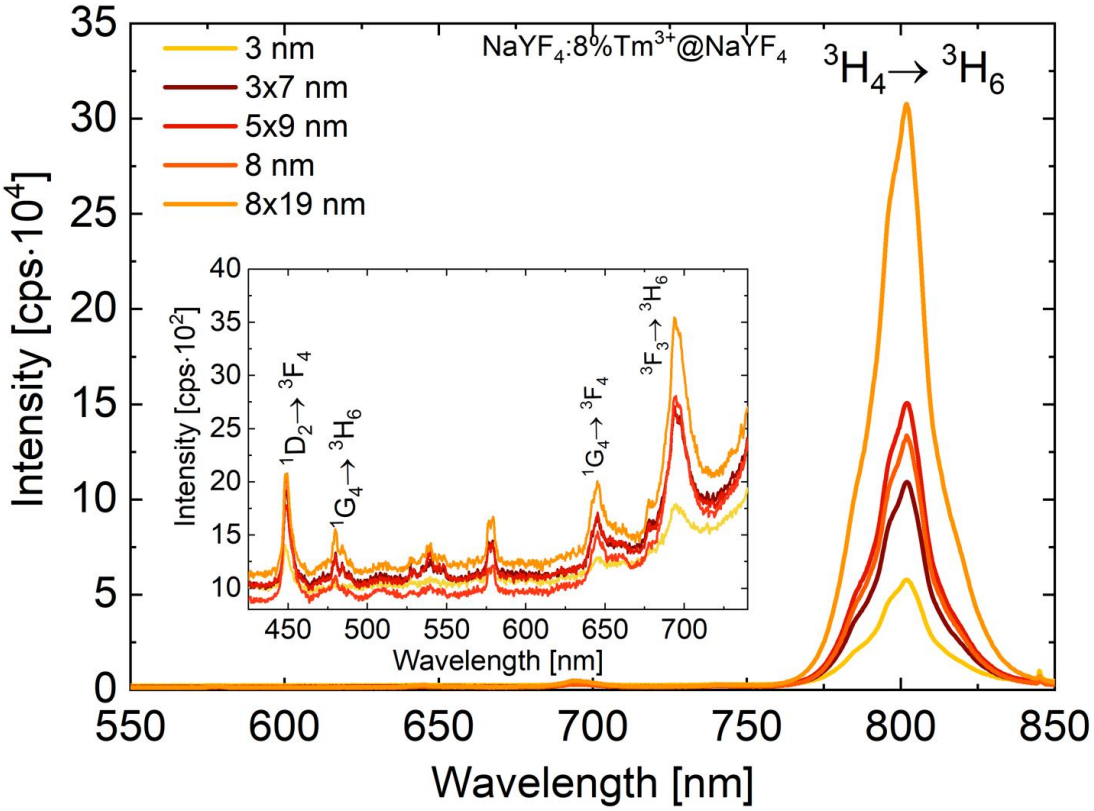

Figure 50. Emission spectrum of $NaYF_4$:8%Tm^{3+}@$NaYF_4$ with various shell thickness: 3 nm, 3x7 nm, 5x9 nm, 8 nm, 8x19 nm with signed energy transitions.

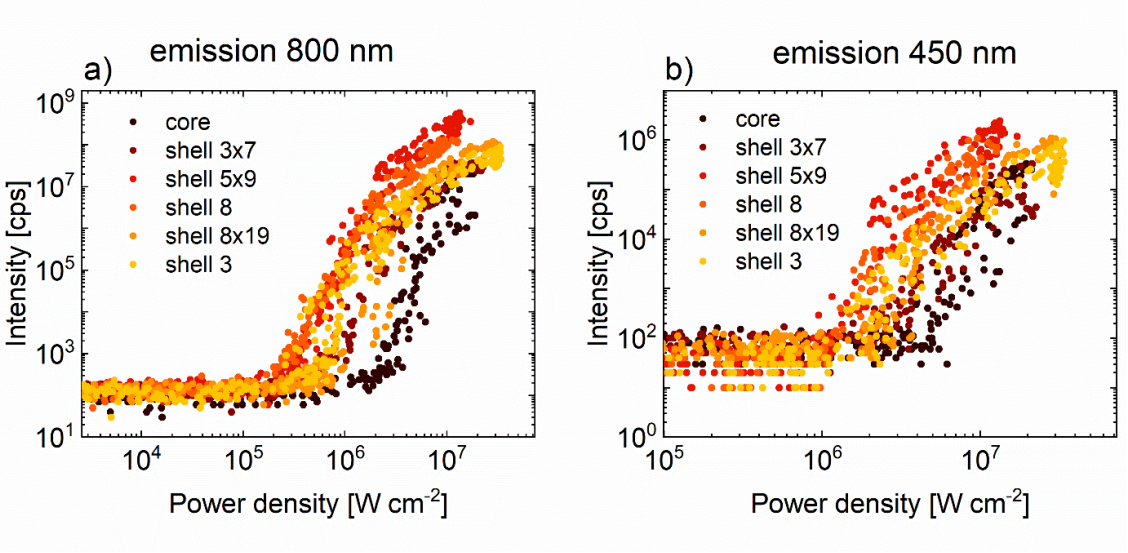

Figure 51. Dependence of luminescence intensity on the power density of the excitation laser for different shell thickness in $NaYF_4$ nanocrystals doped with 8% Tm^{3+}. a) emission at 800 nm and b) emission at 450 nm.

It can be observed that the shell thickness affects the PA. In the case of the sample containing only the core, the PA threshold was shifted towards higher excitation laser powers. The highest slope, reaching 25, occurred for the sample with a shell thickness of 3 nm, but compared to other samples, it also had a relatively high PA threshold.

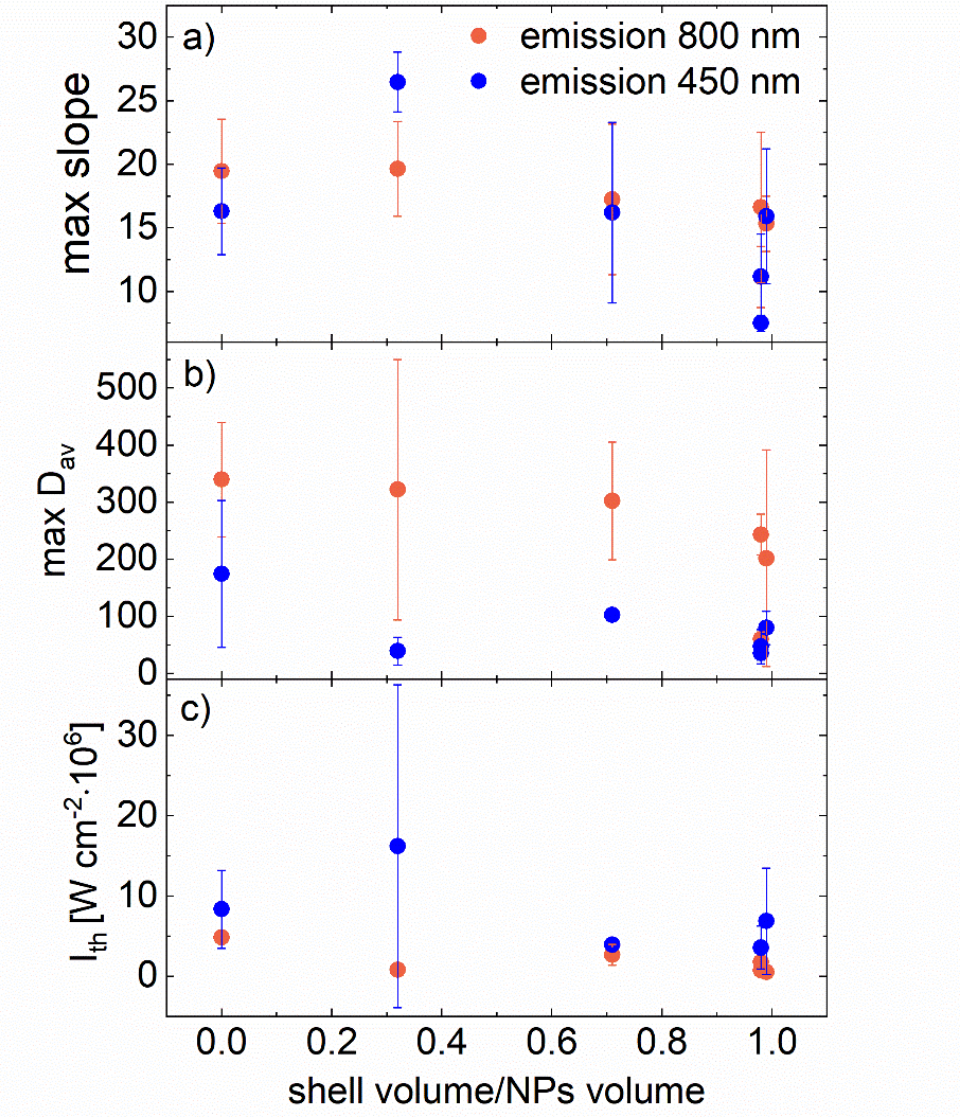

Figure 52. PA parameters, red for emission at 800 nm, blue for emission at 450 nm a) average max slope; b) average max D_{av} ; c) average PA threshold.

The kinetics were then measured for different excitation laser powers (*Figure 53*).

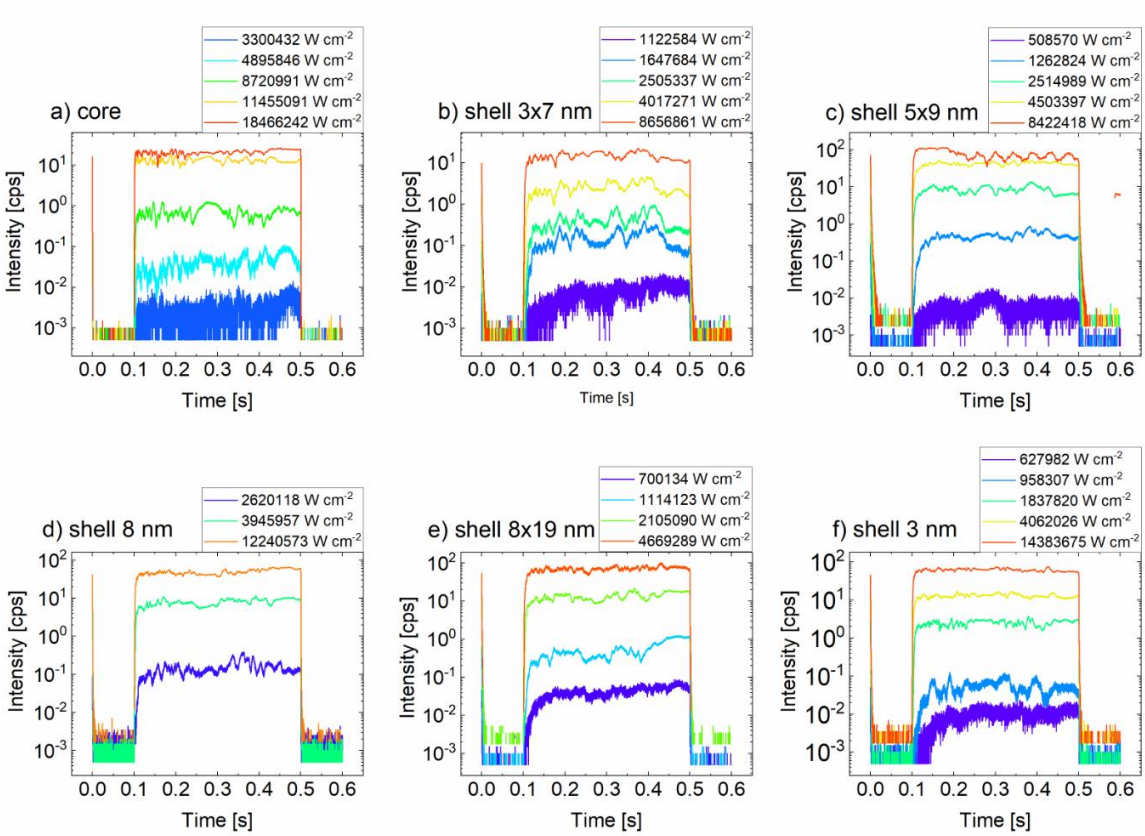

Figure 53. Rise and decay times for different excitation laser powers under the excitation 1059 nm.

Another series of nanocrystals with different shell thickness doped with 2% Tm^{3+} and 48% Yb^{3+} were synthesized by dr. Katarzyna Prorok. The Table 5 shows the size of nanoparticles and shell thickness with the ratio of shell volume to nanocrystal volume. TEM images, as depicted in *Figure 54*, along with X-ray diffraction patterns presented in *Figure 55*, serve as compelling evidence affirming the purity morphology and structural integrity of the nanocrystals under investigation. The TEM images not only provided visual insights but also facilitated the precise determination of the nanocrystals' average size.

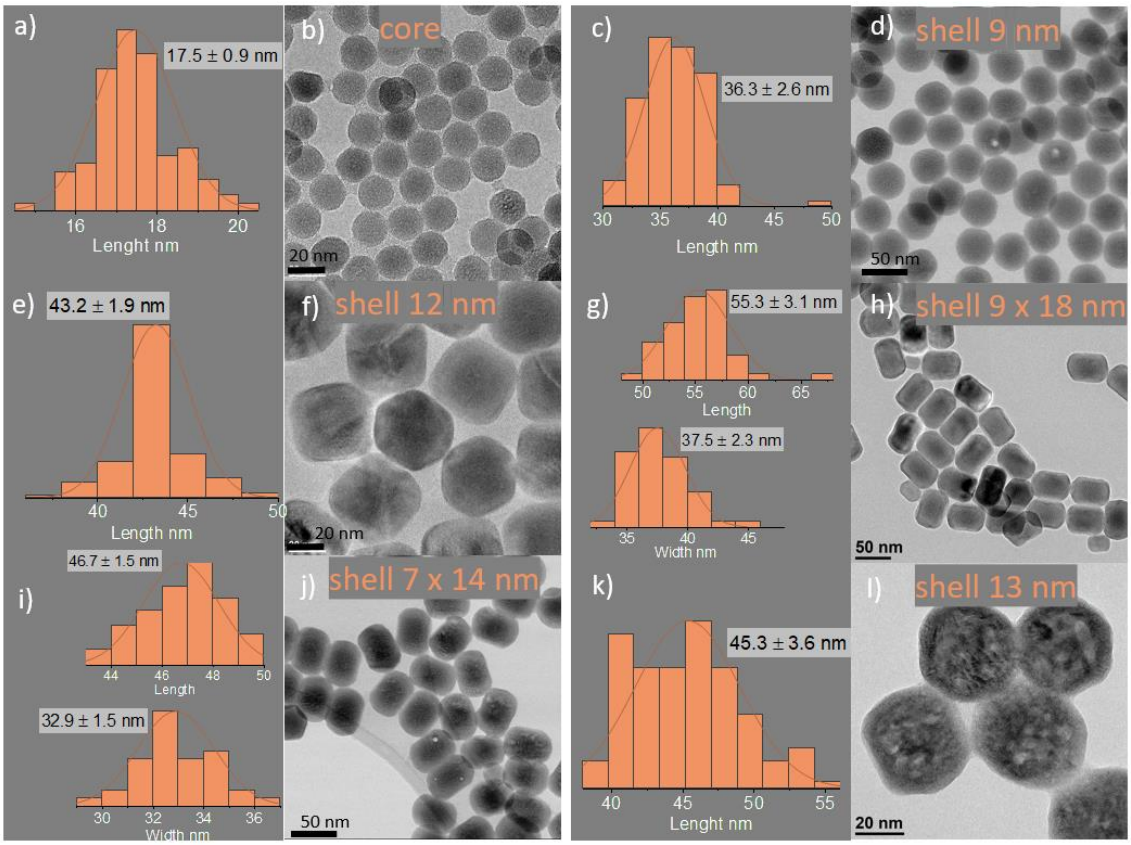

Figure 54. TEM images of $NaYF_4$ b) core, d) core with shell thickness 9 nm f) core with shell thickness 12 nm h) core with shell thickness 9 x 18 nm j) core with shell thickness 7 x 14 nm l) core with shell thickness 13 nm. Histograms with distributions of a) core c) shell 9 nm e) shell 12 nm g)shell 9 x 18 nm i)shell 7 x 14 nm k) shell 13 nm.

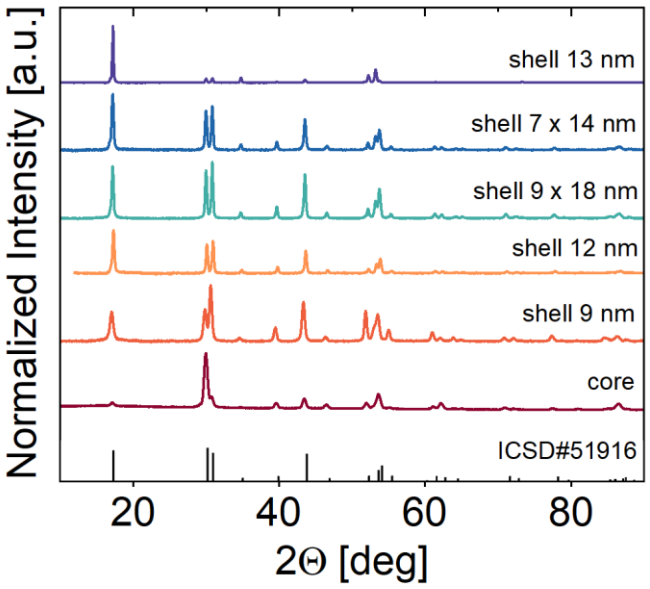

Figure 55. Powder X-ray diffraction data of the synthesized $NaYF_4$ nanocrystals doped with 8% Tm^{3+} with varying shell thickness are presented.

Table 5. Table comparing nanoparticle sizes, shell thickness and the ratio volume of the shell to the volume of the nanoparticle.

sample	Size NPs [nm]	Shell thickness [nm]	Ratio volume shell/ volume NPs
Core $NaYF_4$:2%Tm^{3+}48%Yb^{3+}	18	0	-
Core-shell $NaYF_4$:2%Tm^{3+}48%Yb^{3+}@ $NaYF_4$	36	9	0.72
Core-shell $NaYF_4$:2%Tm^{3+}48%Yb^{3+}@ $NaYF_4$	43	12	0.80
Core-shell $NaYF_4$:2%Tm^{3+}48%Yb^{3+}@ $NaYF_4$	38x55	9x18	0.99
Core-shell $NaYF_4$:2%Tm^{3+}48%Yb^{3+}@ $NaYF_4$	33x47	7x14	0.99
Core-shell $NaYF_4$:2%Tm^{3+}48%Yb^{3+}@ $NaYF_4$	45	13	0.82

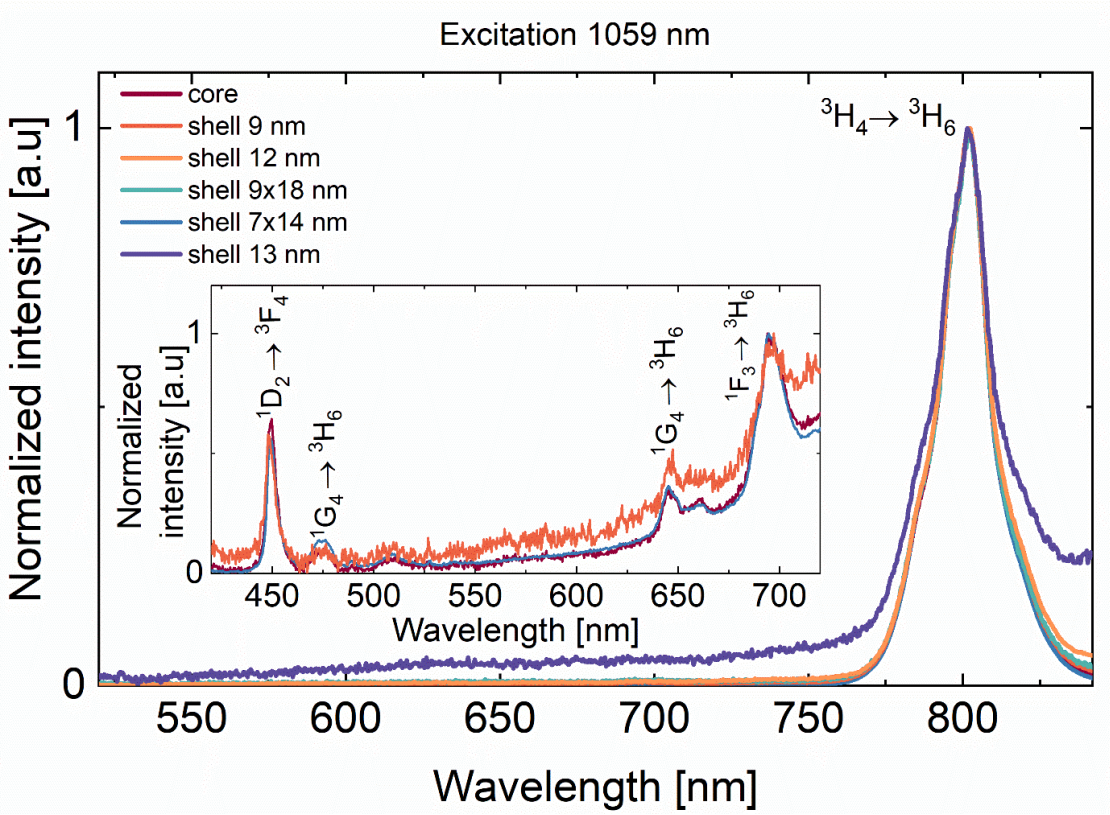

Figure 56. Emission spectrum under the excitation of 1059 nm of $NaYF_4$: 2%Tm^{3+} 48%Yb^{3+} @$NaYF_4$ with various shell thickness: 9 nm, 12 nm, 9x18 nm, 7x14 nm, 13 nm and core with signed energy transitions.

I conducted spectral measurements for each sample (*Figure 56*). A pronounced emission at 800 nm was observed, originating from the energy transition between the $^3H_4$ and $^3H_6$ levels. Subsequently, I measured spectra within the visible light range, with particular attention to the 450 nm emission associated with the $^1D_2 \rightarrow {}^3F_4$ energy transition. To further investigate, I assessed the pump power dependence for this both emission bands.

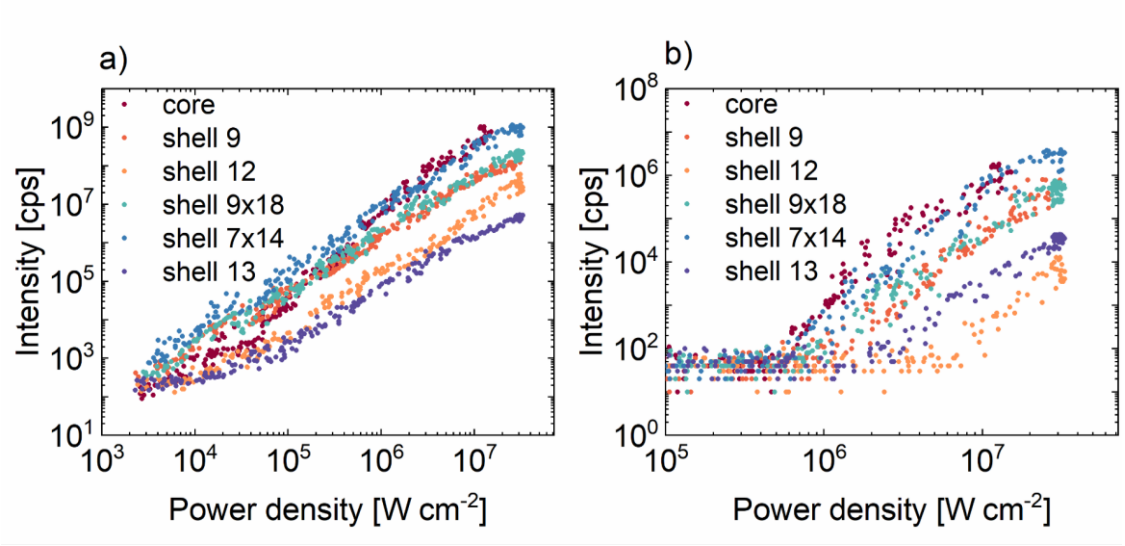

Figure 57. Dependence of luminescence intensity on the power density of the excitation laser for different shell thickness in $NaYF_4$ nanocrystals doped with 2% Tm^{3+} and 48% Yb^{3+}. a) emission at 800 nm and b) emission at 450 nm.

For these nanocrystals, no PA was achieved. The luminescence intensity plotted against the laser power density did not exhibit characteristic S-shaped curves (*Figure 57*).

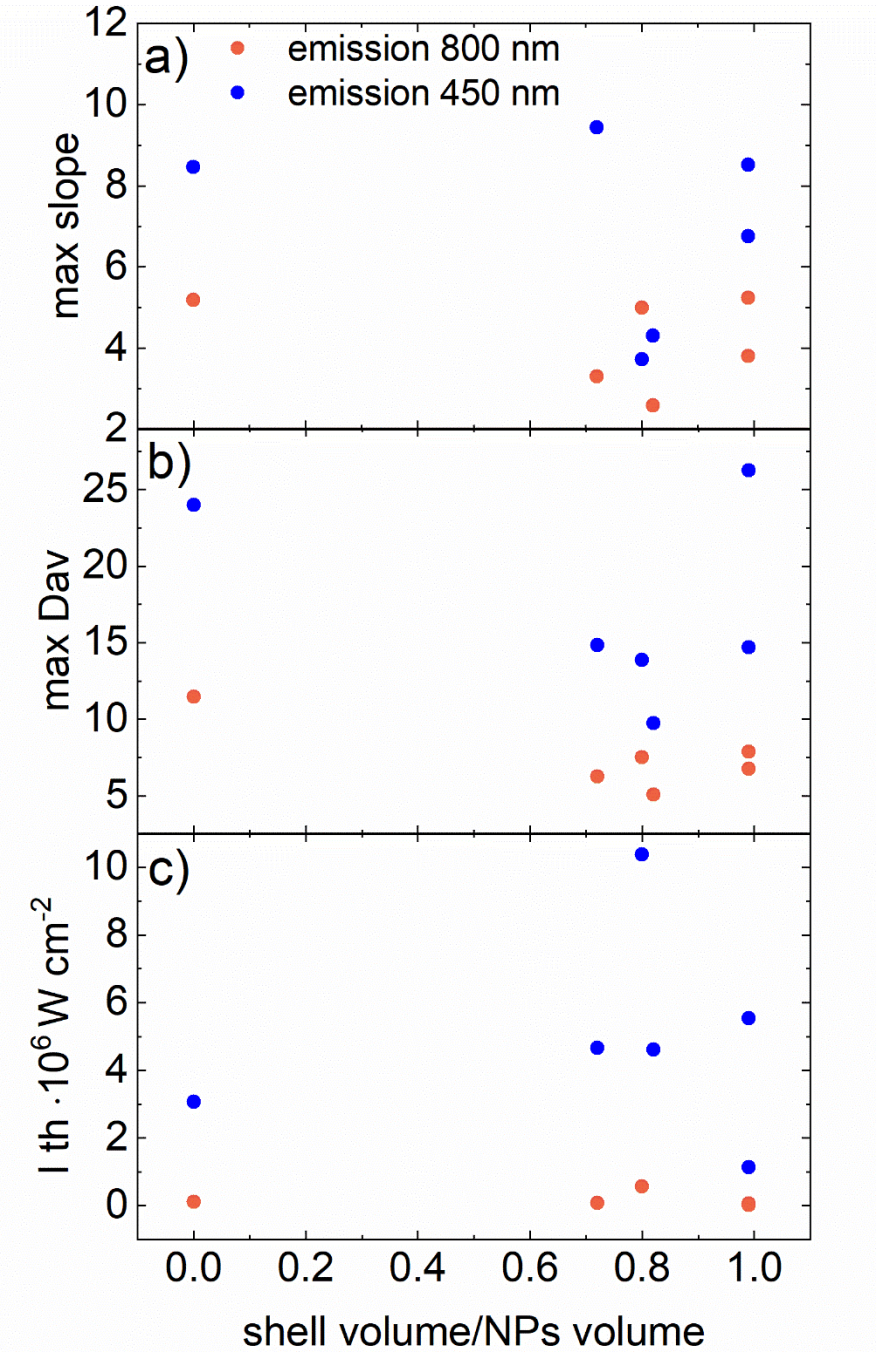

Figure 58. PA parameters, red for emission at 800 nm, blue for emission at 450 nm a) max slope; b) max D_{av} ; c) PA threshold.

The kinetics were then measured for different excitation laser powers (*Figure 59*).

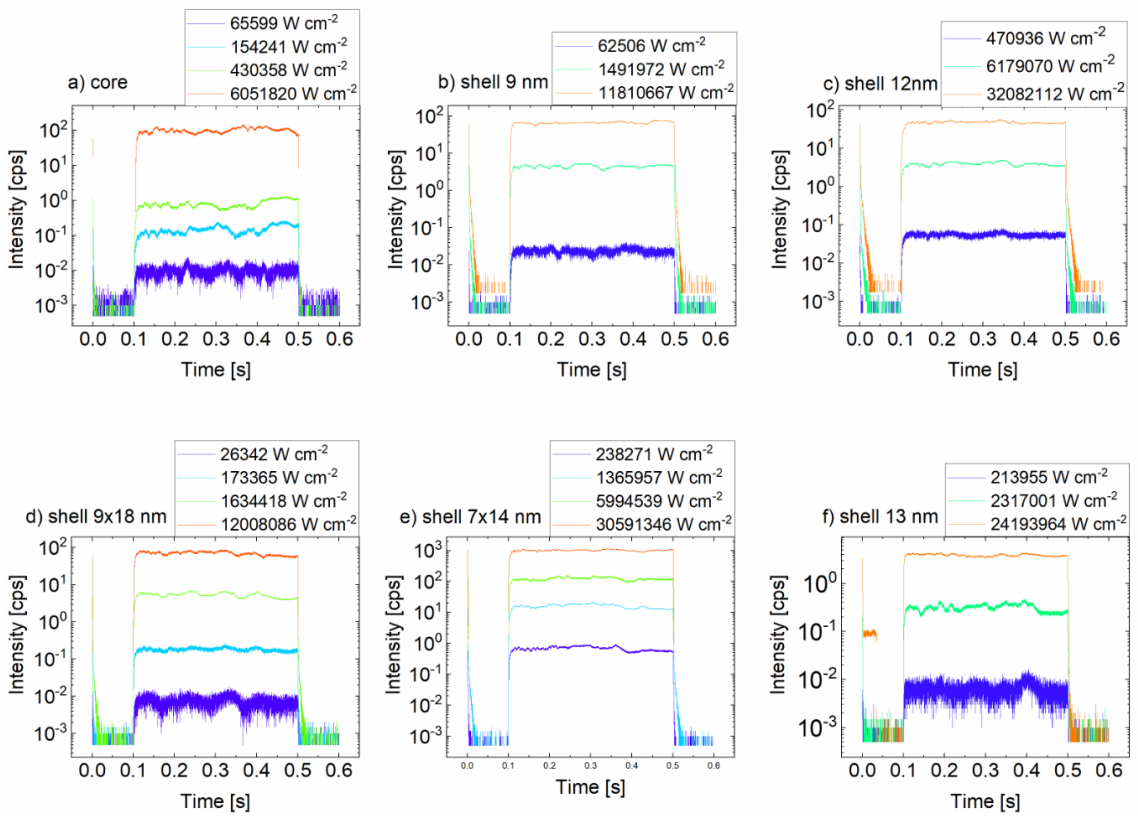

Figure 59. Rise and decay times for different excitation laser powers under the excitation 1059 nm.

Conclusions

The above studies confirm that the passive shell protects nanocrystals and enhances PA emission. The shape of the shell also plays a role in its selection.

Yb facilitates 1059 nm excitation beam absorption and support Tm ions to upconvert instead of energy looping or photon avalanching. Another reason no PA is observed is low 2%Tm doping, which limit energy looping. It is challenging to compare shells with elongated shapes. In the case of spherical shells, there is a clear dependency where a thicker shell corresponds to a lower PA threshold at smaller laser powers.

6.1.7. Impact of the host matrix on the PA

To achieve effective upconversion luminescence, the choice of the host crystal matrix holds utmost importance. The host crystal dictates several critical factors: the spacing between doping lanthanide ions, their spatial orientation, coordination numbers, and the type of surrounding anions. Additionally, the host materials induce crystal fields that perturb the 4f wavefunction, facilitating f-f electronic transitions within the lanthanide ions. Consequently, any alterations in the crystal structure of the host materials significantly impact the optical characteristics of nanomaterials. These crystallographic properties affect energy level splitting and the exact position of ESA band, which, following the ratio of ESA to GSA absorption cross sections, determine the preliminary condition to achieve PA emission.

A pivotal characteristic for assessing the host lattice is the optimal, typically low, phonon energy, which correlates with lattice vibrations in crystals. The absence of high-energy phonons limits undesired nonradiative multiphonon relaxation processes, thereby maximizing radiative emission. Conversely, in certain systems, the presence of phonons in the host matrix can positively affect upconversion efficiency. This is because excited states can be populated through phonon-assisted energy transfer due to energy disparities. In such cases, a higher phonon energy eases the population of lanthanide ion excited states, emphasizing the importance of striking a suitable balance among phonon modes within the crystal lattice.

Numerous materials have been investigated as matrices for upconversion process between lanthanide ions, encompassing phosphates [93], vanadates [94][95], sulfides [96], borates [97][98][99], oxides [100], and fluorides. Among the various material types, fluorides like ALnFx (where A represents alkali metals and Ln denotes lanthanides), including NaLnF4, KLnF4, LnF_3, CaF_2, and $KMnF_3$, emerge as favored candidates for hosting the upconversion process. Their distinguishing characteristics comprise low phonon energies, robust chemical stability, and excellent optical transparency across a broad range of wavelengths, positioning them as preferred materials for facilitating upconversion. Furthermore, host lattices based on cations like Na^+, Ca^{2+}, and Y^{3+} with ionic radii closely matched to those of lanthanide dopant ions serve to inhibit crystal defect formation.

Within the realm of fluorides, hexagonally structured sodium yttrium fluoride (β-$NaYF_4$) is acclaimed as an exceptionally efficient host material for upconversion, primarily due to its exceedingly low phonon energy characteristic (approximately 350 cm^{-1}). The crystal structure of the hexagonal phase $NaYF_4$ boasts an organized array of F- ions and two distinct, relatively low-symmetry cation sites selectively occupied by Na^+ and RE^{3+} ions. This arrangement multiplies the potential energy transfer pathways, consequently augmenting the upconversion process's efficiency. A multitude of studies have confirmed that the hexagonal phase $NaYF_4$ outperforms the cubic structure as a host lattice for upconversion emissions. For instance, the upconversion efficiency of green emission in hexagonal-phase $NaYF_4$:Yb^{3+}/Er^{3+} is roughly tenfold stronger than that observed in cubic $NaYF_4$:Yb^{3+}/Er^{3+}.

CaF_2 serves as a host lattice known for its remarkable attributes: high thermal and chemical stability, a broad transmission range, and a notably low phonon energy at 328 cm^{-1}. Nevertheless, incorporating trivalent lanthanide ions into the divalent alkaline earth fluoride MF_2 (where M=Ca, Sr, Ba) poses the risk of creating crystal defects and lattice stress due to the charge disparity between these ions [101]. Among these, only lanthanum fluoride (LaF_3) stands out prominent low phonon energy modes. These modes, positioned at 227 and 390 cm^{-1}, are advantageous for mitigating multiphonon quenching of upconversion emissions. Other heavy halides like chlorides, iodides, and bromides exhibit phonon energies less than 300 cm^{-1}. However, their utility is limited due to their lower chemical stability and hygroscopic nature.

Another class of materials used as upconversion lattices comprises oxides, such as Y_2O_3, Gd_2O_3, and Lu_2O_3. Oxide particles offer stability over a wide temperature range and exhibit commendable chemical stability. Moreover, they can be doped with various lanthanide ions because of their relatively modest differences in atomic radius and the same charge as Y^{3+} ions. However, these oxides have relatively high phonon energy, exceeding 500 cm^{-1}, attributable to the host lattice's stretching vibration. An illustrative example showcases the emission intensity of α-$NaYF_4$, codoped with Er^{3+} and Yb^{3+}, which was approximately 20 times higher than that in Y_2O_3, codoped with the same ions.

The selection of a host lattice with low phonon energy is pivotal for achieving efficient upconversion. In high-energy phonon hosts, the lifetimes and populations of intermediate states are diminished by multiphonon relaxation, consequently diminishing the effectiveness of upconversion energy processes.

To examine how the matrix affects the PA, dr. Małgorzata Misiak synthesized a series of samples with the same 8% Tm^{3+} ions concentration in different matrices. TEM and XRD (*Figure 60*) measurements confirmed the structural and morphological purity of the obtained nanocrystals.

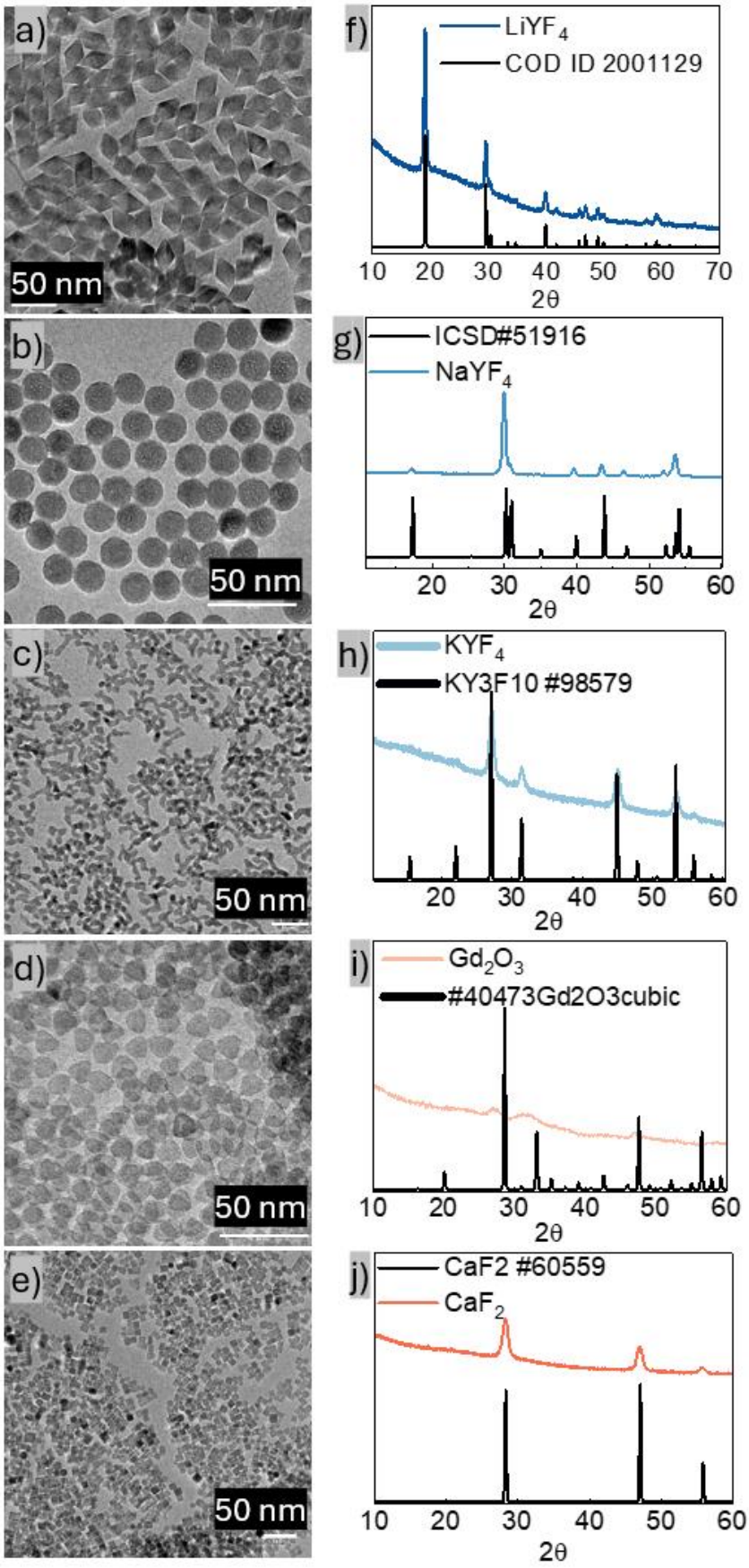

Figure 60. TEM images of various matrices doped with 8% Tm^{3+} and XRD.

Next, for the emission at 800 nm, I measured the dependence of luminescence intensity on the excitation laser power density (1059 nm). The steepest slope of the curve was exhibited by $LiYF_4$ nanocrystals (7.1), followed by $NaYF_4$ (4.7), KYF_4 (2.7), CaF_2 (2.3), and the smallest was observed for Gd_2O_3 (1.8). The smallest PA threshold occurred for CaF_2 crystals, while the largest was for Gd_2O_3. In addition to the matrix and, consequently, the phonon energy impact on PA emission, the shape of the nanocrystal also plays a role. All presented nanocrystals have a core architecture, so they are not protected from surface quenching. In the case of Gd_2O_3 crystals, which are flat, there is a large surface area, and there may be some defects on the surface, disrupting the PA.

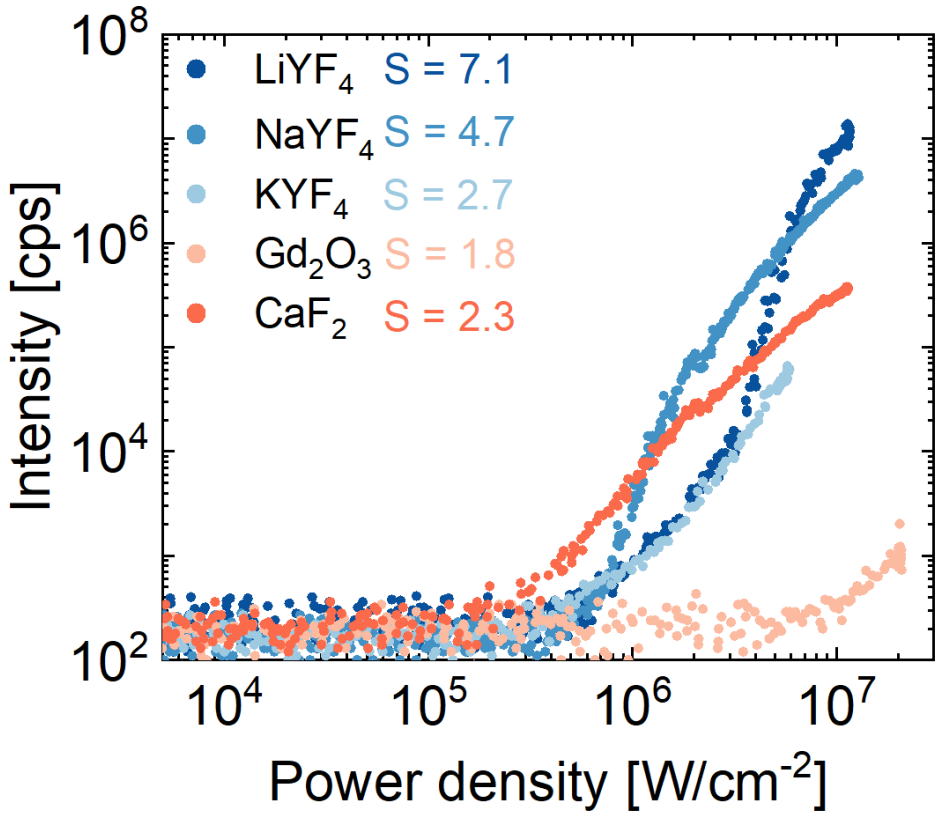

Figure 61. Dependence of luminescence intensity on laser power density for various nanocrystals ($LiYF_4$, $NaYF_4$, KYF_4, Gd_2O_3, CaF_2) doped with 8%Tm.

Conclusions

The occurrence of PA in a crystal, despite the same concentration of Tm ions, is influenced by the type of matrix, phonons, and the shape in which the crystal crystallizes. The crystal surface contributes to increased surface quenching, leading to a significant reduction in emission. In the case of a gadolinium matrix, these are large and flat crystals,

and defects also play a role. Additionally, surface defects are in a disturbed symmetry, transmitting energy to the outside organic environment.

It is not easy to measure ESA spectra, and this is needed to determine exactly for which excitation wavelengths the most favourable ratio σESA/ σGSA is obtained. In addition, the PA emission is affected by the shape of the crystal. Crystals with a flat large surface area show surface extinction. Furthermore, to achieve PA, a delicate balance between energy looping, MPR, and emission is essential.

6.2. Photon avalanche in Pr^{3+} ions

The primary goal of this study was to comprehend the origin and mechanism of PA emission from Praseodymium (Pr^{3+}) ions at the nanoscale. Furthermore, building on earlier reports of MPA [102] in Pr^{3+} ions when co-doped with Ytterbium (Yb^{3+}), we created samples co-doped with 15% Yb^{3+} ions across a broad concentration range of Pr^{3+} ions, namely 0.1%, 0.3%, 0.5%, and 0.7%. All materials were synthesized via the thermal decomposition of lanthanide salts in both core and core-shell architectures.

6.2.1. Investigation of different Pr^{3+} concentrations on PA

β-$NaYF_4$ nanocrystals doped with praseodymium and also co-doped with praseodymium and ytterbium ions were synthesized by Magdalena Dudek. The chosen crystal matrix is well-suited for the PA phenomenon because of its low phonon energy. Furthermore, in comparison to the cubic α-$NaYF_4$ structure, the hexagonal structure is more luminescent. All nanocrystals were fabricated as core NP and these cores were additionally passivated with an undoped shell.

Core:

1. $NaYF_4$:0.1% Pr^{3+} 15% Yb^{3+}
2. $NaYF_4$:0.3% Pr^{3+} 15% Yb^{3+}
3. $NaYF_4$:0.5% Pr^{3+} 15% Yb^{3+}
4. $NaYF_4$:0.7% Pr^{3+} 15% Yb^{3+}

Core-shell:

1. $NaYF_4$:0.1% Pr^{3+} 15% Yb^{3+} @$NaYF_4$
2. $NaYF_4$:0.3% Pr^{3+} 15% Yb^{3+} @$NaYF_4$
3. $NaYF_4$:0.5% Pr^{3+} 15% Yb^{3+} @$NaYF_4$
4. $NaYF_4$:0.7% Pr^{3+} 15% Yb^{3+} @$NaYF_4$

Morphological characterization was conducted for all the prepared nanocrystals, as depicted in *Figure 62*. X-ray powder diffraction (XRD) patterns of the investigated samples closely matched the XRD pattern of the hexagonal structure of $NaYF_4$ crystal (*Figure 62 i*)) confirming the synthesis of all materials in the pure β-NaYF4 phase. The dimensions of these nanocrystals were estimated based on transmission electron microscopy (TEM) images. Exemplary TEM images can be found in *Figure 62*, panels (a-h). Core nanoparticle diameters fell within the range of 17-20 nm, while core-shell dimensions spanned 25-31 nm. Most of the crystals exhibited a narrow size distribution. The thicknesses of the shells were calculated based on the average dimensions of the nanocrystals. In most spherical core-shell nanoparticles, the shell thickness measures around 4 nm, with the exception of the 0.5% Pr^{3+} doped ones, where the shell thickness is approximately 2 nm. This finding suggests that in this sample, a portion of the shell material crystallized as smaller, undoped β-$NaYF_4$ particles.

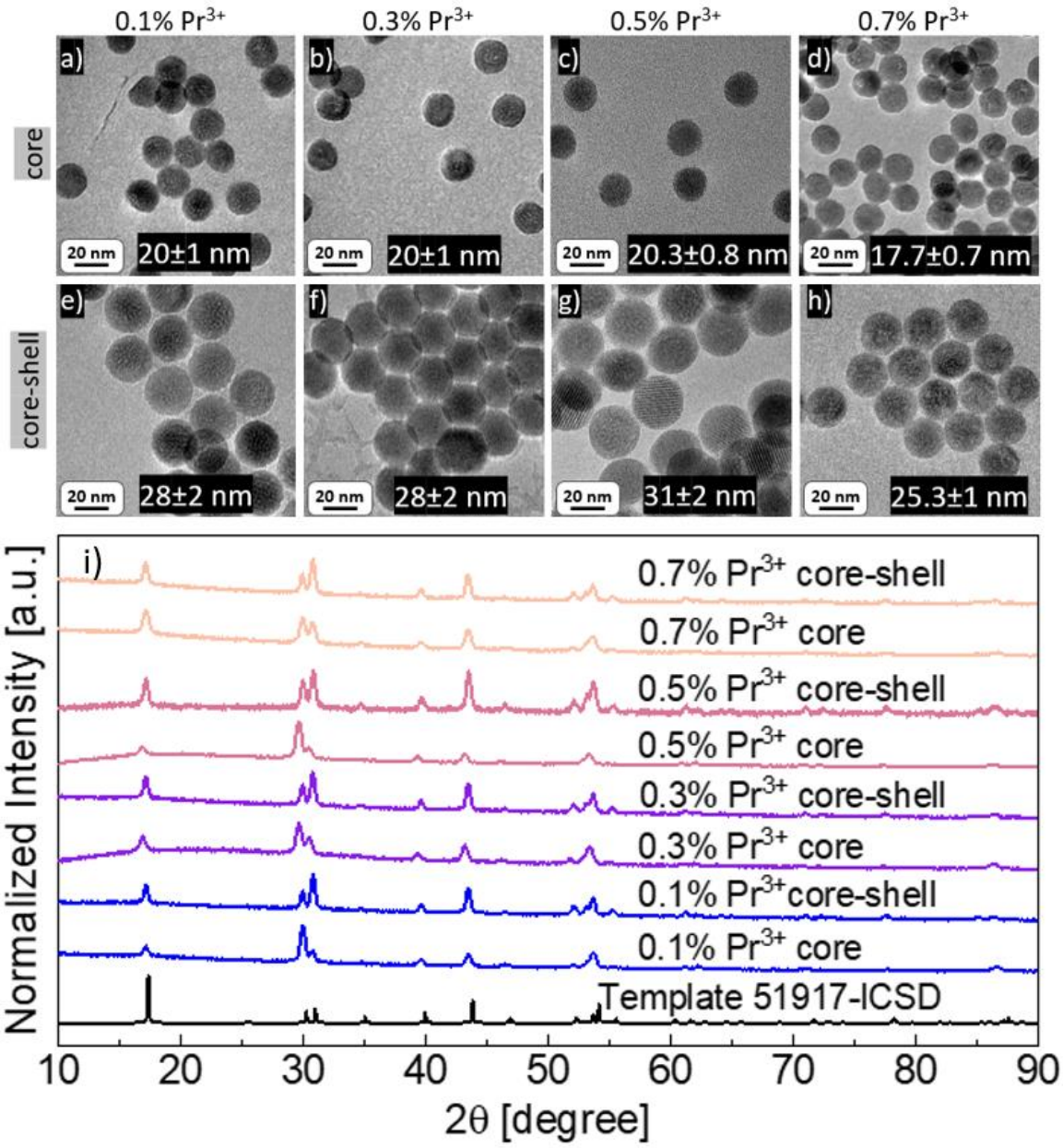

Figure 62. Distinctive features of β-$NaYF_4$ nanocrystals co - doped with x% praseodymium (Pr^{3+}) and 15% ytterbium (Yb^{3+}) ions exhibiting photon avalanche: (a - d) Transmission Electron Microscopy (TEM) images of core nanoparticles. (e-h) TEM micrographs of core-shell nanocrystals.i) X-Ray powder diffraction patterns, showcasing the β-$NaYF_4$ structure (as a reference) and those of all the samples.

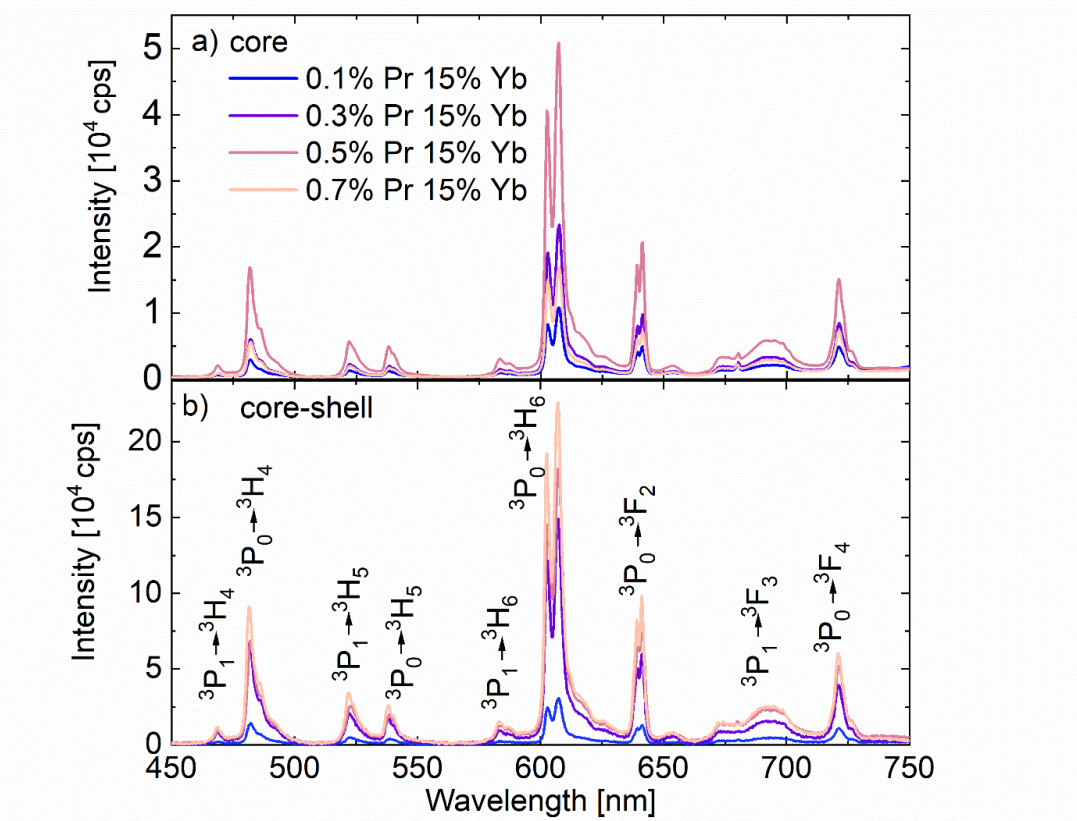

Figure 63. Emission spectrum under the excitation of 852 nm of $NaYF_4$: x%Pr^{3+} 15%Yb^{3+} with signed energy transitions.

In order to verify the presence of the PA phenomenon, we employed an excitation wavelength of 852 nm. This wavelength is in resonance with the ESA of Praseodymium (Pr^{3+}) ions ($^1G_4 \rightarrow {}^3P_1$) while simultaneously staying significantly distant from the Ground-State Absorption (GSA) of these ions, as required for PA. These measurements were conducted at room temperature (RT). We focused our investigation on nanocrystals that were co-doped with both Pr^{3+} and Ytterbium (Yb^{3+}). The 852 nm wavelength can excite Yb^{3+} ions, enabling subsequent Energy Transfer (ET) to Pr^{3+} ions. This process was observed in both core and core-shell samples co-doped with 15% Yb^{3+} ions and a minor concentration, specifically 0.1%, 0.3%, 0.5%, and 0.7% of Pr^{3+} ions. The results revealed multicolor emissions spanning the range from 450 nm to 700 nm (*Figure 63*). Yb^{3+} ions played a pivotal role as sensitizers, contributing further to the sensitized photon avalanche (SPA) phenomenon. These two (607 nm and 482 nm) intense emissions were selected for measuring emission intensity as a function of pump power density.

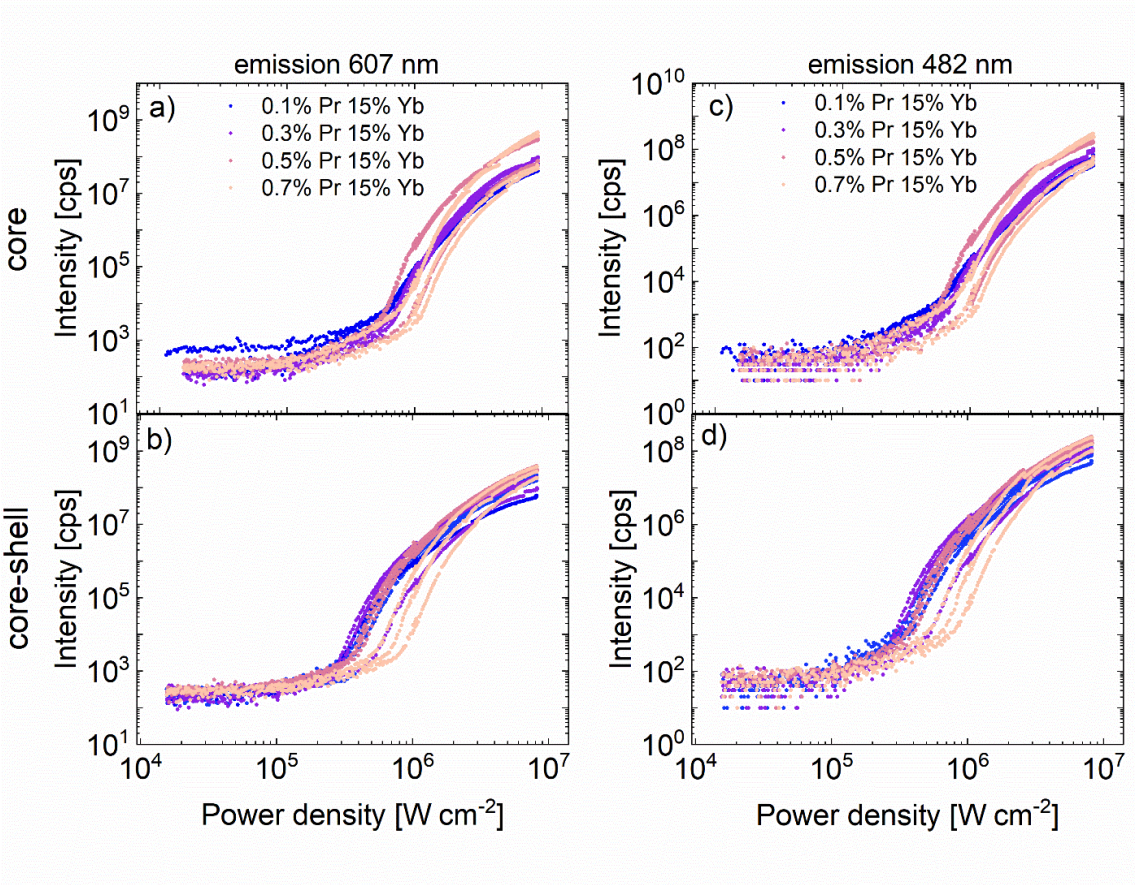

Figure 64. Dependence of luminescence intensity on the power density of the excitation laser 852 nm for various concentration (0.1%; 0.3%; 0.5%; 0.7%) of Pr^{3+} in $NaYF_4$ nanocrystals. a) luminescence intensity at 607 nm in core architecture of nanocrystals b) luminescence intensity at 482 nm in core architecture of nanocrystals c) spectra of core d) luminescence intensity at 607 nm in core-shell architecture of nanocrystals e) luminescence intensity at 482 nm in core-shell architecture of nanocrystals f) spectra of core-shell.

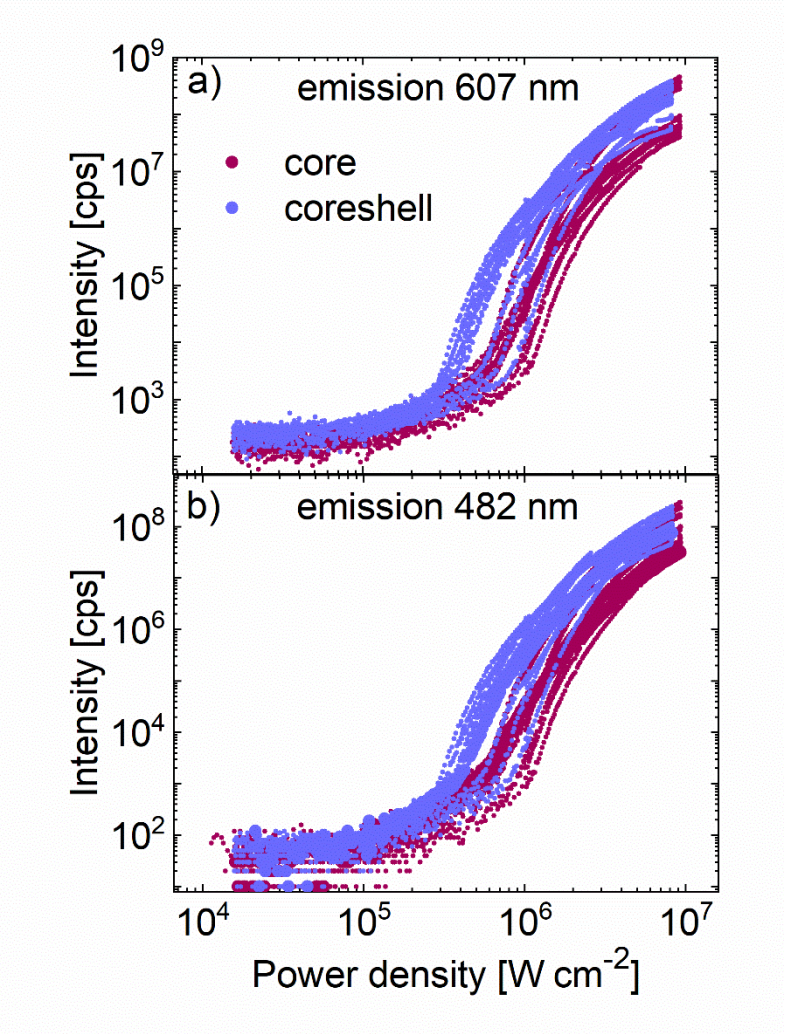

Figure 65. Comparison of dependence of luminescence intensity on the power density of the excitation laser 852 nm for core and core-shell nanocrystals a) emission at 607 nm b) emission at 482 nm.

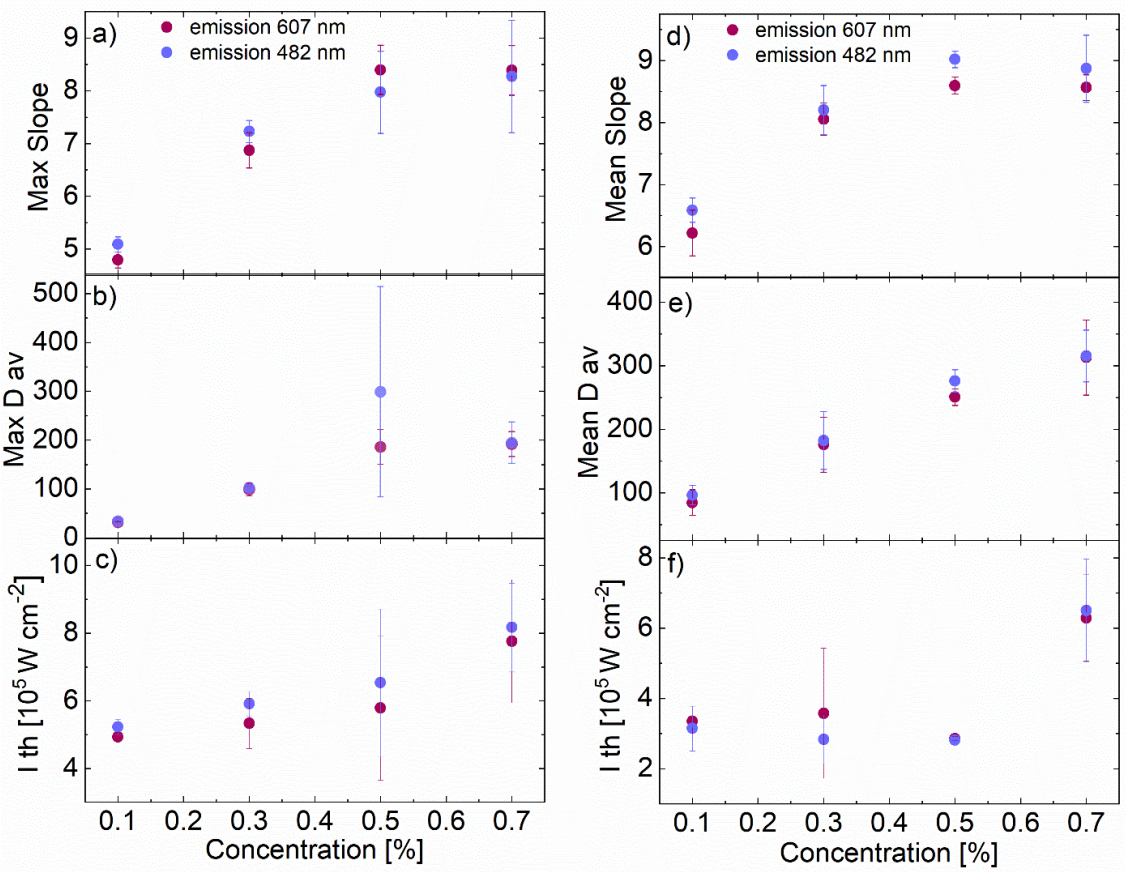

Figure 66. Parameters describing avalanche photon emission. a), b) and c) concerns cores nanoparticles and d), e) and f) concerns core-shells nanoparticles.

As a result, characteristic S-shaped curves were obtained (*Figure 65*). The pump power dependence was measured at least twice, and the average maximum S and average PA_{TH} were calculated (*Figure 66*). When comparing core samples with their core-shell counterparts, it is evident that slope values (*Figure 66* are higher for core-shell samples, and thresholds are lower for them. Once again, the inert shell plays a crucial role in protecting the optically active core from adverse impact of environment. Analyzing *Figure 64* and *Figure 66* it can be observed that average slope values increase with the amount of Pr^{3+} ions, up to 0.5%, and then decrease slightly for 0.7% Pr^{3+} ions. For both PA emissions at 482 nm and 607 nm, the highest average slopes were detected for core-shell NaYF4 nanocrystals co-doped with 15% Yb^{3+} and 0.5% Pr^{3+} ions, amounting to 9.02 and 8.60. Regarding thresholds (*Figure 66*), for PA emissions at 482 nm and 607 nm, the smallest PA_{TH} values were observed for core-shell $NaYF_4$: 15% Yb^{3+}, 0.5% Pr^{3+} @ $NaYF_4$ nanocrystals, totaling 281 kW/cm2 and 287 kW/cm^2, respectively. This means that this sample required the lowest power densities to achieve PA. Therefore, core-shell 15% Yb^{3+} and 0.5% Pr^{3+} co-doped $NaYF_4$ nanocrystals were found to be optimal for PA

emission in this set of investigated samples, aligning with earlier research findings (7). D_{AV} values were calculated (*Figure 66*), describing how much luminescence intensity increases after a twofold increase in power density. Core-shell nanocrystals were found to be more sensitive to changes, with the most sensitive sample being $NaYF_4$: 15% Yb^{3+}, 0.7% Pr^{3+} @ $NaYF_4$

Conclusions

Successful SPA emissions at 482 nm ($^3P_0 \rightarrow {}^3H_4$) and 610 nm ($^3P_0 \rightarrow {}^3H_6$) were achieved in $NaYF_4$ colloidal nanocrystals. These nanocrystals were co-doped with 15% Yb^{3+} ions and

a small amount of Pr^{3+} ions under 852 nm excitation. In contrast, no emission was observed from β-$NaYF_4$ nanocrystals doped solely with Pr^{3+} ions under the same experimental conditions. This underscores the crucial role of Yb^{3+} ions in enabling PA emissions under these specific experimental conditions.

Throughout the experimental investigations, the highest values for S were 8.6 and 9.0, and the lowest PA_{TH} values were 286 kW/cm^2 and 281 kW/cm^2, observed for core-shell samples co-doped with 15% Yb^{3+} and 0.5% Pr^{3+} ions for emissions at 610 nm and 480 nm, respectively.

These experimental results shed light on the essential role of Yb^{3+} ions in facilitating PA emissions from Pr^{3+} ions when excited with 852 nm.

6.2.2. Evaluation of temperature on PA in Pr^{3+}

PA emission mechanism suggests that even minor perturbations in the energy loop and energy distribution at the excited levels of lanthanide emitters will have a considerable impact on the luminescence properties. In light of this, the current experiment focused on studying the effect of temperature ranging from -175 to 175 °C, with increments of 25 °C, on the sensitized PA emission in $NaYF_4$ nanoparticles. These nanoparticles were doped with 15% Yb^{3+} ions and 0.5% Pr^{3+} ions (synthesized by Magdalena Dudek) and were pumped at a wavelength of 852 nm. The core nanocrystals were about 20 nm in size, and the core-shell around 31 nm (*Figure 67b)*). Below in *Figure 67c) d) e)* and *f)* images from TEM are shown.

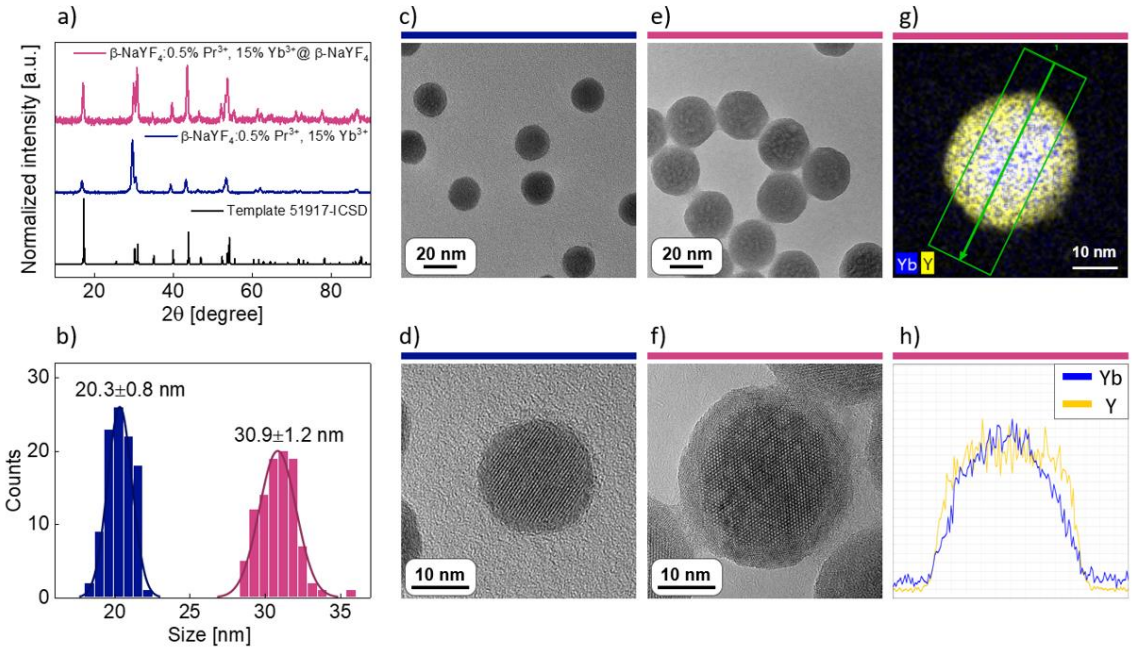

Figure 67. Material properties of core and core-shell nanocrystals $NaYF_4$*:0.5%*Pr^{3+}*15%*Yb^{3+} *a) X-ray powder diffraction patterns for blue - core, pink – core-shell with (black) template b) histograms of size of nanocrystals, blue – core and pink – core-shell. TEM images c), d) core and e), f) core-shell nanocrystals; g) energy dispersive spectroscopy (EDS) mapping of elements and h) EDS line scan profiles of* Yb^{3+} *and* Y^{3+} *ions in a core-shell nanocrystal* [103].

Yb^{3+} ions serve as supportive ions (similar to sensitizers) and play a crucial role in establishing an energy migration network to transfer energy to Pr^{3+} ions. Recently, the phenomenon of SPA in nanocrystalline colloidal nanoparticles has been successfully demonstrated [102]. Moreover, this concept has been further expanded using the core-shell energy migration approach to achieve multicolor PA emission.

The wavelength used in this study is approximately 850 nm, which is resonant with ESA from the $^1G_4$ level in Pr^{3+} ions. Importantly, this wavelength is far from resonance for both Yb^{3+} and Pr^{3+} ions' GSA, as shown in the energy diagram presented schematically in *Figure 68a*).

Although the Yb^{3+} ions absorption from the ground state is weak, it still enhances the population of the $^1G_4$ level of Pr^{3+} ions, leading to the occurrence of ESA. The

combination of this ESA process and appropriately arranged energy levels in Pr^{3+} ions facilitates efficient energy looping, contributing to the generation of PA emission above the pump power threshold.

Despite having a good understanding of this system, limited information is available regarding the susceptibility of PA or SPA emission to temperature in nanoscale materials. This aspect is of great interest in the field of luminescence nanothermometry and its potential applications. Although a single-band radiometric (SBR) approach strategy has been recently proposed, which benefits from the non-GSA excitation scheme and increased cross-relaxation, all current SBR thermometry studies have relied on the sideband ESA [105][91]. To date, no clear evidence of PA behavior has been demonstrated in these studies.

In order to explore their spectroscopic properties, the core-shell nanoparticles were subject to various pump powers within a wide temperature range.

In previous literature reports on various materials, including fluorides, there has been ambiguity in assigning the emission bands in the wavelength range of approximately 580–620 nm to either the $^3P_1$ level or the $^1D_2$ level of Pr^{3+} ions. After careful consideration, we concur with the prevailing opinion that there is no observable $^1D_2$ emission in fluorides. Instead, we oppose that the 583 and 607 nm emission bands originate from the $^3P_1 \rightarrow {}^3H_6$ and $^3P_0 \rightarrow {}^3H_6$ transitions, respectively. These spectral measurements were taken under 852 nm excitation, which aligns perfectly with the excited state absorption of Pr^{3+} ions ($^1G_4 \rightarrow {}^3P_1$). However, this excitation wavelength remains off-resonance to the ground state absorption in both Yb^{3+} ions ($^2F_{7/2} \rightarrow {}^2F_{5/2}$, $\Delta E = 1533\ cm^{-1}$) and Pr^{3+} ions ($^3H_4 \rightarrow {}^1G_4$, $\Delta E = 1887\ cm^{-1}$), as shown in *Figure 68 a)*.

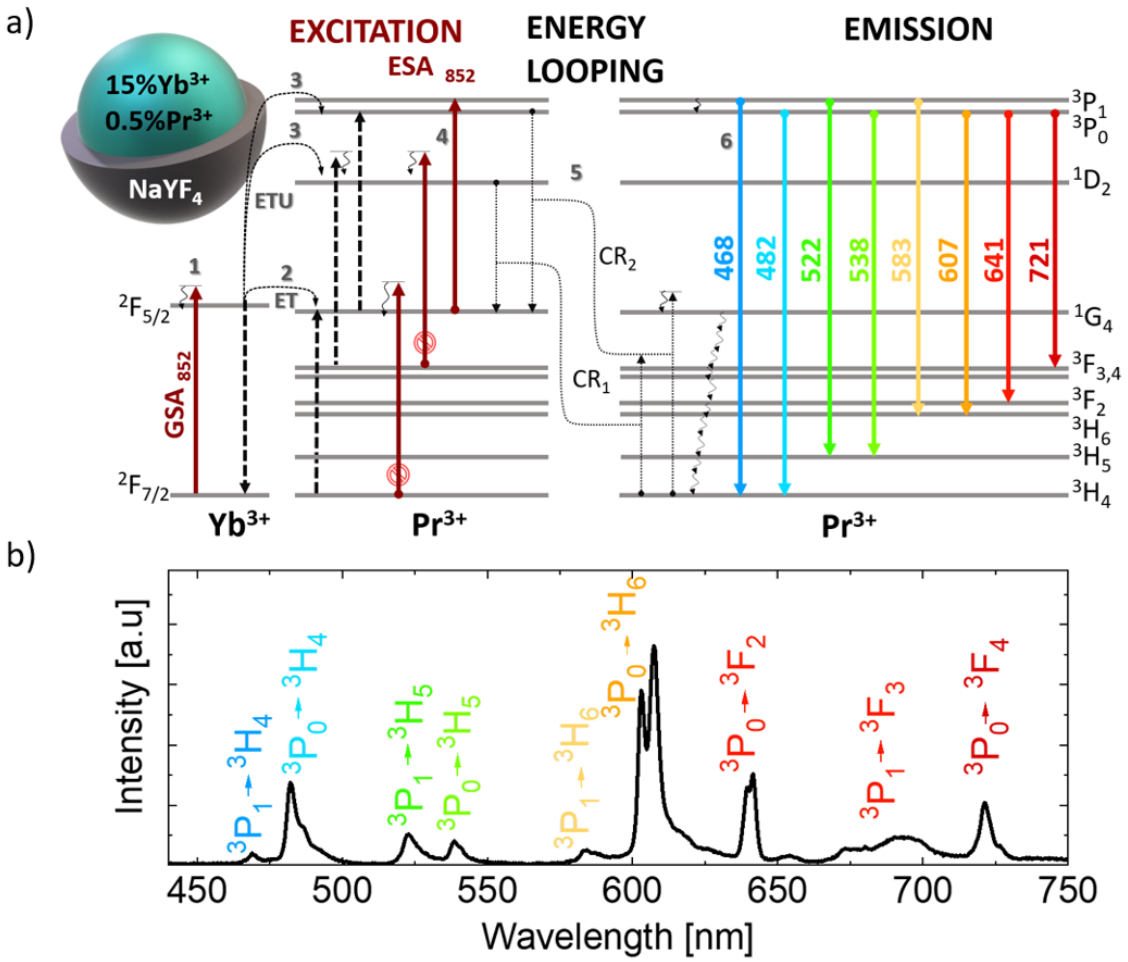

Figure 68. Energy levels in Yb^{3+} and Pr^{3+} and emission spectra from $NaYF_4$: 15%Yb^{3+}0.5%Pr^{3+} [103].

Although there are slight energy mismatches, they are small enough to enable weak sideband, phonon-assisted absorption. This leads to the initial population of key levels of Yb^{3+} ions ($^2F_{7/2} \rightarrow {}^2F_{5/2}$) [process (1)], and subsequently, the Pr^{3+} ions ($^1G_4$) are populated through $Yb^{3+} \rightarrow Pr^{3+}$ energy transfer (ET) [Yb^{3+}:$^2F_{5/2} \rightarrow Pr^{3+}$:$^1G_4$, process (2)] and ETU [$Yb^{3+}$:$^2F_{5/2} \rightarrow Pr^{3+}$:$^1D_2$ or $^3P_0$.1, processes (3)]. Subsequently, energy looping occurs through cross-relaxation, populating the excited state $^1G_4$ [process (5)], which is crucial for PA emission.

Pr^{3+} ions are supposed to be highly susceptible to concentration quenching even at low concentrations of the activators, due to several possible CR mechanisms between their energy levels. Some of these mechanisms also contribute to energy looping, essential for PA. For instance, the CR_2 ($^3P_0$; $^3H_4$) $\rightarrow$ ($^1G_4$; $^1G_4$) $\pm$ 950 cm^{-1} doubles the population of the $^1G_4$ level, supporting ESA excitation, energy looping, and ultimately enhancing PA

behavior. On the other hand, the CR_1 ($^1D_2$; $^3H_4$) → ($^1G_4$; $^3F_{3,4}$) ± 150 cm^{-1} quenches the population of the $^1D_2$ level (if it exists), but it does not contribute to PA gain, as it does not double the population of the $^1G_4$ level (i.e., $^3F3_{,4}$ is fed instead). Consequently, it may result in emission quenching by MPR to the ground state.

The ratio of CR_1 to CR_2 should vary with temperature, as CR_1 requires the occurrence of $^3P_0 \rightarrow {}^1D_2$ ($\Delta E \approx 3850$ cm^{-1}) multi-phonon relaxation, which is approximately 15.4, 12.6, and 10.5 times the energy of the phonons available in the $NaYF_4$ matrix, i.e., 250, 305, and 365 cm^{-1}, respectively. Based on fundamental and more recent studies on MPR, MPR rates are estimated to stay below 320 s^{-1} for the cut-off 365 cm^{-1} phonons at room temperature. Therefore, this CR_1 process is highly unlikely unless ETU from Yb^{3+} occurs. However, since no $^1D_2$ emission is recorded, we deduce that CR_1 is not efficient in the studied system. The only possible CR that may play a role here is the CR_2 process (energy mismatch equals $\Delta E \approx 950$ cm^{-1}), which requires 3 phonons of 305 cm^{-1} energy and thus should be highly probable. As all MPR processes are phonon (defined by host matrix) and temperature-dependent, lower temperatures should further diminish the $^3P_0 \rightarrow {}^1D_2$ MPR and thus support the "beneficial" CR_2 ($\Delta E \approx 150$ cm^{-1}) over the "parasitic" CR_1 ($\Delta E \approx 950$ cm^{-1}).

To understand the role of temperature in PA emission, the intensities of the two most intense emission bands ($^3P_0 \rightarrow {}^3H_4$ at 482 nm and $^3P_0 \rightarrow {}^3H_6$ at 607 nm) were measured while varying the temperature from –175 to 175 °C in 25 °C steps (*Figure 69*). Both profiles were very similar, and the luminescence lifetimes at these wavelengths were identical, approximately 19 μs at room temperature. These measurements further confirm the statement, the $^1D_2$ level does not take place in fluoride matrix, unlike in some existing literature reports [102]. Therefore, the two emission bands originate from the same $^3P_0$ level.

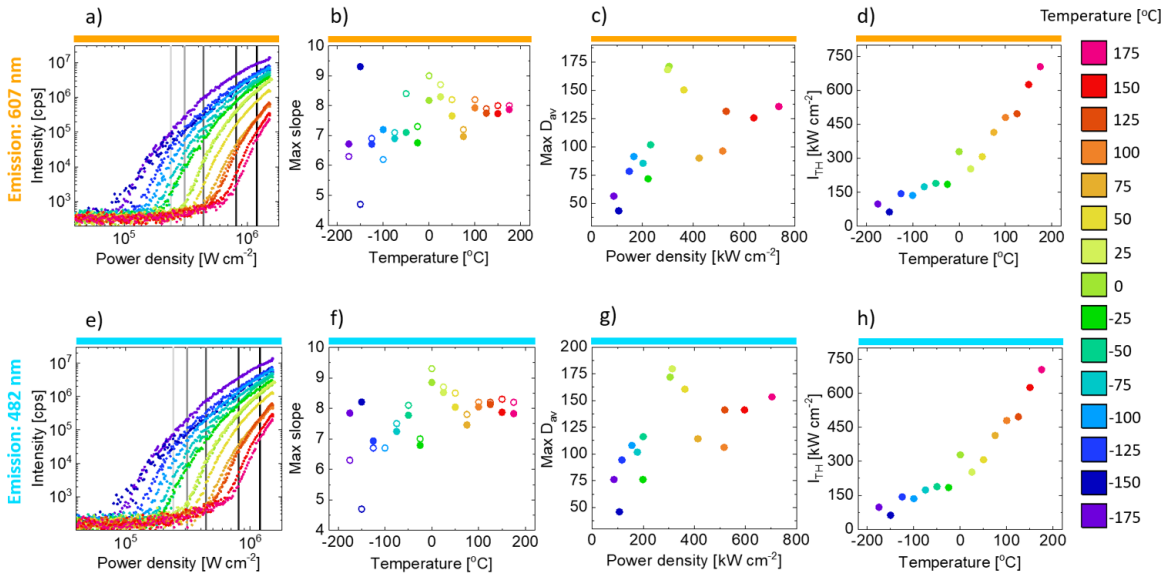

Figure 69. (a) and (e) present pump power dependence of PA emission intensity for different temperatures. (b) and (f) show the maximum PA nonlinearities S_{max} calculated manually (open circles) and by the MATLAB algorithm described in [106]*(full circles)* [103]*;*

Studies of the dependence of luminescence as a function of pump power, shown in *Figure 69 a)* and *e)* at 607 nm and 482 nm, respectively, clearly exhibit typical PA behavior across the entire studied temperature range. Beyond a distinct pump power threshold (*Figure 69 a)–d)* and *e)–h)*), the luminescence intensity experiences a steep increase (*Figure 69* a), b), and e), f)), followed by saturation with further increases in pump power. The slopes of the curves (*Figure 69 b)* and *f)*) measured at different temperatures varied between approximately 6 and 9.3, with most cases yielding values from 7 to 8. The PA gain (D_{av}), which represents the increase in luminescence intensity (I_{lum}) when the excitation beam intensity (I_{exc}) is doubled. The highest D_{av} (*Figure 69c)* and *g)*) was achieved at 482 nm emission at 25°C, reaching a value of 179.6. The high values of S_{max} and D_{av}, and the clear existence of a pump power PA threshold, all firmly support the PA character of the observed emission.

Temperature studies further reveal the significant influence of temperature on the PA phenomenon. As the temperature decreases from 175°C down to -175°C, the PA emission intensity significantly increases by 2–3 orders of magnitude (*Figure 69 a)* and *e)*). This temperature reduction also leads to a decrease in nonlinearity by up to 2-fold (*Figure 69b)*

and f)), and lowers PA gain by approximately 3–4-fold [*Figure 69* c) and g)]. Simultaneously, the PA threshold becomes 10-fold lower [*Figure 69* d) and h)].

The luminescence behavior at low temperatures resembles energy looping rather than true PA (lower slopes and gains). In contrast, at higher temperatures, the emission power dependence shows more typical PA behavior (i.e., higher slopes). These observations suggest a complex nature of the sensitized PA phenomenon in Yb^{3+}, Pr^{3+} co-doped $NaYF_4$ nanoparticles.

On one hand, lowering the temperature reduces multiphonon relaxation, internal losses, and non-radiative quenching on the surface. This is evidenced by the lower PA threshold of pump power. Surface quenching is effectively reduced by surface passivation. However, the losses include efficient cross-relaxations between Pr^{3+} ions and fast MPR processes between levels below 10 000 cm^{-1} ($^1G_4 \rightarrow {}^3F_{3,4} \rightarrow {}^3F_2 \rightarrow {}^3H_6 \rightarrow {}^3H_5 \rightarrow {}^3H_4$). On the other hand, however, the mismatch of energy gaps between the energy levels of Yb^{3+} and Pr^{3+} ions require absorption of host phonons, making lower temperatures an obstacle for efficient energy looping between the two ions. This may seem contradictory to expectations, as the dominance of CR_2 over possible CR_1 should enhance PA performance. However, one must consider the intricate sequence of processes that lead to sensitized PA emission. Absorption, which is strongly temperature-dependent in Yb^{3+} in the fluoride matrix, affects not only process (1) in *Figure 68 a)* but also the ET between Yb^{3+} and Pr^{3+} - processes (2) and (3) in Fig. (a). Additionally, the rich energy level diagram of Pr^{3+} ions likely involves more CR processes than just the most probable CR_2 and CR_1 showed in Fig. a). These additional CRs may further complicate the understanding of the temperature-dependent phenomena studied here.

Lowering the temperature leads to several effects: approximately 100-fold enhanced luminescence intensity, reduction of PA nonlinearities, lowering of PA gains and a decrease in the PA threshold. The increase in PA intensity and decrease in PA threshold are a direct consequence of reduced MPR quenching of emitting and intermediate levels of Pr^{3+} activators, which disrupt energy looping. However, the lower PA slopes [*Figure 69 b)* and *f)*] and PA gains [*Figure 69c)* and *g)*] suggest that CR_2 is affected by temperature to a larger extent than CR_1.

It is important to note that CR_2 plays a critical role in achieving PA emission in Pr^{3+} ions, whereas CR_1 must be considered a parasitic mechanism. Furthermore, the energy

mismatch in ΔE (CR_2) is larger (and therefore more dependent on temperature and host matrix) than ΔE (CR_1), making the CR_2 energy looping more temperature-dependent. As a result, we can conclude that the PA emission in sensitized Pr^{3+} ions is the outcome of an intricate interplay involving several process, namely direct (ESA) and sensitized (Yb^{3+} → Pr^{3+}) photoexcitation, MPR quenching mechanisms and phonon-assisted energy looping. The interplay of these processes, along with their dependence on temperature and host matrix properties, contributes to the intricate behavior of the observed PA phenomenon.

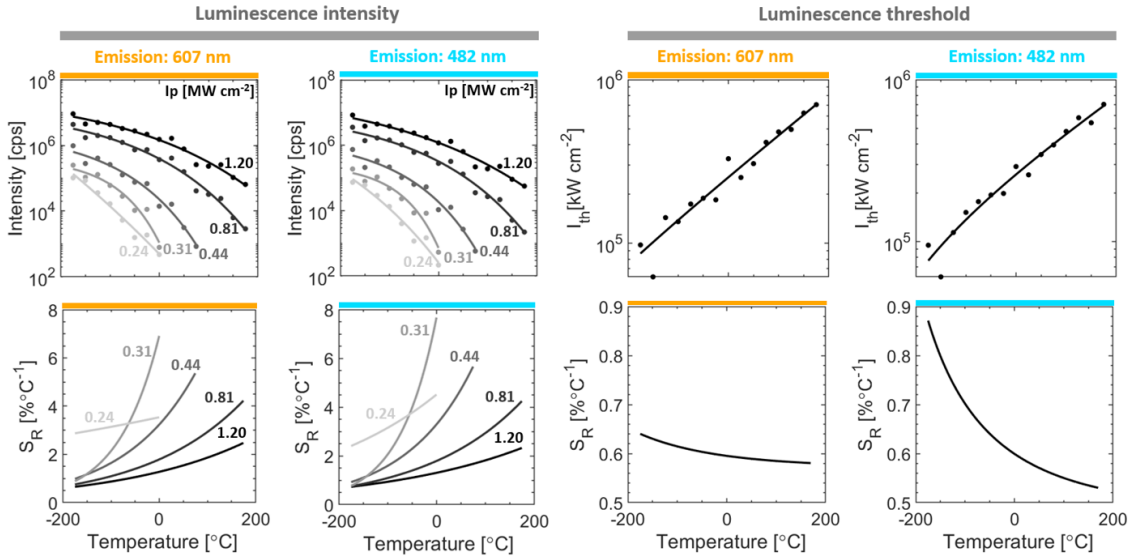

Figure 70. Temperature dependence of PA luminescence intensity, Ith (T), at (a) 607 nm and (c) 482 nm for selected pump power intensities (IP = 0.24, 0.31, 0.44, 0.81, and 1.20 MW·cm-2); (b) and (d) show the corresponding relative temperature sensitivities. Temperature dependence of the PA threshold, Ith (T), for emission at (e) 607 nm and (g) 482 nm. (f) and (h) show the respective relative temperature sensitivities [103].

To further investigate the temperature dependence of the studied sensitized PA system, we analyzed the PA emission intensity at various rising temperatures for specific pump power densities (indicated by vertical gray lines in *Figure 70 a)* and *e)*, located at 0.24, 0.31, 0.44, 0.81, and 1.20 MW·cm^{-2}). These data points were obtained from the original datasets (*Figure 69a*) and *e)*) and were subsequently used for the analysis in *Figure 70*.

As temperature increased, the luminescence intensity exhibited an exponential decrease. The change in temperature resulted in a remarkable increase in PA intensity by more than 2–3 orders of magnitude. However, due to the highly nonlinear nature of PA emission,

the PA intensity was notably affected most probably by small fluctuations in the excitation laser power and mechanical drift of the optical setup. Consequently, the experimental PA intensities did not exhibit perfect smoothness or monotonic behavior.

To enable a quantitative evaluation of the temperature dependence, the experimental data points were initially fitted with an exponential curve, which served as data to calculate relative sensitivity (S_R):

$$S_R = \frac{1}{\theta} \cdot \frac{\Delta\theta}{\Delta T} \cdot 100\%$$

where θ represents a thermometric parameter, such as e.g. luminescence intensity ($\theta = I_{lum}$) or PA threshold ($\theta = I_{th}$). The Δθ denotes the change in the values of the respective luminescence thermometric parameter corresponding to a temperature change of ΔT.

Depending on the selected excitation power, one can deliberately opt for a higher S_R at the cost of limiting the operating range of the thermometer. Conversely, if a wide operating range is preferred, a lower S_R can be achieved, and vice versa. The most significant S_R of 7.5% $°C^{-1}$ was observed under an excitation power density: 0.31 $MW \cdot cm^{-2}$ for emission at 482 nm and in temperatures below 0 °C. A similar high sensitivity S_R=7.0% $°C^{-1}$ was found for 607 nm emission under the same conditions. These sensitivities are higher than those of (1.29% $°C^{-1}$ for $KLaP_4O_{12}:Pr^{3+}$ [90] and 5% $°C^{-1}$ for $LaF_3:Pr^{3+}$ [89], where a genuine PA phenomenon was not observed despite ESA excitation.

Additionally, relative sensitivities were calculated where the new thermometric parameter was the PA threshold (I_{th}), which was 0.9% $°C^{-1}$ for 482 nm emission in low temperatures. Moreover, the relative sensitivities were consistently no less than 0.5% $°C^{-1}$ for both emission wavelengths over the entire temperature range from -175 to 175 °C. The high relative sensitivity values, can be used for precision luminescence nanothermometry.

Conclusions

Nanocrystals with Yb^{3+} and Pr^{3+} exhibits energy looping, which powers the PA emission by involving ESA-pumped Pr^{3+} ions, supported by the presence of Yb^{3+} sensitizer ions. Throughout the studied temperature range (from –175 to 175°C), we clearly observed the

PA phenomenon with significant temperature dependence in both the emission intensity and the PA threshold.

We introduced a novel thermometric approach for luminescence thermometry, based on utilizing the threshold excitation power to observe PA luminescence (I_{th}) as a thermometric parameter. As the temperature increased, we observed a gradual shift of the PA threshold towards higher excitation power densities, ranging from 100 to 750 $kW \cdot cm^{-2}$. This approach enabled us to achieve a relative temperature sensitivity of above 0.5% $°C^{-1}$.

Furthermore, as the temperature increased, we observed a significant decrease in the emission intensity at 482 and 607 nm, with the intensity reduction reaching up to four orders of magnitude for the selected excitation powers. This notable sensitivity of luminescence to temperature variations is of utmost importance for accurate thermometry applications. By analyzing such substantial changes in the intensity of a single emission band, we calculated the corresponding temperature relative sensitivity, achieving a maximum value of 7.5% $°C^{-1}$ at 0 °C. These findings not only confirm the suitability of our approach for luminescence thermometry but also provide compelling evidence of a complex interplay of coexisting phenomena driving the PA emission.

The presented results clearly demonstrate that PA emission in sensitized Pr^{3+} ions is the result of a delicate balance involving various factors, such as direct - ESA and sensitized ($Yb^{3+} \rightarrow Pr^{3+}$) photo-excitations, temperature-dependent phonon-assisted energy looping, and MPR quenching mechanisms. Understanding these mechanisms is crucial for harnessing the full potential of this thermometric system and advancing its applications in temperature sensing.

6.3.Attempts to find PA in Nd^{3+}

The Nd^{3+} energy diagram (*Figure 72a*) is distinguished by the presence of multiple energy levels that facilitate the CR phenomena, boasting wide energy gaps and a big absorption cross-section for ESA. These unique characteristics make neodymium ions highly promising for PA emission applications. Notably, Nd^{3+} emits in the NIR region, aligning with the 1st and 2nd biological windows for tissues. This property renders it highly suitable

for bioimaging and biodetection purposes. Furthermore, Nd^{3+} exhibits temperature-sensitive luminescence properties, making it suitable for luminescent thermometry as well [7].

To investigate the possibility of achieving PA emission in Nd^{3+} I have measured $NaGdF_4$ core nanocrystals doped with different concentrations of Nd^{3+} (1%, 5%, 12.5%, and 25%), which were next surface passivated with $NaGdF_4$ shells without doped [19]. The samples were synthesized by Artiom Skripka.

Structural Analysis

The crystalline structure and phase composition of both core-only and core/shell LnNPs were assessed using XRD analysis. CuKα radiation was employed, and the measurements were carried out with a Bruker D8 Advance Diffractometer. The morphology and size distribution of these nanoparticles were examined through TEM utilizing a Philips Tecnai 12 instrument. To determine particle size, ImageJ image analysis software was employed, with a minimum of 200 individual particles analyzed per sample.

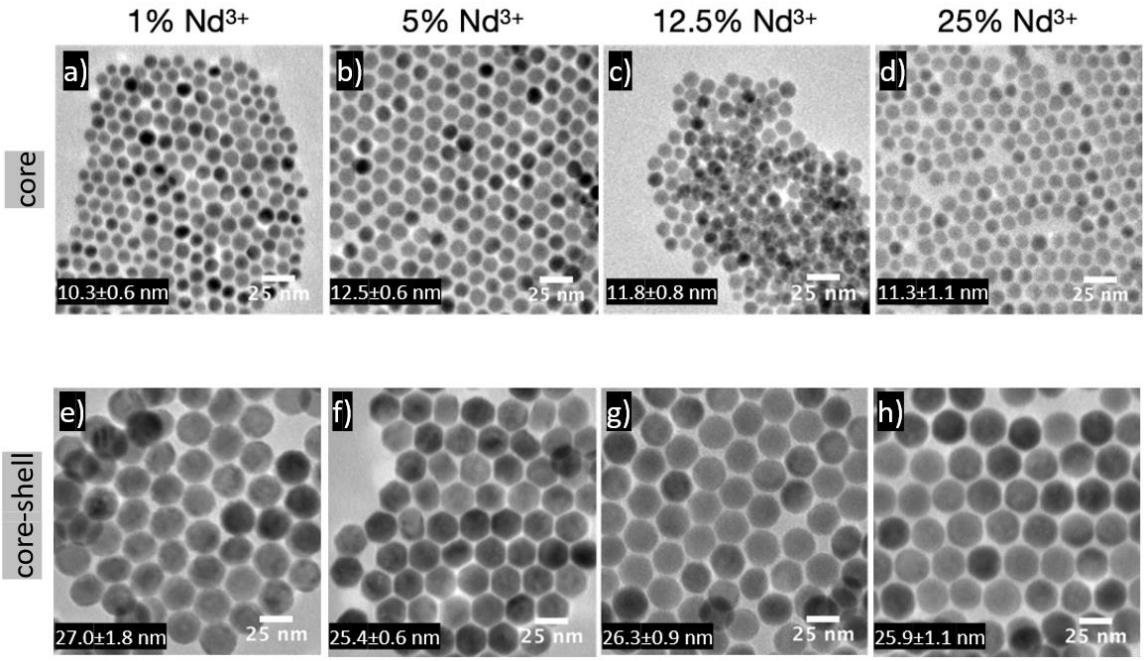

Figure 71. TEM images and size distributions for $NaGdF_4:Nd^{3+}$ core nanoparticles and $NaGdF_4:Nd^{3+}/NaGdF_4$ core-shell nanoparticles.

In our study, we focused on understanding the role of MPR rates, CR and another phonon-assisted energy transfer processes, that are involved in both PA and ESA. These processes influence the population of the $^4I_{11/2}$ level, which is the starting level for PA, and also the emptying of the $^4I_{15/2}$ and $^4I_{13/2}$ levels. We found that these processes can be controlled by temperature. To explore the behavior of the Nd^{3+} system, we conducted measurements in a temperature range from -200 to 200°C.

During the studies, I have measured emission intensity at 880 nm for increasing excitation laser power density at 1059 nm, which induces transitions from the $^4F_{3/2}$ to $^4I_{9/2}$ levels. This excitation wavelength matched well with the ESA process ($^4I_{11/2} \rightarrow {}^4F_{3/2}$), and it was non-resonant with the GSA process ($^4I_{9/2} \rightarrow {}^4F_{3/2}$ - 2000 cm^{-1}) (*Figure 72a*).

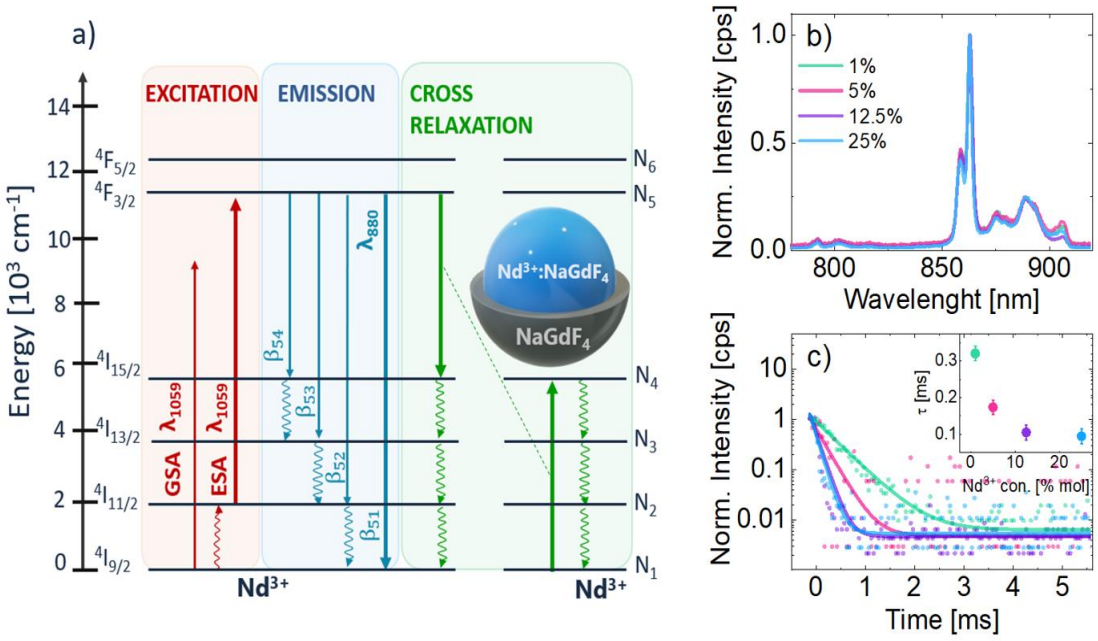

Figure 72. a) Energy diagram in Nd^{3+} and energy transitions occurring: absorption, emission and CR. Nonradiative relaxation is wavy arrows. b) emission spectra. c) decay time with τ for different concentrations of Nd^{3+}.

Anti-Stokes emission spectra and decay times for each sample at an excitation wavelength of 1059 nm were measured. Decay curves were fitted using a single exponential model and single decay constants were calculated (*Figure 72 c)*. As anticipated, the luminescence decay becomes shorter with increasing concentrations [20], which can be attributed to the effective cross-relaxation occurring between adjacent Nd^{3+} ions.

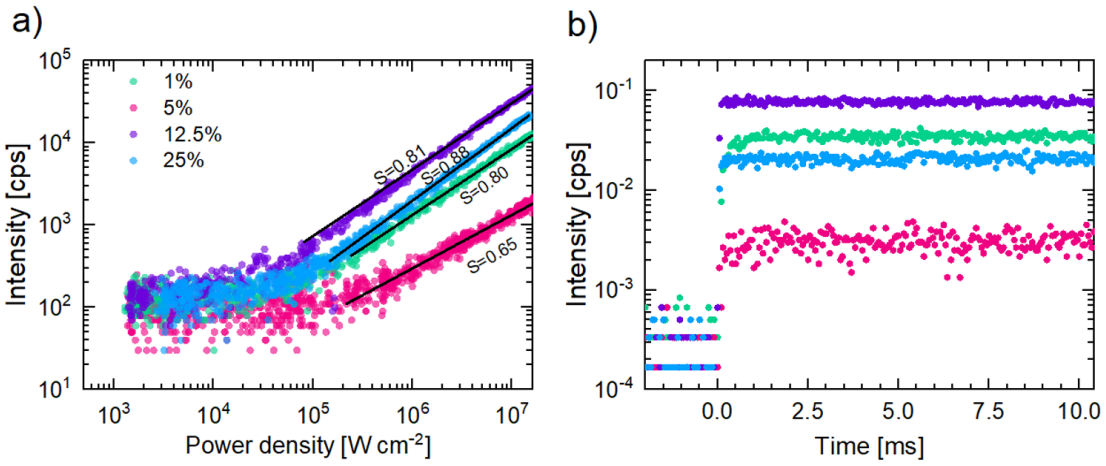

Figure 73. 2 (a) Dependence of luminescence intensity of Nd^{3+} emission on 800 on excitation power density (b) rise times for different concentrations of Nd^{3+} ions in $NaGdF_4$ measured at room temperature. The rise times were measured for 1 MW cm^{-2} with a time resolution of 50 µs.

Figure 73a illustrates the relationship between excitation power density and luminescence intensity for various Nd^{3+} concentrations at room temperature. However, in the case of all the samples we investigated, the power dependencies were nearly linear. There were no discernible thresholds or heightened non-linear slopes (as depicted in *Figure 73a)*, and neither were there extended luminescence risetimes (as shown in *Figure 73b).* These findings led us to conclude that no PA type of emission was present under the experimental conditions.

This observation likely arises from the similarity in energy gaps and multiphonon relaxation (MPR) rates along the series of non-radiative transitions: $^4I_{15/2} \rightsquigarrow {}^4I_{13/2} \rightsquigarrow {}^4I_{11/2} \rightsquigarrow {}^4I_{9/2}$. As the $^4I_{15/2} \rightsquigarrow {}^4I_{13/2}$ MPR populates the pivotal $^4I_{11/2}$ level (the initial multiplet for energy looping), the subsequent $^4I_{11/2} \rightsquigarrow {}^4I_{9/2}$ transition is equally rapid and non-radiatively depopulates the $^4I_{11/2}$ excited state. This hinders the energy storage and looping, thus preventing PA emission.

The looping $^4I_{11/2}$ excited state is located approximately 2000 cm^{-1} above the $^4I_{9/2}$ ground state. Consequently, the $^4I_{11/2}$ state is likely thermally populated and undergoes enhanced MPR. Even though the energy of the pump photons is less than that of the emitted photons, the emission does not necessarily involve upconversion anti-Stokes processes; it can result from phonon-assisted absorption. The absence of a saturation regime,

commonly observed in up-conversion processes, further confirms that the observed anti-Stokes emission has a distinct origin, different from conventional upconversion looping.

Recently, PA has been demonstrated in Nd^{3+} ions in crystals with very low phonon energy (128 cm^{-1}) KPb_2Cl_5 [107]. The low phonon energies of nanoparticles facilitate upconversion luminescence from higher lanthanide excited states, leading to highly nonlinear, PA emission from the nanoparticles.

Following the unsuccessful verification of PA at room temperature in the materials under study, we opted to investigate the excitation power density dependence of the Nd^{3+} $^4F_{3/2} \rightarrow {}^4I_{9/2}$ luminescence across a range of temperatures, spanning from -200°C to 200°C. This was undertaken to determine whether any indications of PA emission, such as variations in pump power intensities, could be observed at temperatures both below and above room temperature.

As illustrated in *Figure 74a*, our findings for 12.5% Nd^{3+} doped NaGdF4 nanoparticles reveal no substantial deviations from the results obtained at room temperature, except for PA emission intensity. The intensity values corresponding to the chosen pumping power (11 MW cm^{-2}) are presented in *Figure 74b*. It is worth noting that temperature exerts a non-trivial influence on luminescence intensity but does not alter the pump power dependency. In particular, at temperatures below 0°C, the luminescence resulting from ESA is barely discernible, while just above 0°C, it experiences a significant increase, rising by a factor of 10 to 100-fold over a temperature span of approximately 100°C.

For the series of samples, we calculated well-established relative temperature sensitivity parameters, denoted as S_R (*Figure 74c*), using the relationship $S_R = \frac{1}{I_L} \cdot \frac{\Delta I_L}{\Delta T} \cdot 100\%$, where I_L represents luminescence intensity, ΔT signifies the temperature difference, and ΔI_L denotes the luminescence intensity difference between a given temperature I(T) and I(T+ΔT). The S_R values, reflecting how much the chosen parameter (in our case, absolute luminescence intensity) changes with variations in temperature, ranged from a few percent, with the highest value being approximately 12% $°C^{-1}$. This confirmed the very high susceptibility to temperature fluctuations and indicated their potential suitability for applications in the field of nano-thermometry [21].

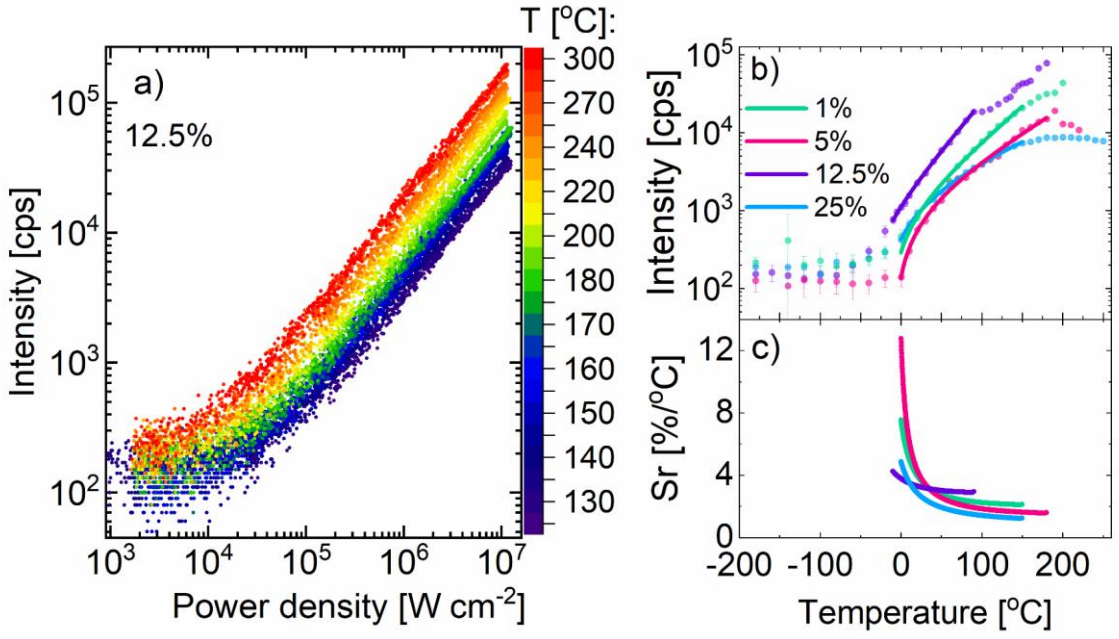

Figure 74. a) The dependence of luminescence intensity on the excitation laser power density for a wavelength of 860 nm in the temperature range from 125°C to 300°C for a sample containing 12.5% Nd^{3+}. The luminescence intensity as a function of temperature from -200°C to 200°C for various concentration of Nd^{3+}c) Relative temperature sensitivity at a constant pumping power density of 11 MW/cm^2 for different concentrations (1%, 5%, 12.5% and 25%) of Nd^{3+}.

Conclusions

During the course of our investigation, characteristic features of PA emissions could not be identified in any of the Nd-doped $NaGdF_4$@$NaGdF_4$ core-shell nanoparticles under 1064 nm photoexcitation, matching the ESA. On the contrary, the relationship between luminescence intensity and power density was found to be linear, and luminescence risetimes were rapid, exhibiting no dependence on pump power.

Furthermore, we conducted measurements on the luminescence intensity of Nd^{3+} ions at 860 nm for the maximum power density as a function of temperature. Notably, we observed significant variations in the emission intensity of the Nd-doped nanocrystals with changes in temperature during ESA excitation. Among the samples, the 12.5% Nd-doped nanocrystals exhibited the most robust emission, with the highest sensitivity (calculated from the intensity of a single band) reaching up to 12%/°C at 0°C for the 5% Nd-doped sample. This is a very high sensitivity of the luminescent thermometer as

compared to state-of-the-art in luminescence thermometry. These findings suggest a potential application of the studied materials in luminescence nanothermometry.

The luminescence intensity, influenced by the pump power, demonstrates a weak linear or quadratic dependency, as expected. Furthermore, the temperature dependence indicates negligible luminescence intensity at low temperatures, which gradually increases at higher temperatures. It is probable that at elevated temperatures, multiphoton relaxation processes become more pronounced, depopulating the critical level of $^4I_{11/2}$ and impeding the energy looping. Conversely, the thermal population of $^4I_{11/2}$ is responsible for the high temperature sensitivities observed.

6.4.Attempts to find PA in Ho^{3+}

We wanted to evaluate existence of PA emission also in Ho doped matrices. Where PA was previously observed in Ho ions was briefly described in the introduction.

Therefore, we investigated whether PA emission occurs in holmium ions. First for Holmium alone (0.5%Ho^{3+} and 2%Ho^{3+}), then co-doped Yb^{3+}, because we expected a similar effect to the sensitization of Pr^{3+} with Yb^{3+} ions. Below is a list of samples that were synthesized by Magdalena Dudek:

Core:

1. $NaYF_4$:0.5% Ho^{3+} 20% Yb^{3+}
2. $NaYF_4$:1% Ho^{3+} 20% Yb^{3+}
3. $NaYF_4$:2% Ho^{3+} 20% Yb^{3+}
4. $NaYF_4$:4% Ho^{3+} 20% Yb^{3+}
5. $NaYF_4$:8% Ho^{3+} 20% Yb^{3+}

Core-shell:

1. $NaYF_4$:0.5% Pr^{3+} 20% Yb^{3+} @$NaYF_4$
2. $NaYF_4$:1% Pr^{3+} 20% Yb^{3+} @$NaYF_4$
3. $NaYF_4$:2% Pr^{3+} 20% Yb^{3+} @$NaYF_4$
4. $NaYF_4$:4% Pr^{3+} 20% Yb^{3+} @$NaYF_4$
5. $NaYF_4$:8% Ho^{3+} 20% Yb^{3+}@$NaYF_4$
6. $NaYF_4$:0.5% Pr^{3+}
7. $NaYF_4$:2% Pr^{3+}

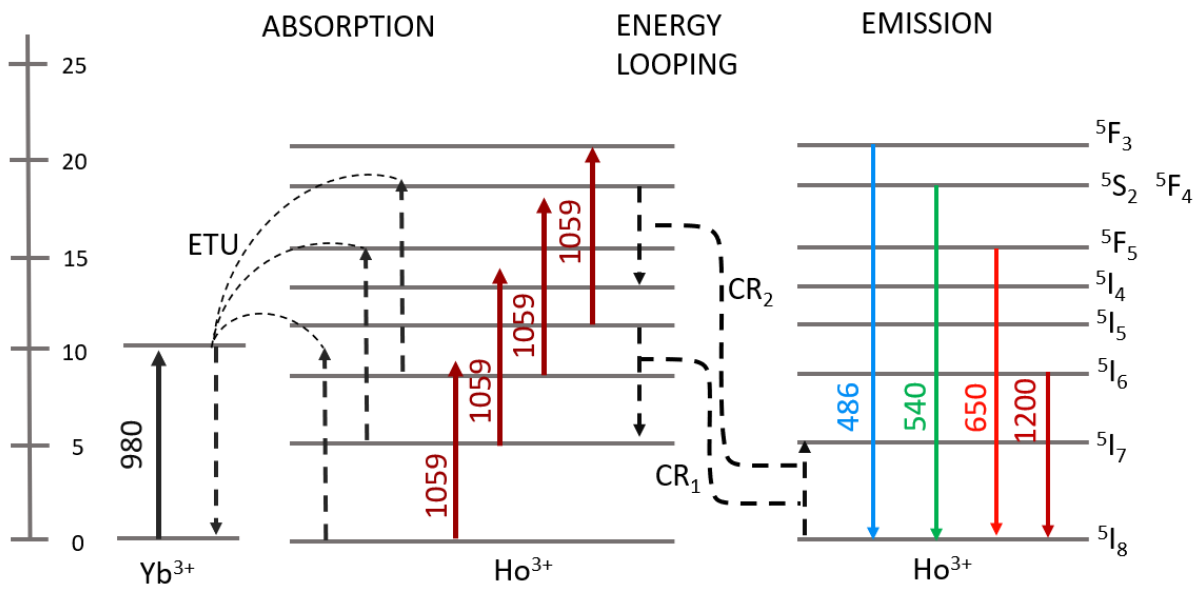

Figure 75. Energy diagram in Yb^{3+} and Ho^{3+}.

Figure 75 shows the energy levels in Yb^{3+} and Ho^{3+} ions. In the first case, I excited the nanocrystals with a laser with a beam wavelength of 1059 nm, then with a laser with a beam wavelength of 980. As a result of the analysis, we predicted that the 1064 wavelength laser should enable PA in Ho^{3+} ions. At the very end, I checked the behavior of the nanocrystals under constant excitation of 980 nm (for three different values) and for avalanche excitation, that is, for a higher power density of the excitation laser. Unfortunately, in neither of these cases was it possible to obtain PA emission.

I performed measurements of the dependence of luminescence intensity as a function of the power density of the excitation laser under 1059 nm excitation. The measurements were performed in two channels for the emission at the 650 nm and 540 nm (*Figure 76.*) Unfortunately, none of the samples showed PA, the slope of the curve for both emissions was about , there was no clear threshold of PA for both core and core shell nanocrystals. From the measurements it could be observed that nanocrystals without Yb^{3+} co-doping had lower luminescence intensity (by up to 4 orders of magnitude) and the emission began to increase much later, that is, for higher excitation laser power (10^6 - up to 10^7 W cm^{-2}).

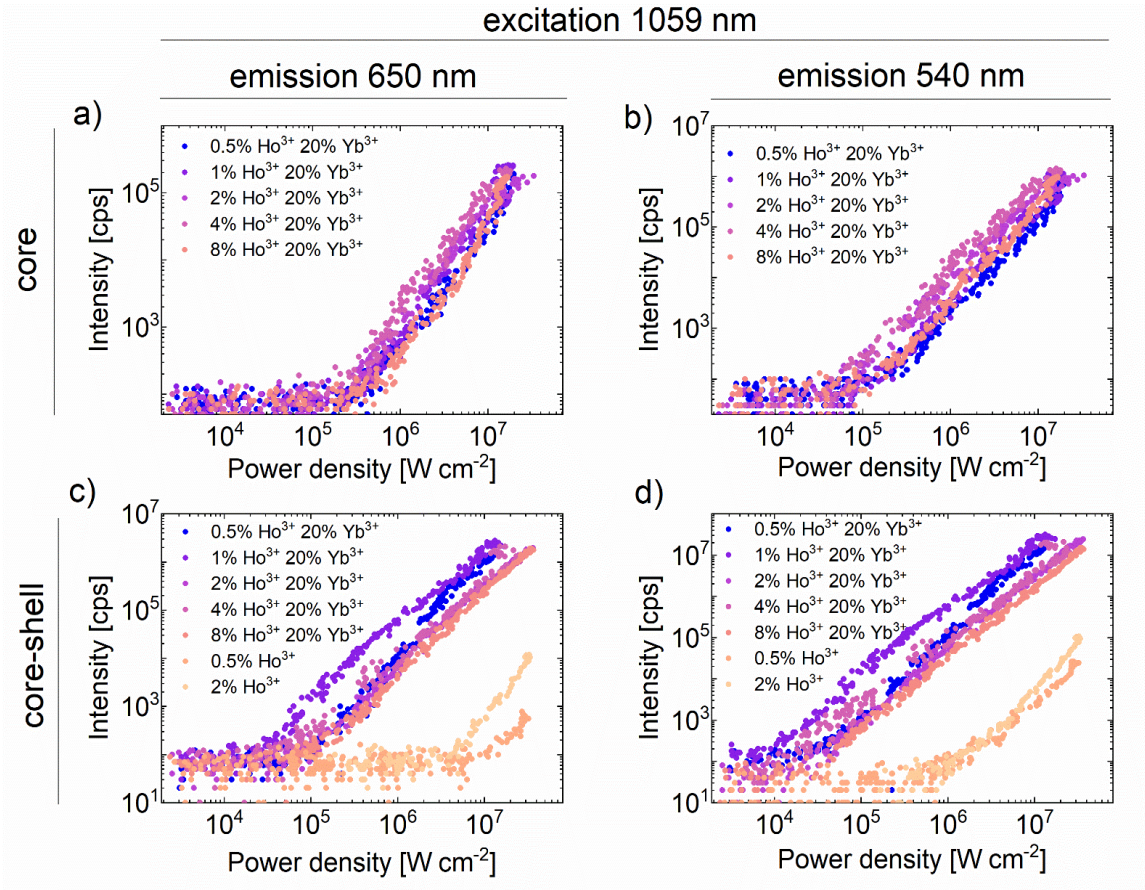

Figure 76. Dependence of luminescence intensity on 1059nm excitation laser power density for NaYF4 core (a) and (b) nanocrystals and core-shell (c) (d) for two emissions 650nm: (a) and (c) and 540nm: (b) and (d).

Subsequently, PA searches took place under 975 nm laser excitation. Under this excitation, some probes core with Yb^{3+} ions ($NaYF_4$:2% Ho^{3+} 20% Yb^{3+}, $NaYF_4$:4% Ho^{3+} 20% Yb^{3+}, $NaYF_4$:8% Ho^{3+} 20% Yb^{3+}) showed upconversions and of course samples without Yb^{3+} did not even showed emission. *Figure 77* shows the recorded emissions.

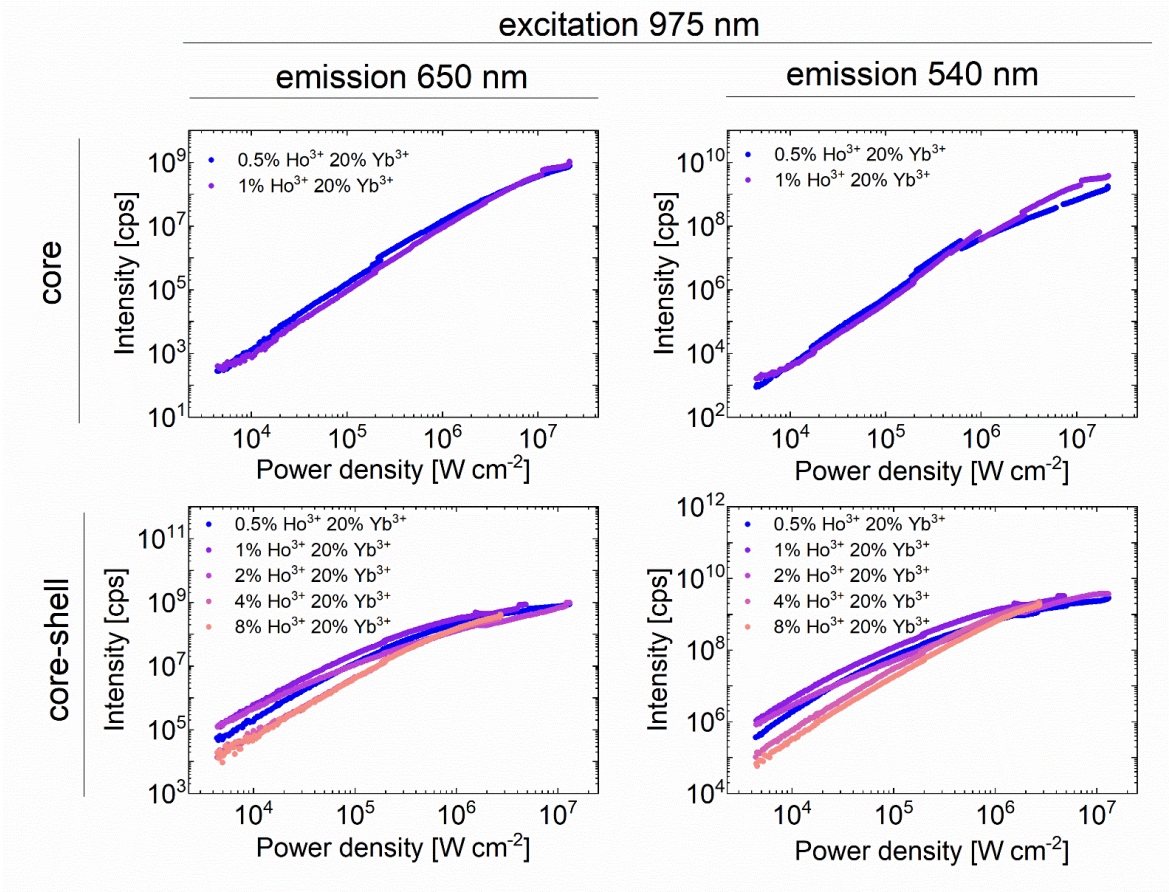

Figure 77. Dependence of luminescence intensity on 975nm excitation laser power density for $NaYF_4$ core a) and b) nanocrystals and core-shell c) d) for two emissions 650nm: a) and c) and 540nm: b) and d).

Moreover, the spectra under 975 nm excitation for different excitation laser power were also registered .clearly two dominant emissions can be seen, they are 650 and 540, which correspond to transitions to levels ($^5F_5 \rightarrow {}^5I_8$ and $^5S_2$, $^5F_4 \rightarrow {}^5I_8$).

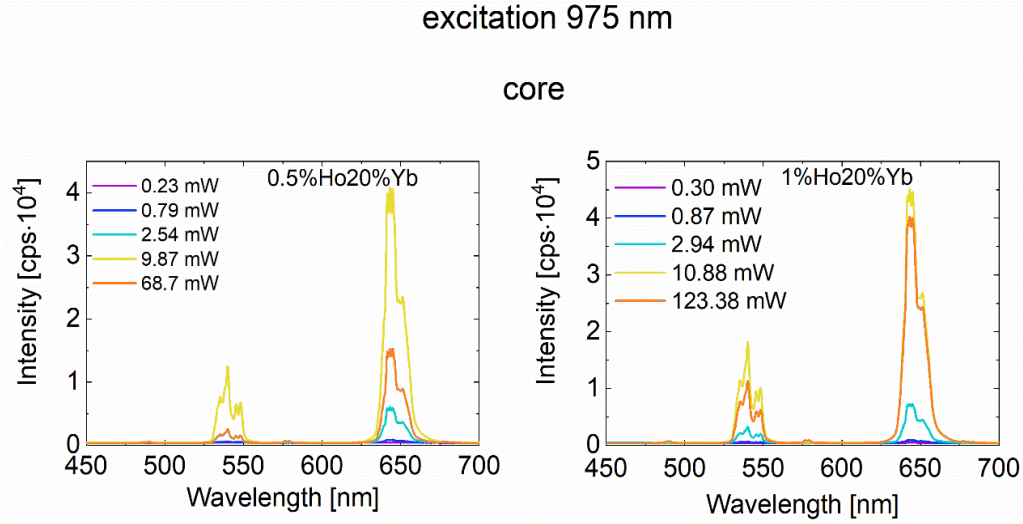

Figure 78. Emission spectra of core nanocrystals under 975 nm excitation for different laser powers. a) Emission spectra for $NaYF_4$:0.5%Ho^{3+}20%Yb b) Emission spectra for $NaYF_4$:1%Ho^{3+}20%Yb.

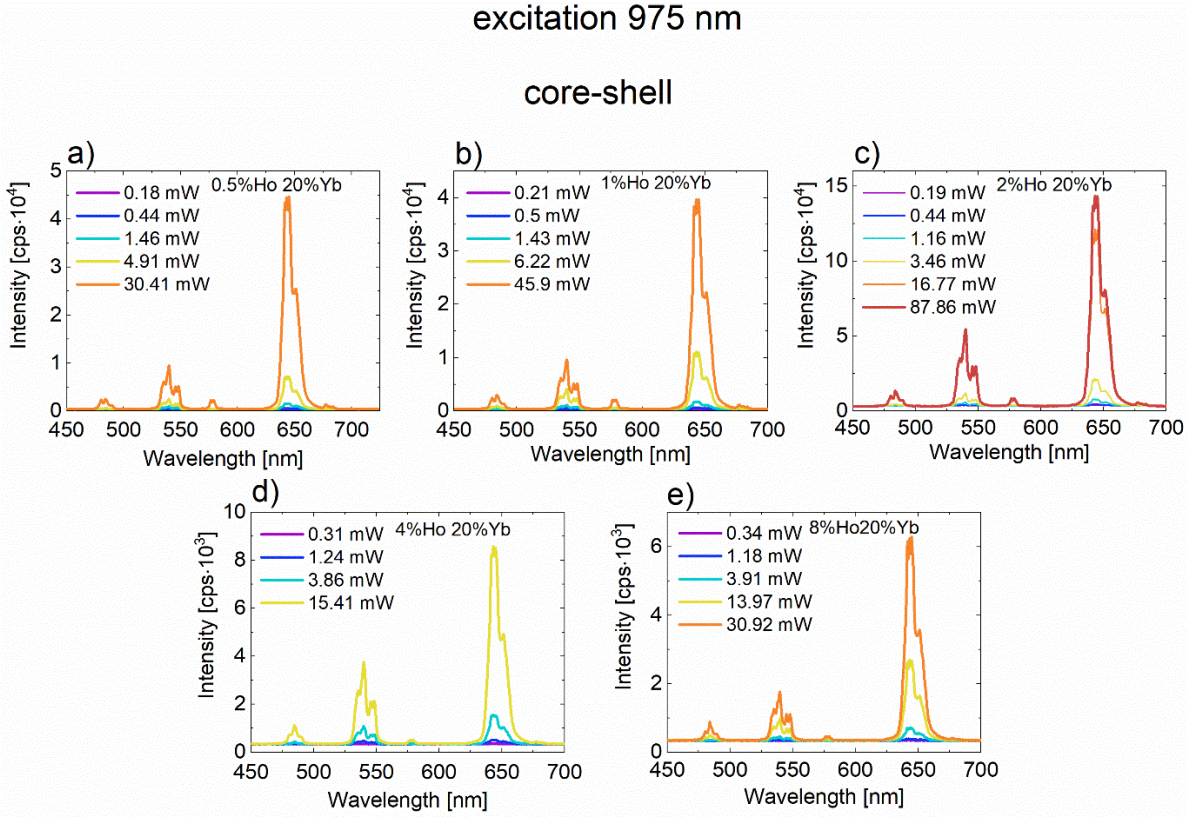

Figure 79. Emission spectra of core-shell nanocrystals under 975 nm excitation for different laser powers. a) Emission spectra for $NaYF_4$:0.5%Ho^{3+}20%Yb b) Emission spectra for $NaYF_4$:1%Ho^{3+}20%Yb c) Emission spectra for $NaYF_4$:2%Ho^{3+}20%Yb d) Emission spectra for $NaYF_4$:4%Ho^{3+}20%Yb e) Emission spectra for $NaYF_4$:8%Ho^{3+}20%Yb.

Conclusions

Failure to obtain PA may be related to not pumping enough the level from which energy looping occurs, or failing to reach high on the energy ladder. PA is a very sensitive process, perhaps the ion concentration is wrong, too small does not give a sufficiently effective CR, and too large, can cause the CR to extinguish the emission. Another reason could be an incompatible excitation wavelength, which originate from the fact we do not know ESA spectra and experimental measurements of ESA are not trivial and unfortunately beyond the scope of my current work. Probably the ratio of the absorption cross-section from the excited state (σESA) to the cross-section from the ground state (σGSA), β, is too small.

7. Dissertation conclusions

The studies planned and performed within this doctoral thesis, entitled "Evaluation of luminescent properties of photon avalanching nano-, micro- and bulk crystals: novel materials, characterization methods and applications," represents a significant and comprehensive exploration into the realm of PA in lanthanide-doped crystals. This study has made substantial contributions to both the theoretical understanding and practical applications of luminescent phenomena, particularly focusing on nano- and microcrystals doped with lanthanide ions such as Tm^{3+}, Nd^{3+}, Pr^{3+}, and Ho^{3+}.

A pivotal aspect of this research involved designing, construction, and optimization of a custom optical microscope-based measurement system. This non-commercial system, built from the ground up, was capable of measuring luminescent properties (pump power dependent spectra, intensities and rise/decay kinetics) of the materials over a wide range of photoexcitation power densities, from 10^2 to 10^7 Wcm^{-2}.

Beside developing the core instrument, substantial objective of this doctoral work delved into the intricate spectroscopic and avalanche properties of lanthanide-doped crystals.

The main part of this dissertation involved complex measurements of the spectroscopic and avalanche properties of lanthanide-doped crystals.

I have investigated the spectroscopic properties of Tm^{3+} ions in terms of various factors affecting PA. These factors include crystal size by bulk micro and nano.

The volume and scale of the material play a significant role in the PA phenomenon, giving rise to two distinct outcomes. With an increase in material size, there is a proportional rise in the number of ions it contains. In the context of PA, characterized by its collective nature, the efficient interaction among numerous ions becomes pivotal for the accumulation of energy in the metastable state.

A greater ion population offers diverse interaction possibilities, and larger material dimensions reduce the impact of surface quenching. Surface quenching involves energy transfer to external molecules, potentially causing the loss of the system's ability to emit light. In the case of smaller materials, particularly at the nanoscale, the significance of surface effects becomes more pronounced, especially when considering a bare core or a core with a protective shell. The influence of these factors on PA is evident in the shift

of S-shaped characteristics. Smaller materials, constrained by a limited ion count, exhibit a more pronounced contribution from surface effects, resulting in a shift in the PA threshold. Conversely, larger materials exhibit brighter luminescence effects. Additionally, S-shaped curves shift towards higher values, indicating that a greater amount of energy must be supplied to achieve comparable effects.

Furthermore, distinct concentrations of Tm^{3+} ions impact the dependence of luminescence intensity on the power density of the excitation laser. At lower concentrations (3%), the effect is more localized and has less volume spread, rendering the nano shell less influential. At higher concentrations (8%), the increased ion count prevents saturation, facilitating efficient energy exchange with neighboring ions. Here, the protective role of the shell becomes more prominent, safeguarding the nanocrystal from quenching.

Another factor investigated affecting PA was dopant concentration of Tm^{3+} ions. Microcrystals of $LiYF_4$ doped with varying concentrations of thulium were examined, with each sample displaying PA. As the concentration of thulium increased, both the occurrence of avalanche events and the slope of the luminescence intensity-power density dependence curve exhibited an upward trend. This observation is likely attributed to the enhanced efficiency of CR, which influence the population of the metastable level from which the efficient ESA occurs.

For emission at 800 nm, the maximum slope of the curve shows an increasing trend with increasing concentration. The average maximum slope for a concentration of 1% oscillates around 10, while for the highest concentration of 16% it averages 28. Similarly, for emissions at 450 nm, the maximum slope of the curve increases with increasing concentration. The slope for a concentration of 1% is around 6, while for the highest concentration of 16% it averages 15.

The PA threshold appeared to be smallest for microcrystals with a concentration of 3% for both 800 nm and 450 nm emission. These crystal properties enable the optimal sample to be selected based on power density, achieving the desired PA threshold and exhibiting the highest slope for the smallest avalanche threshold.

For the first time, this study investigates the interaction between Tm^{3+}-doped $LiYF_4$ crystals (with 3% Tm^{3+} content) and plasmonic nanoparticles - AuNRs. The aim was to examine whether the combination of these materials would enhance or diminish the PA

emission. The addition of gold nanorods to nanocrystals resulted in decreased luminescence, possibly due to reabsorption of gold nanorods at the wavelength of 800 nm. Energy transfer from excited nanocrystals to gold nanoparticles was observed in both core and core-shell nanocrystals. Core-shell nanocrystals exhibited higher luminescence intensity, attributed to the protective role of the passive shell against surface quenching. In microcrystals, the addition of gold nanorods in a 1:1 ratio led to emission enhancement, while higher concentrations (1:5 and 1:20) resulted in reduced luminescence. The dependence of luminescence intensity on excitation laser power density (1059 nm) was measured for pure and gold nanorod-mixed core, core-shell, and microcrystals. In nanocrystals, the presence of AuNRs shifted the s-shape curve towards higher powers, causing a sudden increase in luminescence at higher power densities for both 800 nm and 475 nm emissions.

Due to the long lifetimes of the energy levels in lanthanide ions, various combinations of rise times and signals were possible to measure. The dynamics of the rise time depends on the initial occupation of the metastable state. With the initial pumping of the level and not allowing the energy to fully "discharge" after the previous excitation pulse, a faster increase in emission occurred during subsequent excitation pulses. PA measurements facilitate the entirely optical processing of complex signals using reservoir computing concept. The luminescence generated by pulses is affected by the time intervals between consecutive, identical excitation pulses. PA synapses demonstrate a phenomenon known as PPF amplifying the luminescence intensity in response to previous photostimulation history. These properties resemble to neuronal synaptic functioning, making them applicable for optical amplification, entirely optical signal processing, and information storage.

In the subsequent study, our aim was to illustrate and assess the sensitivity of the PA phenomenon to the presence of an energy acceptor resonating with the loop state. To accomplish this, we utilized $LiYF_4$ microcrystals doped with 3% Tm^{3+} and varying percentages of Tb^{3+} ions, and subsequently analyzed the experimental results. The luminescence intensity of the $^3H_4 \rightarrow {}^3H_6$ transition at 1059 nm excitation undergoes a noticeable decrease with increasing terbium ion concentration and significantly shifts the PA threshold towards higher excitation laser power densities. As a consequence, the full S-shaped PA pattern is not observed for the highest steepness (3% Tb^{3+}) In addition, the PA slope, initially peaking at 30 for the 0.05% Tb^{3+} dopant,

decreases with increasing terbium ion concentration, eventually reaching about 3 for the sample containing 3% Tm^{3+} and 3% Tb^{3+}. Similar changes were observed for the blue PA emission from the higher energy level of $^1D^2$ Tm^{3+} measured at 450 nm. This observation underscores the potential of Tb^{3+} doping as an effective method to modulate and regulate the PA response. In the future, these findings could hold promising implications for advancing PA-based biosensing applications. The precise control over the PA phenomenon has the potential to significantly enhance the sensitivity of the detection process.

Subsequently I have investigated the PA phenomenon in different nanocrystal matrices for the same 8% Tm^{3+} dopant. Afterwards I investigated the dependence of luminescence intensity on excitation laser power density (1059 nm) for emissions at 800 nm. $LiYF_4$ nanocrystals exhibited the steepest curve slope (7.1), followed by $NaYF_4$ (4.7), KYF_4 (2.7), and CaF_2 (2.3), with the smallest observed for Gd_2O_3 (1.8). The smallest PA threshold was found for CaF_2 crystals, while the largest occurred for Gd_2O_3. Beyond the matrix and the associated phonon energy's impact on PA emission, the nanocrystal shape also plays a role. Despite all nanocrystals having a core structure, making them susceptible to surface quenching, Gd_2O_3 crystals, with their flat configuration and larger surface area, may experience disruptions in PA due to potential defects on the surface. Furthermore, to achieve PA, a delicate balance between energy looping, MPR, and emission is essential. sigma ESA(l)

Furthermore, I carried out temperature measurements of PA in Pr^{3+} ions under 852 nm laser excitation. As the temperature increased, the PA threshold shifted towards higher powers, for which the slope of the S-shape curve was greatest (9) for temperature 0˚C. PA was measured for different temperatures. I introduced a new thermometric parameter - i.e. the PA threshold. At the same time, a luminescence thermometer with high temperature sensitivity was demonstrated, one of the parameters was the luminescence intensity, and in this case the relative sensitivity of this thermometer reached 7.5% $°C^{-1}$ at 0 °C, and for the parameter in which the PA threshold - this approach allowed us to achieve a relative temperature sensitivity above 0.5 % $°C^{-1}$ for the entire temperature range.

In addition, I performed temperature-dependent luminescence intensity measurements for Nd ions and also calculated a high temperature sensitivity for this material, despite no

characteristic features of PA emission was noticed in Nd:$GdYF_4$@: $NaGdF_4$ at 1059 nm photoexcitation.
I achieved a high temperature sensitivity of 12% $°C^{-1}$ for sample with 12.5% Nd^{3+} at 0°C.

Unfortunately, achieving the PA process in Ho^{3+} ions has proven challenging. This process is highly sensitive, and the issue may stem from inappropriate ion concentration. Insufficient concentration might hinder effective CR transitions, while excessively high concentration could lead to quenching of the emission due to CR effects. Another possible factor contributing to the failure is the incompatible excitation wavelength, which is a result of the unknown spectra of the energy transfer from ESA. Unfortunately, experimental measurements of ESA are non-trivial and currently beyond the scope of my work.

The study highlighted the great importance of PA in nanocrystals and microcrystals, emphasizing their unique properties depending on size, dopant concentration or temperature. The versatility of PA has been demonstrated in applications such as (bio)sensing, optical signal processing and luminescent thermometry. These applications demonstrate the diverse and promising possibilities of using PA in cutting-edge technologies.

The dissertation not only presented important findings but also contributed to methodological advancements in the field. The implementation of a robust experimental procedure for PA measurements, coupled with the development of an algorithm for data analysis using Matlab, facilitated operator-independent analysis. This methodological contribution enhances the reproducibility and reliability of future experiments in the domain of PA.

In conclusion, this doctoral thesis significantly advances the knowledge base of PA in lanthanide-doped crystals. The results of this research could have an impact on the fields of nanotechnology and photonics, offering a rich source of information.

Acknowledgements

Research was supported by the projects 2018/31/B/ST5/01827 and 2021/43/B/ST5/01244 funded by the National Science Centre. Calculations have been carried out using resources provided by Wroclaw Centre for Networking and Supercomputing (http://wcss.pl), grant No. 529.

8. Bibliography

[1] J. S. Chivian, W. E. Case, and D. D. Eden, “The photon avalanche: A new phenomenon in Pr3+-based infrared quantum counters,” *Appl. Phys. Lett.*, vol. 35, no. 2, pp. 124–125, 1979, doi: 10.1063/1.91044.

[2] J. C. G. Bünzli and C. Piguet, “Taking advantage of luminescent lanthanide ions,” *Chem. Soc. Rev.*, vol. 34, no. 12, pp. 1048–1077, 2005, doi: 10.1039/b406082m.

[3] C. E. Lambert, “Lanthanide series of metals,” *Encycl. Toxicol.*, pp. 691–694, 2005, doi: 10.1016/B0-12-369400-0/01096-6.

[4] J. Bünzli and S. V Eliseeva, “Basics of Lanthanides Photophysics. In Lanthanide Luminescence,” *Hänninen P., Härmä H. Lanthan. Lumin. Springer Ser. Fluoresc. (Methods Appl.*, vol. 7, no. July 2010, pp. 1–45, 2010, doi: 10.1007/4243.

[5] “Fizyczna Chemia Nieorganiczna. S.F.A. Kettle - część II.pdf.”

[6] “Chemia nieorganiczna (1994, Wydawnictwo Naukowe PWN) - Lothar Kolditz.pdf.”

[7] *NOMENCLATURE OF INORGANIC CHEMISTRY IUPAC Recommendations 2005 IUPAC Periodic Table of the Elements Fm No*. 2005.

[8] S. Cotton, *Lanthanide and Actinide Chemistry*. 2006. doi: 10.1002/0470010088.

[9] P. Hänninen and H. Härmä, *Lanthanide Luminescence: Photophysical, Analytical and Biological Aspects*. Springer Berlin Heidelberg, 2011. [Online]. Available: https://books.google.pl/books?id=SWxwcXO94M8C

[10] Z. Luo and Y. Huang, *Springer Series in Materials Science 289 Physics of Solid-State Laser Materials*. 2020.

[11] S. K. Sharma, D. S. Verma, L. U. Khan, S. Kumar, and S. B. Khan, *Handbook of Materials Characterization*, no. September. 2018. doi: 10.1007/978-3-319-92955-2.

[12] R. Pązik, “Synteza i zbadanie własności optycznych i elektrycznych nanokrystalicznych materiałów BaTiO3 domieszkowanych jonami ziem rzadkich,” *Pr. doktorska*, pp. 1–184, 2008.

[13] V. V. Ter-Mikirtychev, *Optical spectroscopy of rare-earth ions in the solid state*,

3rd ed. Elsevier Ltd., 2016. doi: 10.1016/B978-0-12-409547-2.12095-5.

[14] A. Skripka, “Rare Earth Nanoparticles: Building Theranostic Agents From the Ground Up,” pp. 1–231, 2020.

[15] A. A. Kaminskii, *Crystalline lasers Physical Processes and Operating Schemes.pdf*. Boca Raton: CRC Press, 1996.

[16] G. Chen, H. Qiu, P. N. Prasad, and X. Chen, “Upconversion nanoparticles: Design, nanochemistry, and applications in Theranostics,” *Chemical Reviews*, vol. 114, no. 10. American Chemical Society, pp. 5161–5214, May 2014. doi: 10.1021/cr400425h.

[17] S. Gao, *Molecular Nanomagnet and Related Phenomena*. 2015.

[18] G. H. Dieke, H. M. Crosswhite, and B. Dunn, “Emission Spectra of the Doubly and Triply Ionized Rare Earths*,” *J. Opt. Soc. Am.*, vol. 51, no. 8, p. 820, 1961, doi: 10.1364/josa.51.000820.

[19] O. Eriksson, “4f ’ 4f,” vol. 41, no. 10, pp. 7311–7314, 1990.

[20] J. Katriel and R. Pauncz, “Theoretical Interpretation of Hund’s Rule,” *Adv. Quantum Chem.*, vol. 10, no. C, pp. 143–185, 1977, doi: 10.1016/S0065-3276(08)60580-8.

[21] S. Da Jiang, B. W. Wang, and S. Gao, “Advances in lanthanide single-ion magnets,” *Struct. Bond.*, vol. 164, pp. 111–142, 2014, doi: 10.1007/430_2014_153.

[22] C. Feldmann, T. Jüstel, C. R. Ronda, and P. J. Schmidt, “Inorganic luminescent materials: 100 Years of research and application,” *Adv. Funct. Mater.*, vol. 13, no. 7, pp. 511–516, 2003, doi: 10.1002/adfm.200301005.

[23] M. Bottrill, L. Kwok, and N. J. Long, “Lanthanides in magnetic resonance imaging,” *Chem. Soc. Rev.*, vol. 35, no. 6, pp. 557–571, 2006, doi: 10.1039/b516376p.

[24] “teo-et-al-2016-lanthanides-applications-in-cancer-diagnosis-and-therapy.pdf.crdownload.”

[25] L. Zhou, J. Huang, and F. Mo, “Preparation and photoluminescence properties of

MgNb2O 6:Eu3+, Bi3+ red-emitting phosphor," *Mater. Sci. Pol.*, vol. 32, no. 1, pp. 88–92, 2014, doi: 10.2478/s13536-013-0157-x.

[26] S. Ye, F. Xiao, Y. X. Pan, Y. Y. Ma, and Q. Y. Zhang, "Phosphors in phosphor-converted white light-emitting diodes: Recent advances in materials, techniques and properties," *Mater. Sci. Eng. R Reports*, vol. 71, no. 1, pp. 1–34, 2010, doi: 10.1016/j.mser.2010.07.001.

[27] R. W. Boyd, "The nonlinear optical susceptibility - Chapter 1," *Nonlinear Opt.*, no. 1941, pp. 1–67, 1961.

[28] T. Informacyjnych, "POLITECHNIKA WARSZAWSKA Wydział Elektroniki i Technik Informacyjnych ROZPRAWA DOKTORSKA," 2014.

[29] F. Auzel, "Upconversion processes in coupled ion systems," *J. Lumin.*, vol. 45, no. 1–6, pp. 341–345, 1990, doi: 10.1016/0022-2313(90)90189-I.

[30] F. Auzel, "Upconversion and Anti-Stokes Processes with f and d Ions in Solids," *Chem. Rev.*, vol. 104, no. 1, pp. 139–173, 2004, doi: 10.1021/cr020357g.

[31] M.-F. Joubert, "Photon avalanche upconversion in rare earth laser materials," *Opt. Mater. (Amst).*, vol. 11, no. 2–3, pp. 181–203, 1999, doi: 10.1016/S0925-3467(98)00043-3.

[32] H. Dong, L. D. Sun, and C. H. Yan, "Energy transfer in lanthanide upconversion studies for extended optical applications," *Chem. Soc. Rev.*, vol. 44, no. 6, pp. 1608–1634, 2015, doi: 10.1039/c4cs00188e.

[33] P. J. Dereń, J. C. Krupa, and W. Strek, "Blue emission of Pr3+ ions in LaCl3 crystal triggered by U3+," *J. Alloys Compd.*, vol. 300, pp. 18–22, 2000, doi: 10.1016/S0925-8388(99)00707-0.

[34] N. V Tkachenko, *Optical Spectroscopy: Methods and Instrumentations*. Elsevier Science, 2006. [Online]. Available: https://books.google.pl/books?id=rBepb6daR9MC

[35] A. Grzybowski and K. Pietrzak, "Maria Goeppert-Mayer (1906-1972): two-photon effect on dermatology.," *Clin. Dermatol.*, vol. 31, no. 2, pp. 221–225, 2013, doi: 10.1016/j.clindermatol.2012.06.002.

[36] E. Nakazawa and S. Shionoya, “Cooperative luminescence in YbPO4,” *Phys. Rev. Lett.*, vol. 25, no. 25, pp. 1710–1712, 1970, doi: 10.1103/PhysRevLett.25.1710.

[37] M. J. V Bell, W. G. Quirino, S. L. Oliveira, D. F. De Sousa, and L. A. O. Nunes, “Cooperative luminescence in Yb 3 + -doped phosphate,” *J. Phys. Condens. Matter*, vol. 15, pp. 4877–4887, 2003.

[38] P. Goldner, F. Pellé, and F. Auzel, “Theoretical evaluation of cooperative luminescence rate in Yb3+ : CsCdBr3 and comparison with experiment,” *J. Lumin.*, vol. 72–74, pp. 901–903, 1997, doi: 10.1016/S0022-2313(96)00238-4.

[39] P. Goldner, B. Schaudel, and M. Prassas, “Dependence of cooperative luminescence intensity on (formula presented) spatial distribution in crystals and glasses,” *Phys. Rev. B - Condens. Matter Mater. Phys.*, vol. 65, no. 5, pp. 1–10, 2002, doi: 10.1103/PhysRevB.65.054103.

[40] J. Ueda and S. Tanabe, “Sensitization mechanisms of 1 μm luminescence in Tb 3+-Yb 3+ co-doped borate glasses,” *Phys. Status Solidi Appl. Mater. Sci.*, vol. 208, no. 8, pp. 1827–1832, 2011, doi: 10.1002/pssa.201084072.

[41] E. A. Gouveia, J. P. Jouart, and M. Bouffard, “Phonon-assisted cooperative sensitization of Tb3+ in SrCl2:Yb, Tb,” *J. Phys. Condens. Matter*, vol. 14, no. 1, pp. 5461–5475, 2002.

[42] “jpsj.32.1577.pdf.”

[43] M. F. Joubert, S. Guy, B. Jacquier, and C. Linarés, “The photon-avalanche effect: review, model and application,” *Opt. Mater. (Amst).*, vol. 4, no. 1, pp. 43–49, 1994, doi: 10.1016/0925-3467(94)90054-X.

[44] C. Lee *et al.*, “Giant nonlinear optical responses from photon-avalanching nanoparticles,” *Nature*, vol. 589, no. 7841, pp. 230–235, 2021, doi: 10.1038/s41586-020-03092-9.

[45] M. F. Joubert, S. Guy, and B. Jacquier, “Model of the photon-avalanche effect,” *Phys. Rev. B*, vol. 48, no. 14, pp. 10031–10037, 1993, doi: 10.1103/PhysRevB.48.10031.

[46] A. S. L. Gomes, G. S. Maciel, R. E. de Araújo, L. H. Acioli, and C. B. de Araújo, “Diode pumped avalanche upconversion in Pr3+-doped fibers,” *Opt. Commun.*,

vol. 103, no. 5–6, pp. 361–364, 1993, doi: 10.1016/0030-4018(93)90157-Z.

[47] S. Kück *et al.*, "Avalanche up-conversion processes in Pr, Yb-doped materials," *J. Alloys Compd.*, vol. 300, pp. 65–70, 2000, doi: 10.1016/S0925-8388(99)00734-3.

[48] T. Sandrock, H. Scheife, E. Heumann, and G. Huber, "High-power continuous-wave upconversion fiber laser at room temperature," *Opt. Lett.*, vol. 22, no. 11, p. 808, 1997, doi: 10.1364/ol.22.000808.

[49] E. Osiac *et al.*, "Orange and red upconversion laser pumped by an avalanche mechanism in Pr3+, Yb3+:BaY2F8," *Appl. Phys. Lett.*, 2003, doi: 10.1063/1.1579561.

[50] E. Osiac *et al.*, "Spectroscopic characterisation of the upconversion avalanche mechanism in Pr3+,Yb3+:BaY2F8," *Opt. Mater. (Amst).*, 2003, doi: 10.1016/S0925-3467(03)00089-2.

[51] W. Lenth and R. M. Macfarlane, "Excitation mechanisms for upconversion lasers," *J. Lumin.*, vol. 45, no. 1–6, pp. 346–350, 1990, doi: 10.1016/0022-2313(90)90190-M.

[52] L. Marciniak, W. Strek, A. Bednarkiewicz, A. Lukowiak, and D. Hreniak, "Bright upconversion emission of Nd3+ in LiLa1-xNdxP4O12 nanocrystalline powders," *Opt. Mater. (Amst).*, vol. 33, no. 10, pp. 1492–1494, 2011, doi: 10.1016/j.optmat.2011.03.005.

[53] H. Dong *et al.*, "Lanthanide Nanoparticles: From Design toward Bioimaging and Therapy," *Chem. Rev.*, vol. 115, no. 19, pp. 10725–10815, Oct. 2015, doi: 10.1021/acs.chemrev.5b00091.

[54] J. F. Da Silva, R. F. Da Silva, E. P. Santos, L. J. Q. Maia, and A. L. Moura, "Photon-avalanche-like upconversion in NdAl3(BO3)4nanoparticles excited at 1064 nm," *Appl. Phys. Lett.*, vol. 117, no. 15, 2020, doi: 10.1063/5.0024619.

[55] E. P. Santos *et al.*, "Temperature triggering a photon-avalanche-like mechanism in NdAl3(BO3)4 particles under excitation at 1064 nm," *J. Lumin.*, vol. 245, no. November 2021, 2022, doi: 10.1016/j.jlumin.2021.118645.

[56] D. Wawrzynczyk, A. Bednarkiewicz, M. Nyk, W. Strek, and M. Samoc, "Neodymium(iii) doped fluoride nanoparticles as non-contact optical temperature

sensors," *Nanoscale*, vol. 4, no. 22, pp. 6959–6961, 2012, doi: 10.1039/c2nr32203j.

[57] T. Hebert, R. Wannemacher, R. M. MacFarlane, and W. Lenth, "Blue continuously pumped upconversion lasing in Tm:YLiF4," *Appl. Phys. Lett.*, vol. 60, no. 21, pp. 2592–2594, May 1992, doi: 10.1063/1.106919.

[58] H. Ni and S. C. Rand, "Avalanche upconversion in Tm:YALO_3," *Opt. Lett.*, vol. 16, no. 18, p. 1424, Sep. 1991, doi: 10.1364/ol.16.001424.

[59] S. Guy, M. F. Joubert, and B. Jacquier, "Photon avalanche upconversion in various Tm3+-doped materials," *J. Alloys Compd.*, vol. 275–277, pp. 186–190, 1998, doi: 10.1016/S0925-8388(98)00300-4.

[60] I. R. Martín *et al.*, "Room-temperature photon avalanche upconversion in Tm3+: Y2O3 crystals," *Phys. Rev. B*, vol. 60, no. 10, pp. 7252–7257, Sep. 1999, doi: 10.1103/PhysRevB.60.7252.

[61] F. Auzel and Y. H. Chen, "the First Step for the Photon Avalanche Process," vol. 184, pp. 57–60, 1995.

[62] I. R. Martín, V. D. Rodríguez, Y. Guyot, S. Guy, G. Boulon, and M. F. Joubert, "Room temperature photon avalanche upconversion in Tm3+-doped fluoroindate glasses," *J. Phys. Condens. Matter*, vol. 12, no. 7, pp. 1507–1516, 2000, doi: 10.1088/0953-8984/12/7/331.

[63] O. K. Alimov and M. E. Doroshenko, "Nonlinear luminescence of ZBLAN fluoride glasses," 1996.

[64] M. Malinowski, R. Piramidowicz, Z. Frukacz, G. Chadeyron, R. Mahiou, and M. F. Joubert, "Spectroscopy and upconversion processes in YAlO3:Ho3+ crystals," *Opt. Mater. (Amst).*, vol. 12, no. 4, pp. 409–423, 1999, doi: 10.1016/S0925-3467(98)00081-0.

[65] O. K. Liu, Y. H. Chen, and J. V. Beitz, "Photon avalanche up-conversion in Ho3+ doped fluoride glasses," *J. Lumin.*, vol. 81, no. 1, pp. 7–12, Jan. 1999, doi: 10.1016/S0022-2313(98)00059-3.

[66] A. Brenier, C. Garapon, C. Madej, C. Pédrini, and G. Boulon, "Dynamics of looping mechanisms in laser crystals," *Opt. Mater. (Amst).*, vol. 4, no. 1, pp. 51–

54, 1994, doi: 10.1016/0925-3467(94)90055-8.

[67] G. Vicidomini, P. Bianchini, and A. Diaspro, “STED super-resolved microscopy,” *Nat. Methods*, vol. 15, no. 3, pp. 173–182, 2018, doi: 10.1038/nmeth.4593.

[68] N. G. Horton *et al.*, “In vivo three-photon microscopy of subcortical structures within an intact mouse brain,” *Nat. Photonics*, vol. 7, no. 3, pp. 205–209, 2013, doi: 10.1038/nphoton.2012.336.

[69] F. Helmchen and W. Denk, “Deep tissue two-photon microscopy,” *Nat. Methods*, vol. 2, no. 12, pp. 932–940, 2005, doi: 10.1038/nmeth818.

[70] B. Huang, H. Babcock, and X. Zhuang, “Breaking the diffraction barrier: Super-resolution imaging of cells,” *Cell*, vol. 143, no. 7, pp. 1047–1058, 2010, doi: 10.1016/j.cell.2010.12.002.

[71] L. Schermelleh, R. Heintzmann, and H. Leonhardt, “A guide to super-resolution fluorescence microscopy,” *J. Cell Biol.*, vol. 190, no. 2, pp. 165–175, 2010, doi: 10.1083/jcb.201002018.

[72] C. Eggeling *et al.*, “Reversible photoswitching enables single-molecule fluorescence fluctuation spectroscopy at high molecular concentration,” *Microsc. Res. Tech.*, vol. 70, no. 12, pp. 1003–1009, 2007, doi: 10.1002/jemt.20505.

[73] H. Bock *et al.*, “Two-color far-field fluorescence nanoscopy based on photoswitchable emitters,” *Appl. Phys. B Lasers Opt.*, vol. 88, no. 2, pp. 161–165, 2007, doi: 10.1007/s00340-007-2729-0.

[74] A. Bednarkiewicz, E. M. Chan, A. Kotulska, L. Marciniak, and K. Prorok, “Photon avalanche in lanthanide doped nanoparticles for biomedical applications: Super-resolution imaging,” *Nanoscale Horizons*, vol. 4, no. 4, pp. 881–889, 2019, doi: 10.1039/c9nh00089e.

[75] M. Dudek *et al.*, “Size-Dependent Photon Avalanching in Tm3+ Doped LiYF4 Nano, Micro, and Bulk Crystals,” *Adv. Opt. Mater.*, vol. 10, no. 19, pp. 1–12, 2022, doi: 10.1002/adom.202201052.

[76] L. F. Johnson and H. J. Guggenheim, “Infrared-pumped visible laser,” *Appl. Phys. Lett.*, vol. 19, no. 2, pp. 44–47, 1971, doi: 10.1063/1.1653816.

[77] P. Goldner and F. Pellé, “Photon avalanche fluorescence and lasers,” *Opt. Mater. (Amst).*, vol. 5, no. 4, pp. 239–249, 1996, doi: 10.1016/0925-3467(96)00003-1.

[78] M. E. Koch, A. W. Kueny, and W. E. Case, “Photon avalanche upconversion laser at 644 nm,” *Appl. Phys. Lett.*, vol. 56, no. 12, pp. 1083–1085, 1990, doi: 10.1063/1.103328.

[79] P. Xie and T. R. Gosnell, “Room-temperature upconversion fiber laser tunable in the red, orange, green, and blue spectral regions,” *Opt. Lett.*, vol. 20, no. 9, p. 1014, 1995, doi: 10.1364/ol.20.001014.

[80] A. Fernandez-Bravo *et al.*, “Ultralow-threshold, continuous-wave upconverting lasing from subwavelength plasmons,” *Nat. Mater.*, vol. 18, no. 11, pp. 1172–1176, 2019, doi: 10.1038/s41563-019-0482-5.

[81] E. Osiac *et al.*, “Avalanche mechanism generating laser oscillation in Pr3+, Yb3+:BaY2F8,” 2003. doi: 10.1109/CLEOE.2003.1312090.

[82] M. H. Asghar, F. Placido, and S. Naseem, “P HYSICAL J OURNAL Characterization of reactively evaporated TiO 2 thin films as high,” *Eur. Phys. JournalApplied Phys.*, vol. 184, no. 3, pp. 177–184, 2006, doi: 10.1051/epjap.

[83] L. Liang, C. Wang, J. Chen, Q. J. Wang, and X. Liu, “Incoherent broadband mid-infrared detection with lanthanide nanotransducers,” *Nat. Photonics*, vol. 16, no. 10, pp. 712–717, 2022, doi: 10.1038/s41566-022-01042-7.

[84] J. S. Dam, P. Tidemand-Lichtenberg, and C. Pedersen, “Room-temperature mid-infrared single-photon spectral imaging,” *Nat. Photonics*, vol. 6, no. 11, pp. 788–793, 2012, doi: 10.1038/nphoton.2012.231.

[85] C. Xie *et al.*, “Single-chip, mid-infrared array for room temperature video rate imaging,” *Optica*, vol. 4, no. 12, p. 1498, 2017, doi: 10.1364/optica.4.001498.

[86] I. M. Pavlovetc, K. Aleshire, G. V. Hartland, and M. Kuno, “Approaches to mid-infrared, super-resolution imaging and spectroscopy,” *Phys. Chem. Chem. Phys.*, vol. 22, no. 8, pp. 4313–4325, 2020, doi: 10.1039/c9cp05815j.

[87] R. Gordon, “Room-temperature mid-infrared detectors.,” *Science*, vol. 374, no. 6572, pp. 1201–1202, Dec. 2021, doi: 10.1126/science.abm4252.

[88] N. Bloembergen, “Solid state infrared quantum counters,” *Phys. Rev. Lett.*, vol. 2, no. 3, pp. 84–85, 1959, doi: 10.1103/PhysRevLett.2.84.

[89] J. Stefanska and L. Marciniak, “ Single-Band Ratiometric Luminescent Thermometry Using Pr 3+ Ions Emitting in Yellow and Red Spectral Ranges ,” *Adv. Photonics Res.*, vol. 2, no. 7, 2021, doi: 10.1002/adpr.202100070.

[90] J. Stefanska, K. Maciejewska, and L. Marciniak, “Blue-emitting single band ratiometric luminescent thermometry based on LaF3:Pr3+,” *New J. Chem.*, vol. 45, no. 27, pp. 11898–11904, 2021, doi: 10.1039/d1nj01869h.

[91] K. Trejgis, A. Bednarkiewicz, and L. Marciniak, “Engineering excited state absorption based nanothermometry for temperature sensing and imaging,” *Nanoscale*, vol. 12, no. 7, pp. 4667–4675, Feb. 2020, doi: 10.1039/c9nr09740f.

[92] A. Bednarkiewicz, M. Szalkowski, M. Majak, Z. Korczak, M. Misiak, and S. Maćkowski, “All-Optical Data Processing with Photon-Avalanching Nanocrystalline Photonic Synapse,” *Adv. Mater.*, vol. 35, no. 42, pp. 1–12, 2023, doi: 10.1002/adma.202304390.

[93] A. Tymiński and T. Grzyb, “Are rare earth phosphates suitable as hosts for upconversion luminescence? Studies on nanocrystalline REPO4 (RE=Y, La, Gd, Lu) doped with Yb3+ and Eu3+, Tb3+, Ho3+, Er3+ or Tm3+ ions,” *J. Lumin.*, vol. 181, pp. 411–420, 2017, doi: 10.1016/j.jlumin.2016.09.028.

[94] A. Tymiński, T. Grzyb, and S. Lis, “REVO4-Based Nanomaterials (RE = Y, La, Gd, and Lu) as Hosts for Yb3+/Ho3+, Yb3+/Er3+, and Yb3+/Tm3+ Ions: Structural and Up-Conversion Luminescence Studies,” *J. Am. Ceram. Soc.*, vol. 99, no. 10, pp. 3300–3308, 2016, doi: 10.1111/jace.14344.

[95] T. V. Gavrilović, D. J. Jovanović, V. Lojpur, and M. D. Dramićanin, “Multifunctional Eu3+- and Er3+/Yb3+-doped GdVO4 nanoparticles synthesized by reverse micelle method,” *Sci. Rep.*, vol. 4, pp. 1–9, 2014, doi: 10.1038/srep04209.

[96] K. Kadono, H. Higuchi, M. Takahashi, Y. Kawamoto, and H. Tanaka, “Upconversion luminescence of Ga2S3-based sulfide glasses containing Er3+ions,” *J. Non. Cryst. Solids*, vol. 184, pp. 309–313, 1995, doi: 10.1016/0022-3093(94)00635-0.

[97] I.-I. Oprea, H. Hesse, and K. Betzler, “Infrared-to-visible upconversion luminescence in neodymium-doped bismuth–borate glass,” *Phys. status solidi*, vol. 242, no. 12, pp. R109–R111, 2005, doi: https://doi.org/10.1002/pssb.200541197.

[98] S. Sinha, M. K. Mahata, and K. Kumar, “Enhancing the upconversion luminescence properties of Er3+-Yb3+ doped yttrium molybdate through Mg2+ incorporation: effect of laser excitation power on temperature sensing and heat generation,” *New J. Chem.*, vol. 43, no. 15, pp. 5960–5971, 2019, doi: 10.1039/c9nj00760a.

[99] Y. Liu, Y. Chen, Y. Lin, Q. Tan, Z. Luo, and Y. Huang, “Energy transfer in Yb3$+$-Er3$+$-codoped bismuth borate glasses,” *J. Opt. Soc. Am. B*, vol. 24, no. 5, pp. 1046–1052, 2007, doi: 10.1364/JOSAB.24.001046.

[100] M. Back, E. Trave, N. Mazzucco, P. Riello, and A. Benedetti, “Tuning the upconversion light emission by bandgap engineering in bismuth oxide-based upconverting nanoparticles,” *Nanoscale*, vol. 9, no. 19, pp. 6353–6361, 2017, doi: 10.1039/c6nr09350g.

[101] C. dos S. Bezerra and M. E. G. Valerio, “Structural and optical study of CaF2 nanoparticles produced by a microwave-assisted hydrothermal method,” *Phys. B Condens. Matter*, vol. 501, pp. 106–112, 2016, doi: 10.1016/j.physb.2016.08.025.

[102] Y. Liang *et al.*, “Migrating photon avalanche in different emitters at the nanoscale enables 46th-order optical nonlinearity.,” *Nat. Nanotechnol.*, vol. 17, no. 5, pp. 524–530, May 2022, doi: 10.1038/s41565-022-01101-8.

[103] Z. Korczak *et al.*, “Sensitized photon avalanche nanothermometry in Pr3+ and Yb3+ co-doped NaYF4 colloidal nanoparticles,” *Fiz. Nizk. Temp.*, vol. 49, no. 3, pp. 351–359, 2023, doi: 10.1063/10.0017243.

[104] Y. Liang *et al.*, “Migrating photon avalanche in different emitters at the nanoscale enables 46th-order optical nonlinearity,” *Nat. Nanotechnol.*, vol. 17, no. 5, pp. 524–530, 2022, doi: 10.1038/s41565-022-01101-8.

[105] L. Marciniak, A. Bednarkiewicz, and K. Elzbieciak, “NIR-NIR photon avalanche based luminescent thermometry with Nd3+ doped nanoparticles,” *J. Mater. Chem. C*, vol. 6, no. 28, pp. 7568–7575, 2018, doi: 10.1039/c8tc01553h.

[106] M. Dudek *et al.*, “Size-Dependent Photon Avalanching in Tm3+ Doped LiYF4 Nano, Micro, and Bulk Crystals,” *Adv. Opt. Mater.*, vol. 2201052, pp. 1–12, 2022, doi: 10.1002/adom.202201052.

[107] Z. Zhang *et al.*, “Tuning Phonon Energies in Lanthanide-doped Potassium Lead Halide Nanocrystals for Enhanced Nonlinearity and Upconversion,” *Angew. Chemie - Int. Ed.*, vol. 62, no. 1, pp. 1–7, 2023, doi: 10.1002/anie.202212549.

Scientific publications:

2023

1. Understanding Yb^{3+}-sensitized photon avalanche in Pr^{3+} co-doped nanocrystals: modelling and optimization

M. Dudek, Z. Korczak, K. Prorok, O. Bezkrovnyi, L. Sun, M. Szalkowski, A. Bednarkiewicz, November 2023 Nanoscale 15, 18613-18623 (2023) doi: 10.1039/d3nr04409b

Citation: 0, Journal Impact Factor: 8.307

In this work I was responsible for measuring the anti-stokes spectra of all the nanocrystals, plotting and analyzing the obtained data. Moreover, I was responsible for measuring and interpretation of all pump power dependent luminescence intensity of the core and core-shell nanocrystals for the two emissions 607 and 482 nm. I performed all spectroscopic measurements on a special home build microscope system.

2. **Sensitized photon avalanche nanothermometry in Pr^{3+} and Yb^{3+} co-doped $NaYF_4$ colloidal nanoparticles Z. Korczak**, M. Dudek, M. Majak, M. Misiak, Ł. Marciniak, M. Szalkowski, A. Bednarkiewicz, Low Temp. Phys. 49, 351-359 (2023); doi: 10.1063/10.0017243

   Citation: 2, Journal Impact Factor: 1.618

In this work, I was responsible for making the energy diagram, measuring luminescence spectra, measuring PA properties (i.e. pump power dependent luminescence intensity and rise/decay kinetics) for the two emission bands at 607 and 482 nm, as well as measuring PA emission properties at temperatures from -175 to 175 every 25 degrees, analyzing the results, calculating temperature sensitivity, preparing the draft of the article as well as I was involved in manuscript preparation and submission.

3. **All-Optical Data Processing with Photon Avalanching Nanocrystalline Photonic Synapse**

A.Bednarkiewicz, M.Szalkowski,M.Majak, **Z.Korczak**, M.Misiak Advance Materials doi:10.1002/adma.202304390

Citation: 1, Journal Impact Factor: 29.4

In this work, my responsibilities included conducting (PA) properties measurements on the NaYF4: 8% Tm^{3+} core-shell nanocrystals. Apart from measuring luminescence kinetics, rise times under different offsets and delay times, and the intensity of two pulses with varying time intervals, I also analyzed and interpreted these results. Additionally, I contributed to the preparation of figures and edited the text.

2022

4. **Size-dependent photon avalanching in Tm^{3+} doped $LiYF_4$ nano, micro and bulk crystals**

   M. Dudek, M. Szalkowski, **Z. Korczak**, M. Misiak, R. Lisiecki, P. Woźniak, Ph. Goldner, A. Skripka, E. M. Chan, P. J. Schuck, A. Bednarkiewicz, Advanced Optical Materials, (2022), 2201052

   Citation: 1, Journal Impact Factor: 4.3

I conducted measurements involving power-dependent intensity and luminescence kinetics for nano, micro and bulk crystals. Subsequently, I conducted comprehensive calculations and analyses of the obtained results, parameters describing PA. I prepared some of the figures and edited the text. I was actively involved in building and optimizing the optical setup, which was used in all these measurements.

2021

5. **Predicting the impact of temperature dependent multi-phonon relaxation processes on the photon avalanche behavior in Tm^{3+} : $NaYF_4$ nanoparticles**

   M. Szalkowski, M. Dudek, **Z. Korczak**, Ch. Lee, Ł. Marciniak, E. M. Chan, P. J. Schuck, A. Bednarkiewicz, Optical Materials: X, Volume 12, December 2021, 100102

   Citation: 1, Journal Impact Factor: 4.3

   I was responsible for preparing editing the text.

It is essential to note that, all the mentioned spectroscopic measurements (pump power dependent emission spectra and luminescence kinetics, as well as pump power dependent luminescence intensity) required prior custom designing and developing dedicated instrument. I was actively participating in all these work, in particular I helped in the construction of the microscope system. My responsibilities included the selection and integration of optical components, alignment of lenses and mirrors for optimal performance and calibration of the system. Moreover, my role included troubleshooting when something in the system stopped working.

Scientific conferences:

1. 3rd Conference on Properties, Design, and Applications of Upconversion Nanomaterials UPCONline 2021 online conference held April 06 -09, 2021 in Compiegne, France. "Searching for photon avalanche in Nd^{3+} doped $NaGdF_4$ core-passive shell nanoparticles" Z. Korczak, M. Szalkowski, A Skripka, A. Kotulska, F. Vetrone, A. Bednarkiewicz – **poster Z. Korczak**

2. 1st International Conference on Advanced Materials for BioRelated Applications AMBRA 2022. the conference was held in Wroclaw 16-19, May 2022. "Photon avalanche in microcrystals doped with different cincentration of thulium". Z. Korczak, M.Szalkowski, M.Misiak, A. Bednarkiewicz – **poster Z. Korczak**

3. PANIC 2023 conference at Wroclaw University of Technology "Temperature dependence of photon avalanche emission in NaYF4: Pr^{3+} Yb^{3+} nanocrystals ions". Z. Korczak, M.Szalkowsk, M.Dudek, Martyna Majak, A. Bednarkiewicz – **poster Z. Korczak**

4. Poster session at the scientific conference 21st International Conference on Dynamical Processes in Excited States of Solids "INFLUENCE OF THULIUM CONCENTRATION ON PHOTON AVALANCHE BEHAVIOR IN LiYF4". Z. Korczak*, M.Szalkowski, M.Misiak, M. Ćwierzona, D. Piątkowski, S. Maćkowski, A. Bednarkiewicz – **poster Z. Korczak**

5. Poster session at the XVI Copernican Doctoral Seminar 2023 - taking 1st place in the physics category. " TEMPERATURE RELATIVITY OF LAWINOUS PHOTON

EMISSIONS IN $NaYF_4$ DOMINATED Pr^{3+} and Yb^{3+} NANOCRYSTALS". Z. Korczak*, M.Szalkowski, M.Dudek, Martyna Majak, A. Bednarkiewicz – **poster Z. Korczak**

6. VII Conference of Doctoral Students of the PAS (KonDokPAN 2023) "Temperature dependence of photon avalanche emission in NaYF4 nanocrystals co-doped with Pr^{3+}/Yb^{3+}". Z. Korczak*, M.Szalkowski, M.Dudek, Martyna Majak, A. Bednarkiewicz – **lecture Z. Korczak**

Other activities

- 13th International Course "Time-resolved Microscopy and Correlation Spectroscopy". March 2-5, 2021 - online event broadcast from Berlin, Germany. The course covered various time-resolved techniques, e.g. FCS, FLIM, FLIM-FRET - **participant**

- Nicolaus Copernicus University in Torun to the Department of Physics, Astronomy and Computer Science. I participated in the imaging of LiYF4:3%Tm^{3+} single microcrystals and $LiYF_4$:3%Tm^{3+} nanocrystals on a confocal microscope and assisted in the imaging of single crystals using a scanning electron microscope. Two research visits (2x 1 week) :

- Lower Silesian Science Festival - running a stand with experiments for children and young people, **giving popular science lectures**

- Running the social media of INTiBS PAN

- Competition for popularization of science in the social media category of the eDoctoral portal– **second prize**